Journal of the Mechanics and Physics of Solids 143 (2020) 104070

Contents lists available at ScienceDirect

Journal of the Mechanics and Physics of Solids

journal homepage: www.elsevier.com/locate/jmps

An investigation of models for elastic ribbons: Simulations & experiments☆

Arun Kumar, Poornakanta Handral, C S Darshan Bhandari, Anindya Karmakar, Ramsharan Rangarajan*

Department of Mechanical Engineering, Indian Institute of Science Bangalore, 560012, India

ARTICLE INFO

Article history:
Received 5 February 2020
Revised 15 June 2020
Accepted 26 June 2020
Available online 1 July 2020

Keywords:
Annular ribbons
Cosserat theory
Geometric nonlinearity
Kirchhoff rods
von Kármán plates

ABSTRACT

Understanding the feature-rich buckling-dominated behavior of thin elastic ribbons is ripe with opportunities for fundamental studies exploring the nexus between geometry and mechanics, and for conceiving of engineering applications that exploit geometric nonlinearity as a functioning principle. Predictive mechanical models play an instrumental role to this end. As a direct consequence of their physical appearance, ribbons are usually modeled either as one-dimensional rods having wide cross sections, or as narrow two-dimensional plates/shells. These models employ drastically different kinematic assumptions, which in turn play a decisive role in their predictive capabilities. Here, we critically examine three modeling approaches for elastic ribbons using detailed measurements of their complex three-dimensional deformations realized in quasistatic experiments with annulus-shaped ribbons. We find that simple and practically realizable ribbon deformations contradict assumptions underlying strain-displacement relationships in nonlinear rod and von Kármán plate models. These observations do not point at shortcomings of the theories themselves, but highlight fallacies in their application to modeling ribbon-like structures that are capable of undergoing large displacements and rotations. We identify and validate, seemingly for the first time, the 1-director Cosserat plate theory as a model for elastic ribbons over a useful range of loading conditions. In the process, we demonstrate annular ribbons to be prototypical systems for studying the mechanics of elastic ribbons. Annular ribbons exhibit a tunable degree of geometric nonlinearity in response to simple displacement and rotation boundary conditions— a feature that we exploit here for highlighting the consequences of kinematic assumptions underlying different ribbon models. We additionally provide experimental evidence for the existence of multiple stable equilibria, bifurcation phenomena correlated with the number of zero crossings in the mean curvature, and localization of energy, thus making annular ribbons interesting mechanical systems to study in their own right.

☆ Research supported by the Science and Engineering Research Board (SERB) through the Early Career Research Award ECR/2017/000346.
* Corresponding author.
E-mail address: rram@iisc.ac.in (R. Rangarajan).

https://doi.org/10.1016/j.jmps.2020.104070
0022-5096/

1. Introduction

Ribbons are slender structures characterized by three disparate geometric dimensions— length ℓ, width w and thickness h, which are ordered such that $\ell \gg w \gg h$. The pair of aspect ratios ℓ/w and w/h dictate their rich buckling-dominated mechanical behavior. In many ways, a growing body of literature on the mechanics of ribbons is exemplary of an evolving paradigm that considers buckling and related geometric nonlinearities as features to be exploited, rather than as modes of failure (Reis, 2015). Hence, ribbons are viewed as shape-programmable structures in flexible robotics and energy harvesting applications (Agostiniani et al., 2017; Armon et al., 2014; Shim et al., 2012). Manufacturing methods, functioning principles and assembly of miniaturized stretchable electronic devices require detailed understanding of the mechanics of ribbons adhered to elastic substrates (Fan et al., 2018; Jiang et al., 2008; Luo et al., 2019; Sun et al., 2006; Tarasovs and Andersons, 2008; Vella et al., 2009). Design and deployment of kirigami-inspired engineering structures depends on exploiting controlled post-buckling behavior of elastic ribbons (Dias et al., 2017; Rafsanjani and Bertoldi, 2017). From sheet metal processing (Fischer et al., 2003), to modeling DNA (Moakher and Maddocks, 2005) and fabricating carbon nanotubes (Kit et al., 2012), ribbon mechanics transcends not only length scales, but also traditional subject classifications.

We are concerned here with elastic ribbons having a planar unstressed configuration, that undergo large but reversible displacements while incurring small strains. As their geometry suggests, such ribbons can be considered either as narrow plates or as rods with highly anisotropic cross sections. This geometrical dichotomy is evident in mechanical models too. The two most commonly used approaches for modeling ribbons are as one-dimensional Kirchhoff rods (Goriely et al., 2001; Mahadevan and Keller, 1993; Moore and Healey, 2019; Morigaki et al., 2016; Sano and Wada, 2019) and as two-dimensional von Kármán plates (Chopin et al., 2015; Green, 1936). A systematic way of deducing one dimensional models from plate theories arises from the observation that ribbons remain nearly unstretched over a broad range of loading conditions. Material inextensibility manifests as a pointwise kinematic constraint that deformed configurations remain isometric to the unstressed state. In particular, inextensibility implies that the (mid)surface of a ribbon remains developable during deformation. These ideas have been frequently invoked to construct mathematical descriptions of Möbius strips (Starostin and van der Heijden, 2007; 2015; Todres, 2015) and to compute deflections/stresses in plates and shells (Harnach and Rothert, 1976; Mansfield, 1955). Integrating developability constraints within the framework of a classical Kirchhoff rod model yields new nonlinear rod models (Dias and Audoly, 2014; 2015) that elegantly unify ideas for describing surfaces in differential geometry with structural mechanics theories.

Our goal in this article is to critically examine modeling approaches for elastic ribbons. Specifically, we consider modeling elastic ribbons as 2-director Cosserat rods, as von Kármán plates and as 1-director Cosserat plates. The two plate theories represent weakly nonlinear and fully nonlinear two-dimensional models. In the context of the experiments considered here, the 2-director Cosserat rod theory serves as a computationally convenient alternative to the Kirchhoff rod theory in which inextensibility and unshearability constraints are imposed weakly.

Fig. 1 succinctly summarizes the motivation for our investigation. The figure illustrates three simple virtual experiments that involve rotating and translating clamped ends of semi-annular/annular ribbons. It shows predictions of the Cosserat rod model alongside those of linear (Reissner-Mindlin), von Kármán and Cosserat plate theories. These simulations represent converged numerical solutions for the respective models. In each case, we find that a pair of models make drastically different predictions for the deformed shape of a ribbon. The figure then evokes the obvious question— *which prediction is right?* We resort to simple experimental realizations of such loading scenarios along with detailed measurements to settle this conundrum.

Evidently, the three models considered here are not representative of the spectrum of geometrical nonlinearity possible in rod/plate theories that have been proposed in the literature. For instance, the well known nonlinear plate theories of (Sanders, 1963; Koiter, 1966) are not investigated. Indeed, it is not our intention to exhaustively examine the applicability of various rod/plate theories for modeling elastic ribbons. Yet, it is imperative to critically examine commonly used ones, which is the rationale behind considering the von Kármán plate and 2-director Cosserat rod theories, with the latter serving as a proxy for the Kirchhoff theory. The 1-director Cosserat plate theory represents a fully geometrically nonlinear model, and its application to modeling elastic ribbons appears to be new. We also note that although some of the models examined here can be generalized to account for finite strains, our aim is to examine the significance of *geometric* nonlinearity, i.e., of strain-displacement relationships underlying these models. Without exception therefore, we ensure that strains remain small, and consequently, assume a linear relationship between conjugate stress-strain measures.

We compute predictions of the aforementioned models using appropriate finite element methods. This is a challenging endeavor in itself, cf. Moore and Healey (2019); Taylor et al. (2015). Our emphasis, however, is not centered on intricacies involved in the various approximation algorithms involved, see Appendix B. Instead, the novelty of our investigation is the set of simple experiments designed to facilitate detailed comparisons between model predictions and experimental measurements. We consider ribbon geometries and boundary conditions that elucidate varying degrees of geometric nonlinearity to help examine the appropriateness of strain-displacement relationships assumed in different ribbon models. We adopt a non contact optical method for pointwise shape measurements in the experiments, which we directly compare with predicted ribbon shapes. Noting that even small disparities in curvatures can manifest as large differences in overall shape, we compare mean curvatures computed from measurements with model predictions.

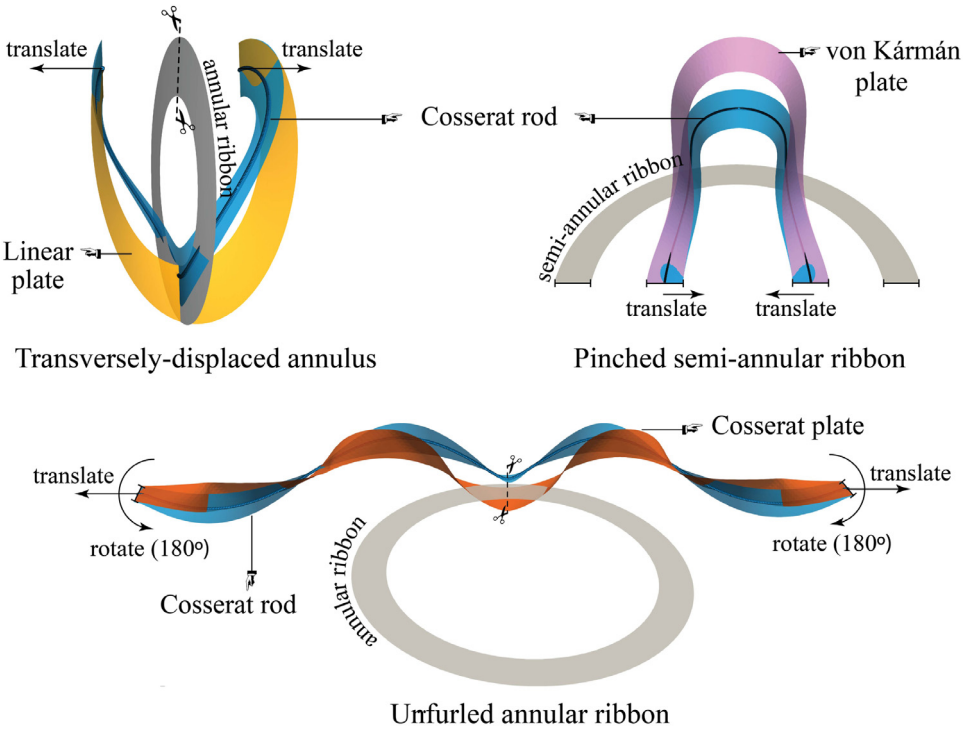

Fig. 1. Virtual experiments using planar elastic ribbons (in gray) with a nonzero geodesic curvature expose unambiguous differences between the predictions of four models for elastic ribbons (in color). Our goal in this article is to critically examine the accuracies of these predictions using detailed measurements from simple experiments realizing the loading scenarios depicted in the figure.

An important feature of our comparisons between experimental measurements and model predictions is that they do not involve any fitting parameters. The ribbon specimens we use in the experiments are cut from flexible radiography films, whose constitutive response we assume to be isotropic. Then, since all our experiments are displacement-controlled, model predictions can be computed without knowledge of the elastic modulus. Furthermore, as reported in studies elsewhere (Sano and Wada, 2019; Tarasovs and Andersons, 2008; Yu and Hanna, 2019), we find that the Poisson's ratio (assumed to be 0.4 in all our calculations) does not appreciably influence predictions of the models examined. In this sense, our findings are independent of material composition, provided that the constitutive response is linear and isotropic.

In the context of the existing literature on models for elastic ribbons, our findings concerning the von Kármán plate and the Kirchhoff rod models are noteworthy. We show that predictions of the von Kármán model can be erroneous in loading scenarios that appear to be far less severe than problems in which it is routinely applied, cf. Liang and Mahadevan (2009, 2011). Similar observations have been demonstrated in studies on predicting instabilities in plates and ribbons (Ben Amar and Pomeau, 1997; Chopin et al., 2015). These findings echo Ciarlet's opinion in Ciarlet (1997) that *"... the validity of the classical lower-dimensional equations, such as the two dimensional von Kármán equations for nonlinearly elastic plates... is no longer left unquestioned."*

Contrary to plate models, where the width is treated as an independent coordinate, the classical Kirchhoff rod model for ribbons treats the width simply as a parameter that modulates the bending and torsional stiffnesses. Despite glaring approximations in the kinematics of cross sections, rod models have shown plenty of promise, especially for predicting instabilities in ribbons (Goriely et al., 2001; Morigaki et al., 2016; Sano and Wada, 2019; Yu and Hanna, 2019). Clear shortcomings have been identified as well. For instance, Audoly and Seffen (2015) demonstrates a mode of instability in ribbons that is not predicted by the Kirchhoff rod theory.

Our findings related to the von Kármán plate and Kirchhoff rod models should not be misconstrued as identifying shortcomings of the models themselves. In fact, we identify kinematic assumptions in these models that are clearly violated in the experiments, and are presumably responsible for their poor predictions. It is not our purpose here to question the general validities of these models (Ciarlet, 1980; Dill, 1992). Instead, our experiments are aimed at highlighting their applicability to modeling elastic ribbons and our findings serve to caution against the application of these models for predicting deformations of elastic ribbons without careful deliberation of the kinematics involved.

Our study here comparing model predictions with experiments using annular ribbons serves multiple purposes.

- Among the theories examined, we find that the 1-director Cosserat plate model best matches the experimental measurements. Its application to ribbon mechanics appears to be new, and based on our experiments, very promising. In

this sense, we identify a promising model for elastic ribbons over a practically useful range of deformations. A predictive model is an invaluable tool, both at small and large length scales where detailed observations or quantitative measurements may be difficult. For ribbons to become an integral part of engineering applications that exploit flexibility of slender structures, a virtual simulation framework is essential, and will augment an existing arsenal of scaling laws (Witten, 2007).

- Second, our study demonstrates that annular ribbons can serve as prototypical systems to highlight the consequences of kinematic assumptions inherent in commonly used models for slender elastic structures. Linearizations and approximations in reduced order theories are well known, are routinely taught in courses on structural mechanics, and are being rigorously justified using tools from asymptotic analysis (Ciarlet, 1980; 1997; Fox et al., 1993; Steigmann, 2013) and Γ-convergence (Friesecke et al., 2006; Kirby and Fried, 2015). Yet, manifestations of these assumptions are rarely examined in practice, much less in a unified manner using a simple experimental system. Here, we show that commonly used rod and plate models differ quantitatively in their predictions for deformations of annular ribbons as a direct consequence of the kinematic assumptions they invoke. In fact, Fig. 1 provides unambiguous evidence to this effect.
- Third, our study establishes a clear way to test dedicated one-dimensional ribbon models that have been recently proposed in the literature. Specifically, simulations using 1-director Cosserat plates can serve as benchmark solutions against which to compare predictions of various ribbon models. It is possible that our findings concerning the Cosserat plate model may inspire new reduced order models for ribbons.

Organization: The remainder of the article is organized as follows. In Section 2, we provide a brief overview of the experiments with ribbons, the shape measurement technique used and the algorithms adopted for data analysis. In Section 3, we briefly discuss the von Kármán theory as a weakly nonlinear plate model for elastic ribbons, and examine its accuracy using the transversely displaced annulus and the pinched semi annulus experiments. We devote Section 4 to discussing the applicability of the 2-director Cosserat rod model for ribbons. Therein, using the unfurled annular ribbon experiment, we highlight qualitative and quantitative shortcomings in modeling ribbons as elastic rods. Next in Section 5, we outline the 1-director Cosserat plate theory and demonstrate its promise for modeling complex three-dimensional ribbon deformations realized in response to a practically useful range of boundary conditions. We highlight interesting features of the deformations observed in the pinched semi annulus and unfurled annulus experiments in Sections 6 and 7, and conclude the article in Section 8 with a set of remarks.

2. Overview of ribbon experiments

We briefly discuss the ribbon experiments used in subsequent sections to examine the accuracies of different ribbon models, the technique used to measure (i.e., digitize) deformed ribbon shapes as dense point clouds, and the algorithms used to compute curvatures and centerline shapes from the measured data. We begin with a description of the ribbon samples used in the experiments.

2.1. Ribbon samples

Without exception, all our ribbon samples have a planar unstressed configuration and a rectangular cross section. We denote the width of the cross section by w and the thickness by h. Ribbon samples are cut from flat exposed radiography sheets having a thickness of $h = 0.18$ mm. Though not important for our purposes, we note that these films are composed of a base layer of Polyethylene Terephthalate, which is coated on either side with thin emulsion layers. The base layer has a nominal elastic modulus of 2.5 GPa, is flexible, and provides structural support. The emulsion layers mainly serve to modulate imaging properties in radiological applications. We cut annular ribbon samples from flat sheets using a low power laser. We presume that local changes in thickness and in material properties caused by heating in narrow regions along ribbon edges cut by the laser are of negligible significance.

2.2. Experiments

Among the three experiments we consider, the suggestively named *transversely displaced annular ribbon* and the *unfurled annular ribbon* experiments use annulus-shaped ribbons. For these, an annulus-shaped ribbon is slit along a radial line to create a pair of mating edges. The edges are held in clamps which can be rotated and translated with respect to each other, thereby creating a variety of loading conditions for the ribbon. In the transversely displaced annulus experiment, clamps holding the ribbon edges are translated in the direction of the normal to the undeformed plane of the ribbon, see Fig. 3a. In the unfurled annulus experiment depicted in Fig. 9a, ribbon edges are rotated by 180° about the normal to the plane of the ribbon, and translated along a perpendicular diametrical axis. Ribbons respond to the imposed boundary conditions by buckling into three-dimensional configurations due to compression along its free edges. In the *pinched semi* annulus experiment, we cut an annular ribbon along a diametrical line and translate the resulting straight edges towards each other along the direction of the cut, see Fig. 4a. Evidently, the pinching action causes the ribbon to buckle out of plane.

The widths of the annular and semi annular ribbons, measured as the difference between the outer and inner radii, range from 20 mm to 35 mm. Hence, the aspect ratio w/h of the cross section generally exceeds 100. We choose the mean radius,

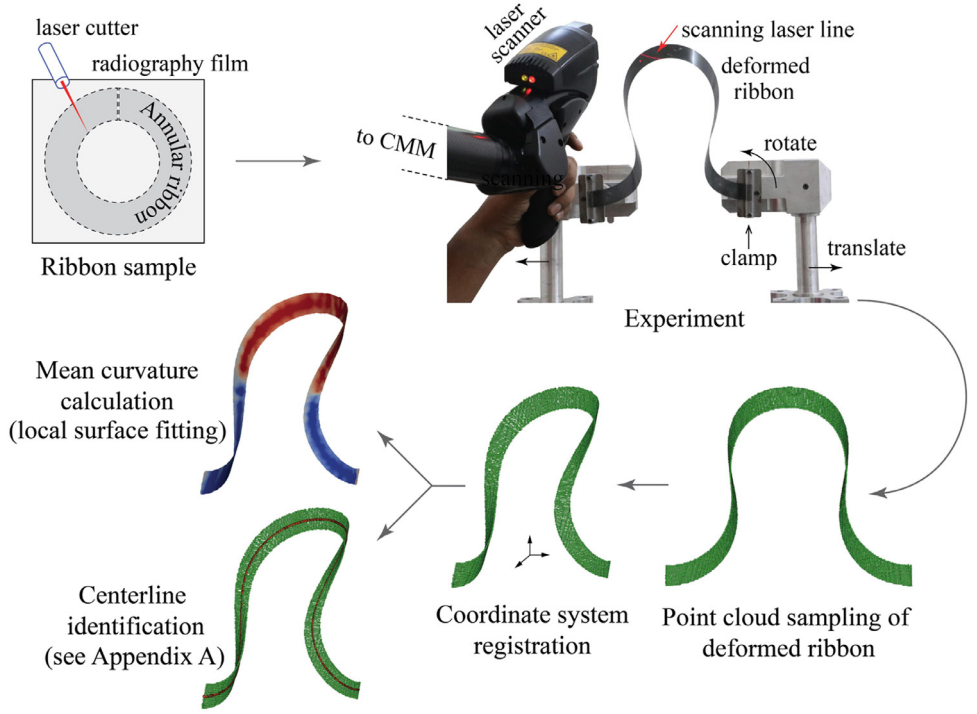

Fig. 2. Illustration of the experimental procedure. The figure shows an annular ribbon cut from a radiography film being loaded using a pair of rotatable and translatable clamps. The shape of the deformed ribbon is measured as a dense point cloud using a laser line scanner and is used for comparisons with model predictions.

henceforth denoted by R, to be at least 4 or 5 times larger than the width, resulting in an aspect ratio $\ell/w = \pi\,(\mathrm{R}_i + \mathrm{R}_o)/w$ in the range of 25 to 30.

Ribbon deformations in all our experiments are fully reversible. Although displacements involved are large and comparable to the dimensions of the ribbon, strains remain small and the material does not suffer any irreversible damage. In particular, ribbon shapes measured in the experiments do not show any noticeable differences after multiple loading/unloading cycles.

2.3. Shape measurements

Owing to their small thickness, our ribbon samples have relatively small flexural rigidities. Hence, contact probes are not well suited for recording their deformed shapes realized in the experiments. Instead, we exploit the fact that exposed radiography films are sufficiently opaque to warrant resorting to optical measurement techniques. We use a laser line scanner mounted on a coordinate measuring machine (Romer Absolute Arm 7320, Hexagon Metrology) to digitize deformed shapes of ribbons, see Fig. 2. A similar principle is used in Seereeram and Seffen (2014) to measure deformations of plates in bending. Scanning a ribbon yields a dense point cloud sampling its exposed surfaces. We generally ensure a density of at least 750 points per square inch in our measurements, and resort to higher resolutions in experiments that involve the formation of localized features, cf. Fig. 26.

The coordinate system used during measurements is approximately aligned with that adopted for corresponding simulations. Noting that small errors in alignment can manifest as large deviations when comparing measured and predicted ribbon shapes, we refine the alignment further using a registration procedure. Specifically, we compute a rigid body transformation, comprising of a rotation $\mathbf{R}$ and a translation $\mathbf{t}$, that aligns the coordinate system of the CMM (coordinate measuring machine) with that used in simulations using the iterative closest point (ICP) registration algorithm (Besl and McKay, 1992). Denoting dense point cloud samplings of deformed ribbon surfaces from simulations and experiments by $\{\mathbf{x}_i\}_{i=1}^n$ and $\{\mathbf{y}_i\}_{i=1}^m$ respectively, the registration algorithm computes $\mathbf{R}$ and $\mathbf{t}$ such that the misalignment error $\mathrm{E}(\mathbf{R},\mathbf{t}) = \frac{1}{2}\sum_{i=1}^m \|\pi_{\mathbf{x}}(\mathbf{R}\mathbf{y}_i+\mathbf{t}) - (\mathbf{R}\mathbf{y}_i+\mathbf{t})\|^2$ is minimized, where $\pi_{\mathbf{x}}(\mathbf{y}) = \arg\min_{\mathbf{x}_j} \|\mathbf{y}-\mathbf{x}_j\|$ identifies the closest point in $\{\mathbf{x}_i\}_{i=1}^n$ for a given $\mathbf{y}$. The resulting transformation $\{\mathbf{y}_i\}_{i=1}^m \mapsto \{\mathbf{R}\mathbf{y}_i+\mathbf{t}\}_{i=1}^m$ of the measured data does not introduce any distortion or permit any rescaling; it merely places the measured digital representation of the ribbon in a prescribed coordinate system.

2.4. Mean curvatures from measured point clouds

Recognizing their critical role in bending dominated deformations, we compute mean curvature distributions from measured point clouds for comparisons with model predictions. Besides facilitating an inspection of bending strains, we also note that mean curvatures are invariant to rigid body transformations. For this reason, comparisons of mean curvatures are unaffected by errors in alignment of coordinate systems used in simulations and experiments.

Evidently, defining mean curvatures for a point cloud sampling requires surface fitting/approximation. To this end, we adopt the algorithm of Cazals and Pouget (2005) and its implementation in the Computational Geometry and Algorithms Library (CGAL) (Alliez et al., 2019). Thus, at each point in the measured cloud, we compute a quadratic Monge patch defined in a local frame in order to fit points in the immediate neighborhood in a least-squares sense. Then, curvatures computed for such local surface patches define the curvatures at points in the measured data set. The number of neighbors defining local patches is an important choice in these calculations— too small a number results in a noisy distribution, while fitting over a large neighborhood results in unintended smoothing. In our calculations, we use points belonging to the first three rings in the immediate neighborhood. This procedure typically identifies about a dozen neighbors for each patch. We have verified that small changes in the size of the neighborhood do not appreciably affect the curvatures reported.

2.5. Mappings to the reference configuration from point cloud measurements

The three-dimensional nature of ribbon configurations observed in our experiments makes it challenging to analyze important features of the deformations. It is far more convenient, at least for the sake of visualization, to pull back fields of interest (e.g., mean curvatures) to the planar reference configuration. Unfortunately, since our measurements do not involve surface labeling or particle tracking, it is not possible to reconstruct the deformation mapping to help realize such a pull back. Nevertheless, borrowing techniques from computational geometry and following the steps outlined in Appendix A, we construct an injective correspondence between the reference and deformed configurations, while using only a point cloud sampling of the deformed surface of the ribbon as input. The mapping constructed this way is *not* the deformation mapping, but can be considered an approximation of it in the sense discussed in Appendix A. We use it extensively in our comparisons between experiments and simulations for two purposes. First, it helps us visualize contours of mean curvature computed using the measured point cloud over the reference configuration, see Figs. 8, 25, 26. Second, it helps us identify deformed centerlines of ribbons, which is not directly available from our point cloud measurements. Instead, we use the constructed mapping to determine the deformed centerline as the image of the centerline in the reference configuration. This, in turn, enables us to examine mean curvature distributions along centerlines determined from the experimental measurements, see Figs. 3d, 8,9c, 10b, 12, 13d and 14b.

2.6. Sources of error

The experimental measurements reported in subsequent sections are representative samples from multiple repetitions. Their repeatability notwithstanding, we identify a few important sources of error. A key source of uncertainty is the extent of the ribbon inserted into clamps in order to ensure a firm grip. We use clamps made of clear Acrylic (see Figs. 2 and 5) to help visually confirm that the length of the ribbon held within each clamp does not exceed 1–2 mm. A second source of error stems from the unaccounted influence of gravity. This is an important concern in the pinched semi annulus and unfurled annulus experiments because low flexural stiffnesses of ribbons make them susceptible to deformations induced by self weight. For this reason, we specifically identify ribbon configurations in which gravity effects are verifiably small. To this end, we compare a ribbon's configuration with another in which the clamps holding the edges are rotated by 180°. This modification in boundary conditions effectively mimics inverting the orientation of the gravitational force acting on the sample. Then, we deem gravity effects to be negligible if the measured shapes of the two configurations are (approximately) mirror images of each other about the horizontal plane passing through the centers of rotation of the clamps. A brief discussion of this procedure for the unfurled annulus experiment is provided at the beginning of Section 7. Finally, we note that the laser scanner used for shape measurements has an accuracy of 80 μm.

3. Ribbons as von Kármán plates

The von Kármán plate theory serves as our exemplar of a weakly nonlinear plate model for ribbons. In the following, we briefly recall the kinematics associated with the model and provide the energy functional extremized by equilibrium solutions. We adopt a system of Cartesian coordinates for $\mathbb{R}^3$, wherein the domain of the ribbon is given by the set $\Omega_0 \times (-h/2, h/2)$, with $\Omega_0 \subset \mathbb{R}^2$ denoting the mid surface lying in the plane spanned by the $\mathbf{E}_1$ and $\mathbf{E}_2$ axes. The $\mathbf{E}_3$ axis coincides with the direction of the ribbon's thickness. We follow common conventions used for indicial notations, with all derivatives and components of vectors/tensors referring to coordinates in the $\{\mathbf{E}_1, \mathbf{E}_2, \mathbf{E}_3\}$ basis.

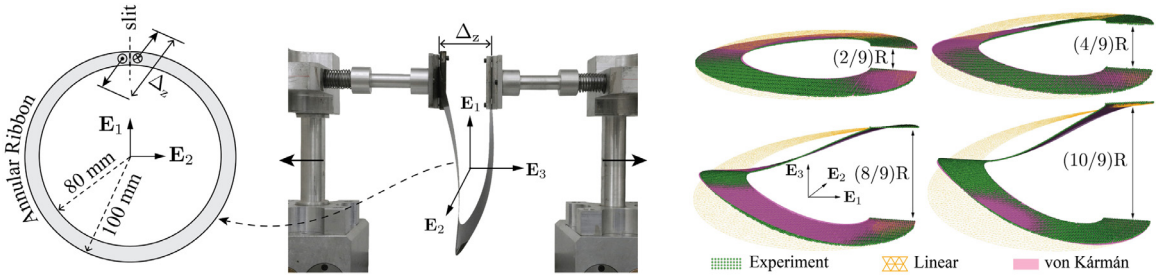

(a) Setup for the transversely displaced annular ribbon experiment.

(b) Measured and predicted ribbon shapes

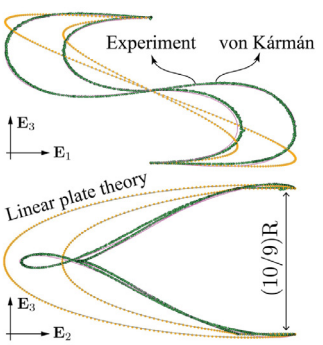

(c) Projected views of the deformed ribbon's centerline

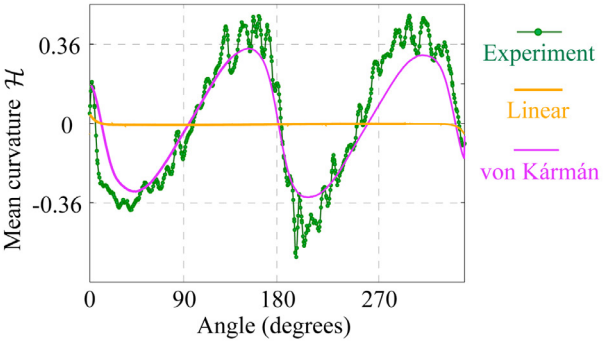

(d) Measured and predicted mean curvature distributions for $\Delta_z = (10/9)\mathrm{R}$. The abscissa in the plot refers to the angular coordinate along the circular centerline in the reference configuration.

Fig. 3. Setup, measurements and model predictions for the transversely displaced annular ribbon experiment discussed in Section 3.2.

3.1. The von Kármán plate model

The ansatz for the displacement field in the model is given by

$$\mathbf{U}(\mathbf{x}, x_3) = (u_1(\mathbf{x}) - x_3 u_{3,1}(\mathbf{x}))\,\mathbf{E}_1 + (u_2(\mathbf{x}) - x_3 u_{3,2}(\mathbf{x}))\,\mathbf{E}_2 + u_3(\mathbf{x})\,\mathbf{E}_3, \tag{1}$$

where $\mathbf{x} = (x_1, x_2) \in \Omega_0$, $x_3 \in (-h/2, h/2)$, and $\mathbf{u} = (u_1, u_2, u_3)$ represents the displacement of the mid surface. Eq. (1) implies that material fibers along the transverse direction remain straight and undistorted during deformation. The Kirchhoff assumption, evident in 1, dictates that transverse material fibers additionally remain normal to the mid surface (in a linearized sense) during deformation. The assumption of small rotations of transverse fibers is made apparent by the terms $x_3(u_{3,1}\mathbf{E}_1 + u_{3,2}\mathbf{E}_2)$ representing the in-plane projections of transverse displacements.

The strain measure in the model is given by

$$\boldsymbol{\varepsilon}_{\mathrm{vk}}(\mathbf{x}, x_3) = \begin{bmatrix} u_{1,1} - x_3 u_{3,11} & (u_{1,2} + u_{2,1})/2 - x_3 u_{3,12} & 0 \\ \mathrm{sym.} & u_{2,2} - x_3 u_{3,22} & 0 \\ & & 0 \end{bmatrix} + \frac{1}{2}\begin{bmatrix} u_{3,1}^2 & u_{3,1}u_{3,2} & 0 \\ \mathrm{sym.} & u_{3,2}^2 & 0 \\ & & 0 \end{bmatrix} \triangleq \boldsymbol{\varepsilon} + \frac{\nabla u_3 \otimes \nabla u_3}{2}, \tag{2}$$

where the splitting of terms helps distinguish linear and nonlinear dependencies of the strain on displacement components. The first term $\boldsymbol{\varepsilon}$ in Eq. (2) is the linearized strain measure from the classical Kirchhoff-Love plate theory. The second term $(\nabla u_3 \otimes \nabla u_3)/2$ contains quadratic contributions from derivatives of the transverse displacement, thus endowing the model with geometric nonlinearity. While in-plane shear strains are permitted, transverse shear strains vanish as a consequence of the Kirchhoff hypothesis. The vanishing strain component $(\varepsilon_{\mathrm{vk}})_{33}$ conveys inextensibility along the transverse direction. The form of Eq. (2) is amenable to multiple interpretations concerning relative magnitudes of strain and rotation components (Ciarlet, 1980). For instance, comparing Eq. (2) with the Green-Lagrange strain corresponding to the displacement field $\mathbf{U}$ in Eq. (1) reveals that it is necessary to explicitly assume displacement derivatives to be small compared to unity, to drop terms that depend on cubic and higher powers of the displacement, as well as to selectively retain quadratic terms depending on the transverse displacement, see Section 5.1. The justification for the latter approximation, as explained in Ciarlet (1980), is based on examining the scalings of in-plane and transverse displacements with the plate thickness, which reveals that derivatives of (u_1, u_2) decay faster with h compared to derivatives of u_3.

Assuming the material constitution to be homogeneous, linearly elastic and isotropic, and denoting the elastic modulus by E and the Poisson ratio by ν, the strain energy in the model is given by Shames and Dym (1995, Chapter 8)

$$\Pi^{\text{vK}} = \Pi^{\text{vK}}_{\text{m}} + \Pi^{\text{vK}}_{\text{b}},$$

$$\text{where} \quad \Pi^{\text{vK}}_{\text{m}} = \frac{\text{E}h}{2(1-\nu^2)} \int_{\Omega_0} \Big\{ \big(u_{1,1} + u_{3,1}^2/2\big)^2 + \big(u_{2,2} + u_{3,2}^2/2\big)^2 + 2\nu\big(u_{1,1} + u_{3,1}^2/2\big)\big(u_{2,2} + u_{3,2}^2/2\big) + \frac{1-\nu}{2}(u_{1,2} + u_{2,1} + u_{3,1}u_{3,2})^2 \Big\}\, d\mathbf{x}$$

$$\text{and} \quad \Pi^{\text{vK}}_{\text{b}} = \frac{1}{2}\frac{\text{E}h^3}{12(1-\nu^2)} \int_{\Omega_0} \big((u_{3,11} + u_{3,22})^2 - 2(1-\nu)(u_{3,11}u_{3,22} - u_{3,12}^2)\big)\, d\mathbf{x}. \tag{3}$$

The splitting of integrals in Eq. (3) distinguishes contributions from stretching ($\Pi^{\text{vK}}_{\text{m}}$) and bending deformations ($\Pi^{\text{vK}}_{\text{b}}$), and highlights their expected scalings with the thickness h of the ribbon. The Euler-Lagrange equations derivable from Eq. (3) yield familiar statements of balances of resultant forces and moments, which are a set of nonlinear partial differential equations (Shames and Dym, 1995, Chapter 8). For the purpose of computing finite element approximations, Eq. (3) supplemented with appropriate boundary conditions along $\partial\Omega_0$ suffice.

The contribution from bending in the von Kármán plate model is symbolically identical to that in the classical Kirchhoff-Love model. The distinction between the two models in fact lies in the membrane contribution. While the membrane component of the energy in the linear theory depends solely, and quadratically, on the in-plane displacement components u_1 and u_2, the energy $\Pi^{\text{vK}}_{\text{m}}$ depends on derivatives of the transverse displacement u_3 as well. As a consequence, membrane force balance in the linear model is independent of u_3, but is intimately and nonlinearly coupled to u_3 in the von Kármán equations.

The terms $(u_{3,11} + u_{3,22})$ and $(u_{3,11}u_{3,22} - u_{3,12}^2)$ appearing in the bending energy functional can be interpreted to be the mean and Gaussian curvatures of the mid surface, computed while invoking assumptions consistent with the strain-displacement relationship in Eq. (2). In this context, we highlight the close resemblance of $\Pi^{\text{vK}}_{\text{b}}$ to the Willmore functional used for modeling biomembranes. We also note that in the limit of vanishing thickness, Eq. (3) yields a membrane model that is useful in studying wrinkling phenomena by identifying regions subjected to compressive stresses. This limit, however, is not useful in our examples involving bending dominated deformations in which we anticipate membrane strains and Gaussian curvatures to be small. Instead, we expect that extremizing Eq. (3) will identify deformations that are approximately isometric to the undeformed state of the ribbon.

3.2. Transversely displaced annular ribbon

The first experiment we consider is a displacement-controlled variant of the "thin plate ring test" that is routinely used for benchmarking finite element solutions of plate models (Başar and Ding, 1992). As depicted in Fig. 3a, the experiment involves cutting an annular ribbon along a radial line and holding the edges created in translatable clamps. In the system of coordinates indicated in the figure, the ribbon lies in the $\mathbf{E}_1 - \mathbf{E}_2$ plane, the slit is parallel to the $\mathbf{E}_1$ axis, and the clamps are translated along the $\mathbf{E}_3$ direction. The ribbon has mean radius $\text{R} = 90\,\text{mm}$ and width $w = 20\,\text{mm}$. The separation Δ_z between the ends is controlled by moving cylindrical posts holding the clamps using a lead screw mechanism (not shown in the image).

We increase the separation Δ_z in integer multiples of the width and measure shapes of the realized deformations. Fig. 3b shows the measured point clouds from the experiment in green, alongside predictions of the von Kármán plate model (in magenta), which closely follow the experiment. For the case in which Δ_z equals the outer radius of the ribbon, Fig. 3c compares projections of the deformed centerline and Fig. 3d the non dimensionalized mean curvature $\mathcal{H} = \text{R} \times \text{H}$ along the centerline. In many ways, the favorable comparisons of the von Kármán model with the experimental data seen in Figs. 3a–d justifies its widespread application and highlights the targeted nature of nonlinearity in the model. It is generally well recognized that despite the explicit assumptions of small displacements and moderate rotations invoked in the strain-displacement relationship in Eq. (2), and the consequent lack of frame invariance, the model is applicable far from these thresholds (Audoly and Pomeau, 2010, Chapter 7). We will see in Section 4 that a nonlinear rod model also predicts the deformations observed in this experiment quite well. Then, the consistency of the von Kármán plate theory with the Kirchhoff rod model for narrow ribbons suggests that the results in Fig. 3 are not surprising (Audoly and Pomeau, 2010, Chapter 6.7).

For the sake of completeness, Fig. 3b–d also shows the predictions of a linear plate model (Reissner-Mindlin). Large deviations evident in the plots are a consequence of the linearized strain-displacement relationship, rather than the specific plate model adopted. In essence, the displacement field in the experiment does not simply scale linearly with Δ_z. This result, however unremarkable, provides sufficient reason to disregard geometrically linear theories for modeling ribbons. It also highlights the fact that nonlinear contributions of the transverse displacement to the in-plane strain components in the von Kármán model conspire to identify a more physically realistic deformation.

3.3. Pinched semi annular ribbon

In the next experiment, we cut an annulus-shaped sample having mean radius $\text{R} = 90\,\text{mm}$ and width $w = 20\,\text{mm}$ along a diametrical line to create a semi annular ribbon. Referring to the coordinate system indicated in Fig. 4a, straight edges of the ribbon created by the cut are parallel to the $\mathbf{E}_2$ axis, and are held in clamps oriented along the straight edges. The distance

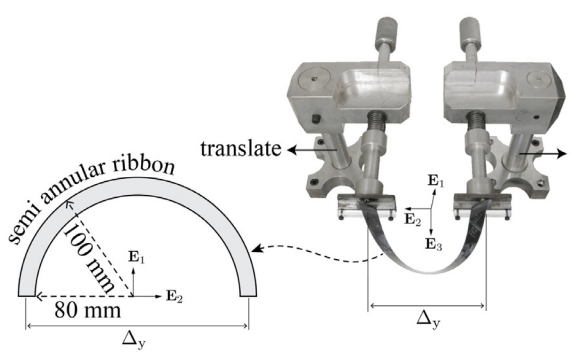

(a) Experimental setup.

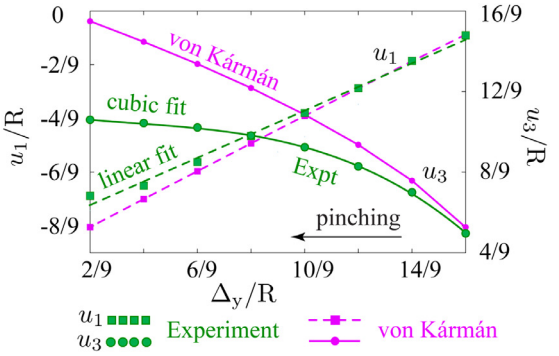

(b) Measured and predicted displacements at the midpoint of the centerline of the ribbon.

Fig. 4. The pinched semi annular ribbon experiment shows a nonlinear dependence of the transverse displacement u_3 at the midpoint of the ribbon with the loading parameter Δ_y.

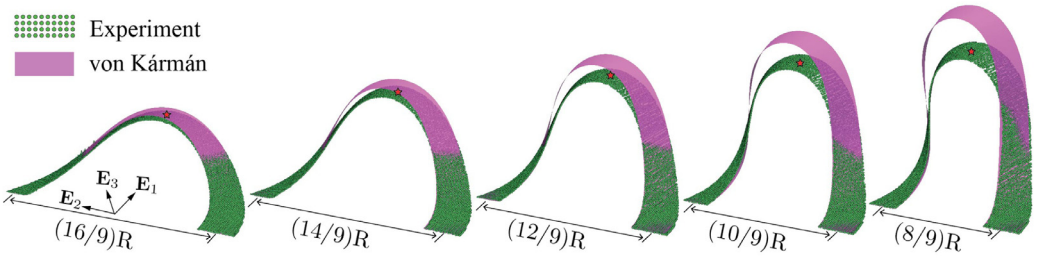

(a) A superposition of measured and predicted shapes of a pinched semi annular ribbon. Notice the progressive deterioration of model predictions.

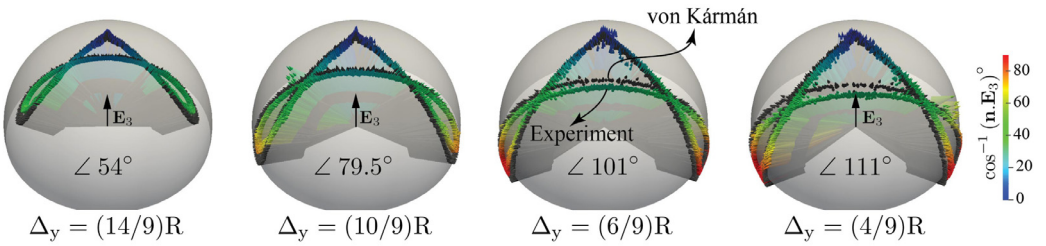

(b) Visualization of tips of normals to deformed ribbon surfaces. Notice that errors in the von Kármán model are larger away from the pole $\mathbf{E}_3$, which represents the normal to the undeformed surface. Extreme values of director rotations are indicated in each image.

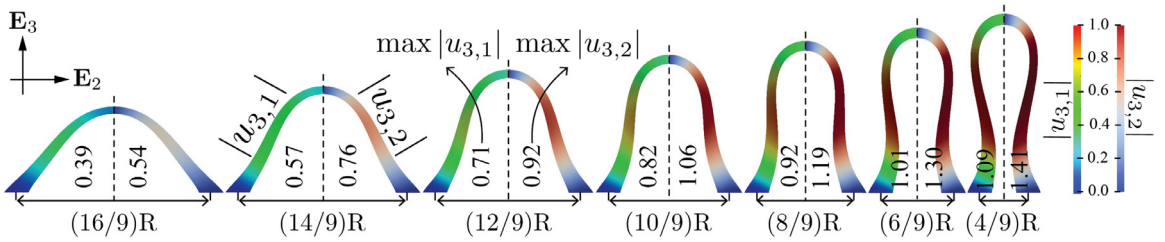

(c) Examining magnitudes of transverse displacement derivatives of the solution predicted by the von Kármán model. Both $|u_{3,1}|$ and $|u_{3,2}|$ are assumed to be much smaller than 1 when justifying the strain-displacement relationship in eq. (2). Large magnitudes observed in the solutions shown contradict these assumptions, indicating a lack of inner consistency.

Fig. 5. A comparison of experimental measurements and predictions of the von Kármán model for the pinched semi annulus experiment. Fig. (c) suggests that deviations from the assumptions in the model, which manifest even at small values of the imposed displacement Δ_y, are responsible for the poor predictions seen in (a) and (b).

between the centers of the clamps is denoted by Δ_y. When the ribbon is held in its undeformed state, the separation Δ_y equals the mean diameter 2R. The experiment consists in decreasing Δ_y by translating the posts holding the clamps, causing the ribbon to spontaneously buckle out of the $\mathbf{E}_1 - \mathbf{E}_2$ plane. The experiment hence examines post buckling deformations of the ribbon.

Fig. 4b plots the displacement at the midpoint along the centerline of the ribbon as Δ_y is decreased monotonically. Owing to reflection symmetry about the $\mathbf{E}_1 - \mathbf{E}_3$ plane, we only examine displacement components along the $\mathbf{E}_1$ and $\mathbf{E}_3$ axes. Data points from the experimental measurements (in green) show that the in-plane component u_1 varies approximately linearly with Δ_y, while the transverse component u_3 varies nonlinearly. The latter observation implies that models capable of predicting only linear relationships between u_3 and Δ_y are doomed to fail. This, of course, is in addition to the fact that geometrically linear models are incapable of predicting the buckled branch of the solution.

Fig. 5a compares ribbon shapes measured in the experiments with shapes predicted by the von Kármán model. Both Figs. 4b and 5a show that the model over predicts the transverse displacement, and that the deviation increases with progressive pinching. Furthermore, the relationship between Δ_y and u_3 appears to closely follow a cubic polynomial for the experimental data, and a quadratic one for the von Kármán model. Fig. 5b shows the loci of the tips of normals to deformed ribbon surfaces. By virtue of the Kirchhoff assumption, normals to the ribbon are material fibers (commonly termed as directors). Hence, points close to the pole of the unit sphere in the images represent fibers that remain unrotated from their initial orientation along $\mathbf{E}_3$— these fibers are located at the clamped ends of the ribbon. Reflection symmetry observed in the deformations in Fig. 5a are evident in the shapes of these loci as well.

The main reason for poor predictions of the von Kármán model in this experiment is a lack of inner consistency. Figs. 5b and c show that directors undergo large rotations and that transverse displacement derivatives ($u_{3,1}$, $u_{3,2}$) have significant magnitudes. At $\Delta_y = (10/9)\mathrm{R} = 100\,\mathrm{mm}$, for instance, when the clamps are displaced by a distance equal to the outer radius, we find that director rotations approach 80° and that derivatives of u_3 approach magnitudes close to 1. These values clearly contradict the strain-displacement relationship assumed in Eq. (2). This experiment serves as a reminder that even seemingly simple ribbon deformations can involve displacement magnitudes and director rotations that violate the kinematic assumptions underlying the von Kármán model.

4. Ribbons as nonlinear rods

The physical appearance of narrow ribbons motivates considering reduced order one-dimensional models for describing their mechanics. The early works of Sadowsky (Hinz and Fried, 2015) and Wunderlich (Todres, 2015), and the recent model of Dias and Audoly (2015) represent efforts in this direction. In this section, using comparisons with experimental measurements of ribbon deformations, we examine the merit of the well known and widely used approach of modeling ribbons as nonlinear elastic rods (Mahadevan and Keller, 1993; Morigaki et al., 2016; Sano and Wada, 2019; Yu and Hanna, 2019).

4.1. 2-director Cosserat rods

We adopt the special Cosserat theory of rods, described in Antman (1974) as a generalization of the Kirchhoff model. For the sake of brevity, we mention just the essential elements of the theory in the context of modeling a rectangular ribbon having a straight centerline in the unloaded state and assume a prismatic cross section. Detailed discussions of the theory, as well its extension to pre-curved rods can be found in Antman (1995, Chapter 8) and O'Reilly (2017, Chapter 6).

In the setting of the Cosserat theory, we consider a rectangular ribbon to be a *directed* curve whose configuration is specified by the coordinates of its centerline and by pairs of orthonormal material lines, referred to as director fields, that position its cross sectional planes. The undeformed state is specified parametrically as

$$(S, \xi_1, \xi_2) \mapsto \xi_1 \mathbf{E}_1 + \xi_2 \mathbf{E}_2 + S\mathbf{E}_3 \quad \text{where } (S, \xi_1, \xi_2) \in [0, \ell] \times [-w/2, w/2] \times [-h/2, h/2]. \tag{4}$$

In Eq. (4), we interpret $S \mapsto S\mathbf{E}_3$ as denoting the straight centerline of the ribbon. The directors located at each S represent material lines coinciding with the $\mathbf{E}_1$ and $\mathbf{E}_2$ axes, with the director $\mathbf{E}_1$ oriented along the width and $\mathbf{E}_2$ along the thickness as depicted in Fig. 6. An admissible deformation mapping for the ribbon has the form

$$(S, \xi_1, \xi_2) \mapsto \varphi_0(S) + \xi_1 \mathbf{t}_1(S) + \xi_2 \mathbf{t}_2(S), \tag{5}$$

where $S \mapsto \varphi_0(S) \in \mathbb{R}^3$ parameterizes the centerline in the deformed configuration and $S \mapsto (\mathbf{t}_1(S), \mathbf{t}_2(S))$ are the convected material directors. Each cross section is assumed to remain planar and undistorted, which is ensured in Eq. (5) by insisting that $\mathbf{t}_1$ and $\mathbf{t}_2$ remain mutually perpendicular unit vectors. The triad $\{\mathbf{t}_1(S), \mathbf{t}_2(S), \mathbf{t}_3(S) = \mathbf{t}_1(S) \times \mathbf{t}_2(S)\}$, commonly referred to as the *moving frame*, defines an orthonormal basis for $\mathbb{R}^3$ at each S. The moving frame is more conveniently described using a field of rotations $S \mapsto \Lambda(S)$ which is such that $\mathbf{t}_i(S) = \Lambda(S)\,\mathbf{E}_i$ for $i = 1, 2, 3$. Consequently, an admissible configuration of the ribbon is fully determined by $\Phi = (\varphi_0(S), \Lambda(S)) \in \mathbb{R}^3 \times \mathrm{SO}(3)$.

Orthonormality of the moving frame implies that we can find a skew-symmetric tensor field $S \mapsto \Omega(S)$ such that $d\mathbf{t}_i/dS = \Omega(S)\,\mathbf{t}_i(S)$ for $i = 1, 2, 3$. The axial vector of Ω, denoted by $\boldsymbol{\omega}$, satisfies $d\mathbf{t}_i(S)/dS = \boldsymbol{\omega}(s) \times \mathbf{t}_i(S)$. Resolving $\boldsymbol{\omega}$ in the moving basis as

$$\boldsymbol{\omega}(S) = \kappa_1(s)\,\mathbf{t}_1(S) + \kappa_2(S)\,\mathbf{t}_2(S) + \kappa_3(S)\,\mathbf{t}_3(S) \tag{6}$$

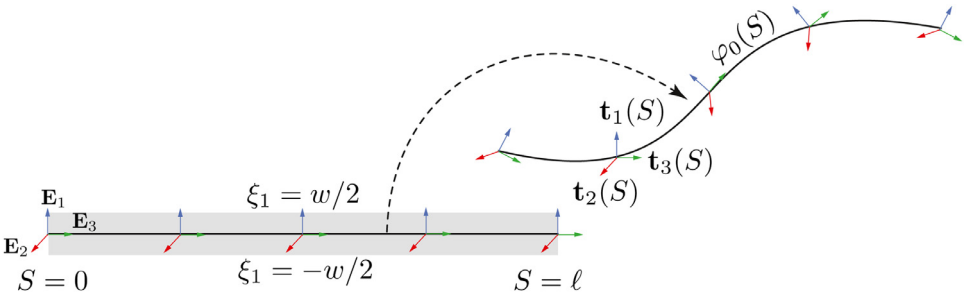

Fig. 6. The configuration of a rectangular ribbon modeled as a 2-director Cosserat rod is specified by the coordinates of its centerline φ_0 and by a field of orthonormal director frames $\{\mathbf{t}_1, \mathbf{t}_2, \mathbf{t}_3\}$.

identifies the flexural strains κ_1 and κ_2 about the principal axes of the cross section, and the torsional strain κ_3. The shear and extensional strains, on the other hand, are given by the components of $\boldsymbol{\gamma}(S) = d\varphi_0(S)/dS - \mathbf{t}_3(S)$. The material versions of the strains $\boldsymbol{\gamma}$ and $\boldsymbol{\omega}$ follow as

$$\boldsymbol{\Gamma} = \Lambda^{\mathrm{T}}\boldsymbol{\gamma} = \Lambda^{\mathrm{T}}\frac{d\varphi_0}{dS} - \mathbf{E}_3 \quad \text{and} \quad \mathbf{K} = \Lambda^{\mathrm{T}}\boldsymbol{\omega} = \kappa_i \mathbf{E}_i, \tag{7}$$

respectively. Presuming a linear relationship between the strain measures in Eq. (7) and the conjugate resultants, the strain energy functional in the model is given by

$$\begin{aligned} &\Pi^{\mathrm{CR}}[\Phi] \triangleq \Pi_{\mathrm{e}}^{\mathrm{CR}} + \Pi_{\mathrm{s}}^{\mathrm{CR}} + \Pi_{\mathrm{b}}^{\mathrm{CR}} \qquad (8)\\ \text{where}\quad &\Pi_{\mathrm{e}}^{\mathrm{CR}} = \frac{EA}{2}\int_{S=0}^{\ell}\left(\Lambda^{\mathrm{T}}\frac{d\varphi_0}{dS}\cdot\mathbf{E}_3 - 1\right)^2 dS,\\ &\Pi_{\mathrm{s}}^{\mathrm{CR}} = \frac{GA}{2}\int_{S=0}^{\ell}\left(\left(\Lambda^{\mathrm{T}}\frac{d\varphi_0}{dS}\cdot\mathbf{E}_1\right)^2 + \left(\Lambda^{\mathrm{T}}\frac{d\varphi_0}{dS}\cdot\mathbf{E}_2\right)^2\right) dS,\\ \text{and}\quad &\Pi_{\mathrm{b}}^{\mathrm{CR}} = \frac{1}{2}\int_{S=0}^{\ell}\left(\mathrm{EI}_1\kappa_1^2 + \mathrm{EI}_2\kappa_2^2 + \mathrm{GJ}\kappa_3^2\right) dS, \end{aligned}$$

where $\Pi_{\mathrm{e}}^{\mathrm{CR}}$ and $\Pi_{\mathrm{s}}^{\mathrm{CR}}$ represent energetic contributions from extension of the centerline and transverse shearing, while $\Pi_{\mathrm{b}}^{\mathrm{CR}}$ represents contributions from bending and twist. The extension and transverse shear stiffnesses scale with the area $\mathrm{A} = wh$ of the cross section. Since $h \ll w$, the area moments of inertia about the principal axes, namely, $\mathrm{I}_1 = wh^3/12$ and $\mathrm{I}_2 = hw^3/12$, yield drastically different bending modulii $\mathrm{EI}_1 \ll \mathrm{EI}_2$. In particular, it is far easier to bend about the $\mathbf{t}_1$ axis than about $\mathbf{t}_2$. The torsional stiffness GJ about $\mathbf{t}_3$ is computed using the polar moment of inertia J, which for the rectangular cross section is given by the approximate expression $\mathrm{J} \approx 32wh^3(16/3 - 3.361h/w)$.

Evidently, the main distinctions between Eq. (7) and the Kirchhoff rod model are the extensibility of the centerline and the possibility of transverse shear. In Kirchhoff rods, the normal $\mathbf{t}_3(S)$ to the cross section at $\varphi_0(S)$ coincides with the tangent $d\varphi_0(S)/dS$ to the centerline. The moving frame therefore equals the convected frame $\{\mathbf{t}_1, \mathbf{t}_2, d\varphi_0/dS\}$. Consequently, the strain measure $\boldsymbol{\Gamma}$ vanishes, and $\Pi_{\mathrm{e}}^{\mathrm{CR}} = 0$ and $\Pi_{\mathrm{s}}^{\mathrm{CR}} = 0$. The configuration of a Kirchhoff rod is therefore fully determined by the rotation $S \mapsto \Lambda(S)$ of the director frame, with the position of the centerline computed as $\varphi_0(S) = \int_{s=0}^{S}\Lambda(s)\mathbf{E}_3\, ds$. The linear constitutive relationship between curvatures/twist and conjugate stress couples in Eq. (8) is identical to that invoked for a Kirchhoff rod. However, section contact forces in the 2-director Cosserat model are determined constitutively, rather than as Lagrange multipliers imposing inextensibility and unshearability constraints in a Kirchhoff rod.

We do not expect extensional and transverse shear strains to be significant in bending-dominated experiments. We have verified this to be the case in simulations as well. In the context of our experiments therefore, the Cosserat rod theory effectively reduces to a Kirchhoff rod model in which inextensibility and unshearability are imposed weakly, with the extensional and shear stiffnesses serving as penalty parameters. In fact, changing these stiffnesses by an order of magnitude does not appreciably affect the numerical predictions. Hence, the conclusions we infer for the Cosserat rod model largely extend to the Kirchhoff rod model as well. In fact, the main reason behind adopting the Cosserat theory over the Kirchhoff rod model is the ease of implementation of the former, see Appendix B.2. While rotations in the Kirchhoff model can be computed using a variant of the algorithm discussed in Appendix B.2, the main difficulty stems from imposing displacement boundary conditions. Specifically, since $S \mapsto \Lambda(S)$ defines the configuration of the ribbon in the Kirchhoff model, imposing displacement boundary conditions manifests as a nonlinear integral constraint of the form $\int_{s=0}^{\ell}\Lambda(s)\mathbf{E}_3\, ds = \varphi_0(\ell)$. By explicitly introducing the centerline coordinates as an independent unknown, the Cosserat model helps avoid such constraints.

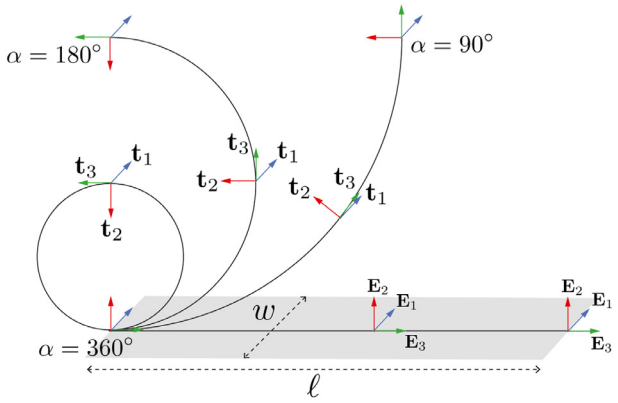

Fig. 7. When one end of a rectangular ribbon is clamped and the other end is rotated about the $\mathbf{E}_1$ axis parallel to the width, the centerline of the ribbon bends into an arc of a circle. Rotating the section $S = \ell$ by the angle 2π causes the ribbon to roll up into a cylinder. Both Kirchhoff and Cosserat rod models reproduce this solution exactly.

4.2. Rolled up rectangular ribbon

Perhaps the most well known solution of a rectangular ribbon undergoing large displacements and rotations is that in which one edge of the ribbon is clamped while the other end is subjected to a rotation/moment, causing the centerline of the ribbon to roll up into an arc of a circle. When the end moment (or rotation angle) is sufficiently large, the ribbon assumes the shape of a cylinder. We recall this example because it helps to highlight the *geometric exactness* of the Cosserat rod theory, besides providing a simple context in which to examine the strain measures in the model. We note that the von Kármán theory cannot describe this solution unless the imposed moment/rotation is assumed to be sufficiently small.

In the following, we demonstrate that the deformation

$$\varphi_0(S) = \mathrm{r}\sin(\alpha S/\ell)\,\mathbf{E}_2 + \mathrm{r}(1-\cos(\alpha S/\ell))\,\mathbf{E}_3 \quad \text{and} \quad \Lambda(S) = \begin{bmatrix} 1 & 0 & 0 \\ 0 & \sin(\alpha S/\ell) & \cos(\alpha S) \\ 0 & -\cos(\alpha S/\ell) & \sin(\alpha S/\ell) \end{bmatrix}, \tag{9}$$

illustrated in Fig. 7 representing the centerline deformed into an arc of a circle of radius $\mathrm{r} = \ell/\alpha$ when the end $S = \ell$ is rotated by a prescribed angle $\alpha > 0$, is a solution of the Cosserat rod model. The deformed mid surface of the ribbon, parameterized as $(S, \xi_1) \mapsto \varphi_0(S) + \xi_1 \Lambda(S)\mathbf{E}_1$, represents the section of a cylindrical surface of radius r with axis parallel to $\mathbf{E}_1$. The cylindrical mid surface is bounded between tangent planes normal to $\mathbf{E}_2$ at $S = 0$ and to $\cos\alpha\,\mathbf{E}_2 - \sin\alpha\mathbf{E}_3$ at $S = \ell$. When $\alpha = 2\pi$, Eq. (9) represents the ribbon rolled up into a cylinder of radius $\ell/2\pi$.

First, we note that Eq. (9) does not involve any extension or transverse shear:

$$\frac{d\varphi_0}{dS} = \cos(\alpha S/\ell)\,\mathbf{E}_2 + \sin(\alpha S/\ell)\mathbf{E}_3 \;\Rightarrow\; \boldsymbol{\Gamma} = \Lambda^{\mathrm{T}}\frac{d\varphi_0}{dS} - \mathbf{E}_3 = 0 \;\Rightarrow\; \mathbf{N} = 0. \tag{10}$$

Computing the curvature strains, we have

$$\Omega = \frac{d\Lambda}{dS}\Lambda^{\mathrm{T}} = \frac{\alpha}{\ell}\begin{bmatrix} 0 & 0 & 0 \\ 0 & 0 & -1 \\ 0 & 1 & 0 \end{bmatrix} \;\Rightarrow\; \boldsymbol{\omega} = (\alpha/\ell)\,\mathbf{E}_1 \;\Rightarrow\; \mathbf{K} = \Lambda^{\mathrm{T}}\boldsymbol{\omega} = (\alpha/\ell)\mathbf{E}_1 \;\Rightarrow\; \mathbf{M} = (\alpha/\ell)\mathrm{EI}_1\,\mathbf{E}_1. \tag{11}$$

Then, evaluating the statement of virtual work in for an arbitrary variation $(\boldsymbol{\eta}_0, \boldsymbol{\vartheta})$, we get (see Eq. (38a) in Appendix B.2)

$$G(\Phi, (\boldsymbol{\eta}_0, \boldsymbol{\vartheta})) = \mathrm{EI}_1\left(\frac{\alpha}{\ell}\right)\int_{S=0}^{\ell}\mathbf{E}_1\cdot\Lambda^{\mathrm{T}}\frac{d\boldsymbol{\vartheta}}{dS}\,dS = \mathrm{EI}_1\left(\frac{\alpha}{\ell}\right)\int_{S=0}^{\ell}\frac{d(\boldsymbol{\vartheta}\cdot\mathbf{E}_1)}{dS}\,dS = (\boldsymbol{\vartheta}(\ell) - \boldsymbol{\vartheta}(0))\cdot\mathbf{E}_1 = 0, \tag{12}$$

where we have used the fact that $\boldsymbol{\vartheta}(0) = \boldsymbol{\vartheta}(\ell) = 0$ owing to the prescribed rotations at the ends. Eq. (12) verifies that the deformation in Eq. (9) is a stationary point of Π^{CR}. Eq. (10) shows that Eq. (9) is in fact a solution of the Kirchhoff rod model as well. Thanks to the cylindrical symmetry of the solution, Eq. (9) can also be derived using the planar *Elastica* model (Frisch-Fay, 1962). This simple example highlights the potency of modeling ribbons undergoing large displacements and rotations as nonlinear rods.

4.3. Transversely displaced annular ribbon and pinched semi-annular ribbon experiments

Next, we revisit the experiments discussed in Sections 3.2 and 3.3 to compare predictions of the Cosserat rod model with measurements. Fig. 8a shows the annular ribbon from the experiment described in Section 3.2, when the transverse displacement Δ_z equals the outer radius $\mathrm{R}_0 = 100\,\mathrm{mm}$. The model prediction is shown in blue and the computed centerline is highlighted using circular markers. Examining the mean curvature distribution helps us inspect additional details.

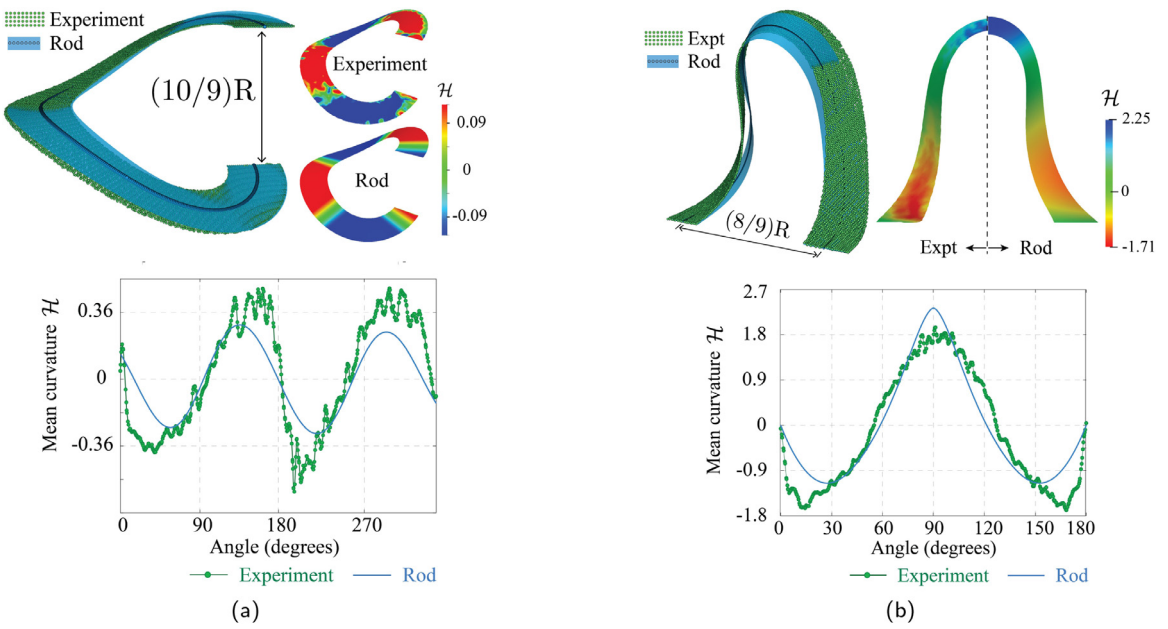

Fig. 8. Comparisons of measured and Cosserat rod model predictions for the (a) transversely displaced annulus and the (b) pinched semi annulus experiments.

Mean curvature from a Cosserat rod solution. Setting $\xi_2 = 0$ in Eq. (5) shows that the mid surface of a deformed ribbon modeled as a Cosserat rod is the ruled surface

$$(S, \xi_1) \mapsto \boldsymbol{\phi}(S, \xi_1) = \varphi_0(S) + \xi_1 \mathbf{t}_1(S), \tag{13}$$

whose mean curvature is given by do Carmo (2016):

$$H(S, \xi_1) = \frac{1}{2} \frac{eG + gE - 2fF}{EG - F^2}, \tag{14}$$

where the components of the first and second fundamental forms are

$$\mathbf{I} = \begin{bmatrix} E & F \\ F & G \end{bmatrix} = \begin{bmatrix} \boldsymbol{\phi}_{,S} \cdot \boldsymbol{\phi}_{,S} & \boldsymbol{\phi}_{,S} \cdot \boldsymbol{\phi}_{,\xi_1} \\ \cdot & \boldsymbol{\phi}_{,\xi_1} \cdot \boldsymbol{\phi}_{,\xi_1} \end{bmatrix} \quad \text{and} \quad \mathbf{II} = \begin{bmatrix} e & f \\ f & g \end{bmatrix} = \begin{bmatrix} \boldsymbol{\phi}_{,SS} \cdot \mathbf{n} & \boldsymbol{\phi}_{,S\xi_1} \cdot \mathbf{n} \\ \cdot & \boldsymbol{\phi}_{,\xi_1\xi_1} \cdot \mathbf{n}, \end{bmatrix} \tag{15}$$

and $\mathbf{n}$ is the unit normal to the mid surface. A few observations help simplify Eq. (14). Assuming extensional and transverse shear strains to be sufficiently small, we set $\mathbf{t}_3 = \varphi_0'$. Then,

$$F = \boldsymbol{\phi}_{,S} \cdot \boldsymbol{\phi}_{,\xi_1} = (\mathbf{t}_3 + \xi_1 \mathbf{t}_1') \cdot \mathbf{t}_1 = 0, \quad G = \boldsymbol{\phi}_{,\xi_1} \cdot \boldsymbol{\phi}_{,\xi_1} = \mathbf{t}_1 \cdot \mathbf{t}_1 = 1 \quad \text{and} \quad g = \boldsymbol{\phi}_{,\xi_1\xi_1} \cdot \mathbf{n} = 0,$$

which reduces the mean curvature to $H = e/(2E)$. It therefore suffices to compute e and E from the numerical solution. We have

$$E = (\mathbf{t}_3 + \xi_1 \mathbf{t}_1') \cdot (\mathbf{t}_3 + \xi_1 \mathbf{t}_1') = 1 + 2\xi_1 \underbrace{\mathbf{t}_1' \cdot \mathbf{t}_3}_{-\kappa_2} + \xi_1^2 \underbrace{\mathbf{t}_1' \cdot \mathbf{t}_1'}_{\kappa_2^2 + \kappa_3^2} = (1 - \xi_1\kappa_2)^2 + \xi_1^2\kappa_3^2,$$

which, notably, is strictly non-negative. With

$$\boldsymbol{\phi}_{,S} \times \boldsymbol{\phi}_{,\xi_1} = (\mathbf{t}_3 + \xi_1 \mathbf{t}_1') \times \mathbf{t}_1 = (1 - \xi_1\kappa_2)\mathbf{t}_2 - \xi_1\kappa_3\mathbf{t}_3 \;\Rightarrow\; \mathbf{n} = \frac{(1 - \xi_1\kappa_2)\mathbf{t}_2 - \xi_1\kappa_3\mathbf{t}_3}{\sqrt{E}}, \tag{16}$$

we compute $e = \boldsymbol{\phi}_{,SS} \cdot \mathbf{n}$ as

$$e = \frac{\big((\mathbf{t}_3' + \xi_1\mathbf{t}_1'') \cdot ((1 - \xi_1\kappa_2)\mathbf{t}_2 - \xi_1\kappa_3\mathbf{t}_3)\big)}{\sqrt{E}} = \frac{\big((1 - \xi_1\kappa_2)(\mathbf{t}_2 \cdot \mathbf{t}_3') + \xi_1(1 - \xi_1\kappa_2)(\mathbf{t}_1'' \cdot \mathbf{t}_2) - \xi_1^2\kappa_3(\mathbf{t}_1'' \cdot \mathbf{t}_3)\big)}{\sqrt{E}}.$$

Now, $\mathbf{t}_2 \cdot \mathbf{t}_3' = -\kappa_1$ and by the chain rule, $\mathbf{t}_1'' \cdot \mathbf{t}_2 = (\mathbf{t}_1' \cdot \mathbf{t}_2)' - \mathbf{t}_1' \cdot \mathbf{t}_2' = \kappa_3' - \kappa_1\kappa_2$. Similarly, $\mathbf{t}_1'' \cdot \mathbf{t}_3 = -\kappa_2' + \kappa_1\kappa_3$. Hence, we get

$$e = \frac{1}{\sqrt{E}}\big(-(1 - \xi_1\kappa_2)\kappa_1 + \xi_1(1 - \xi_1\kappa_2)(\kappa_3' - \kappa_1\kappa_2) + \xi_1^2\kappa_3(\kappa_2' - \kappa_1\kappa_3)\big).$$

In particular, along the centerline $\xi_1 = 0$, the mean curvature simplifies to $H(S, 0) = -\kappa_1$.

Fig. 8a shows contours of the mean curvature on the deformed surface and plots of its profile along the centerline of the ribbon computed from model predictions using the expressions derived above. Contours of $\mathcal{H}$ computed from the experimental measurement shows that the mean curvature is a weak function of the coordinate ξ_1, suggesting that the ribbon deformation is effectively rod-like. Inspecting the profiles of $\mathcal{H}$ along the centerline, we find that the values computed from model predictions and from experimental measurements agree well. We find small differences in magnitudes, but the locations of extrema and zero crossings in the two profiles are quite close.

Fig. 8b compares analogous data for the pinched semi annulus experiment, when the separation Δ_y between the ends equals the inner radius $R_i = 80\,\text{mm}$. The predictions for ribbon shape and the mean curvature closely follow the experimental measurements, unlike in the case of the von Kármán theory (Fig. 4b). The rod model imposes severe restrictions on the kinematics of the ribbon along the narrow width, but retains accurate geometric descriptions of displacements and rotations along the centerline of the ribbon.

4.4. Unfurled annular ribbon

The discussions in Sections 4.2 and 4.3 provide reassuring evidence of the merit behind modeling slender ribbons as nonlinear rods. The next experiment provides evidence to the contrary. Fig. 9a depicts the setup used in the unfurled annulus experiment. Therein, an annular ribbon having a mean radius of 90 mm and a width of 20 mm is slit along a radial line. The straight edges of the ribbon are held in clamps that are initially oriented along the $\mathbf{E}_1$ axis. The clamps are rotatable about the $\mathbf{E}_3$ axis normal to the undeformed plane of the ribbon, and translatable along a lead screw running parallel to the $\mathbf{E}_2$ direction. The experiment consists in rotating the ribbon's edges by 180° and examining its deformation as the clamps are translated. We mention a few preliminary remarks concerning the resulting deformation of the ribbon.

- Rotating or translating the clamps necessarily induces compression along the outer periphery of the ribbon. For this reason, we expect planar solutions to be unstable. This manifests in the experiments as well— the ribbon buckles out of its initial plane even for small displacements and/or rotations of its ends. By virtue of the boundary conditions imposed, the clamped edges remain in the initial plane of the ribbon throughout the deformation. Yet, the ribbon deforms into complex three dimensional shapes. The experiment therefore helps examine deformations far into the post buckling regime.
- The deformations in Fig. 9a and b bear superficial resemblances to shapes of *Godet* surfaces introduced in Nechaev and Voituriez (2001) to model surface deformations induced by a prescribed metric. Note that the undulations observed here are caused by the difference between the inner and outer circumferences of the ribbon, not by a metric-altering mechanism such as growth, diffusion damage or residual stresses (Marder et al., 2003; Sharon and Efrati, 2010; Sharon et al., 2002).
- Owing to the nature of the boundary conditions imposed, we expect the deformation to be symmetric about the $\mathbf{E}_1 - \mathbf{E}_3$ plane. This is observed in our experiments as well, although it is possible to break symmetry by perturbing the ribbon to alternate equilibrium states. We discuss the possibility of multiple solutions and provide examples of deformations lacking reflection symmetry in Section 7.
- This experiment complements the example of a rectangular ribbon rolled up into a cylinder discussed in Section 4.2 in the sense that it effectively attempts to straighten out the ribbon's circular centerline. The clamped edges, however, are parallel to the axis of rotation in the example in Section 4.2, but orthogonal to the rotation axis in Fig. 9a.

Fig. 9b compares ribbon shapes predicted by the Cosserat rod model with experimental measurements as the separation Δ_y between the ribbon edges is progressively increased. For ease of visualization, the figure shows projections of these shapes on the $\mathbf{E}_1 - \mathbf{E}_2$ and $\mathbf{E}_2 - \mathbf{E}_3$ planes. At first glance, the predictions appear to be reasonably good, although deviations comparable to the width of the ribbon are evident. Since the ribbon straightens out progressively with increasing distance Δ_y, it is imprudent to rely only on shape comparisons to evaluate the accuracy of the rod model. Examining profiles of the mean curvature along the centerline of the ribbon in Fig. 9c reveals startling qualitative differences. The profile predicted by the rod model (equal to $-\kappa_1$) shows localization at the clamped ends and at the center, and a nearly vanishing curvature elsewhere. Curvatures computed from experimental measurements indicate otherwise. At $\Delta_y = 250\,\text{mm}$, the measured data suggests that it is energetically preferable for the ribbon to adopt a configuration in which the mean curvature is piecewise constant along the centerline. At larger separations of 300 mm and 470 mm, the ribbon switches more frequently between positive and negative mean curvatures of approximately equal magnitudes.

The comparisons in Fig. 9 suggests that the set of admissible ribbon configurations in the rod model is not sufficiently "rich" to accommodate the state of combined bending and twist that the ribbon exhibits in this experiment. Fig. 10 shows that increasing the width of the ribbon from 20 mm to 35 mm, while retaining the mean radius of 90 mm, exacerbates the shortcomings of the kinematic assumptions. Comparing the mean curvature profiles at the separation $\Delta_y = 250\,\text{mm}$ shows that the ribbon retains a roughly piecewise constant mean curvature, just as was the case in Fig. 9c with the narrower ribbon. Not only does the rod model predict sharp localization at the ends and at the center, it also predicts six zero crossings in the profile. The experiment reveals just two.

It can be argued that the discrepancies observed in Figs. 9 and 10 stems from the width of the ribbon being relatively large. Setting the length scale ℓ to be the circumference $\pi(R_i + R_0)$ of the centerline, the aspect ratios w/ℓ are approximately 0.035 and 0.062 for widths $w = 20\,\text{mm}$ and $w = 35\,\text{mm}$, respectively. These values are comparable to the ratio of $1/20 = 0.05$

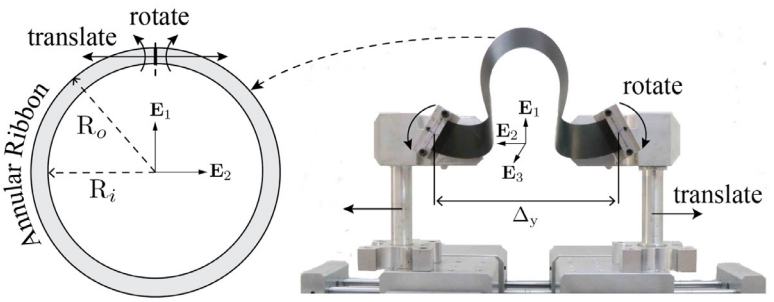

(a) Setup for the unfurled annulus experiment. Clamped edges of the ribbon are rotated by 180° about the $\mathbf{E}_3$ axis and translated along the $\mathbf{E}_2$, causing the ribbon to buckle out of plane and deform into complex 3D shapes.

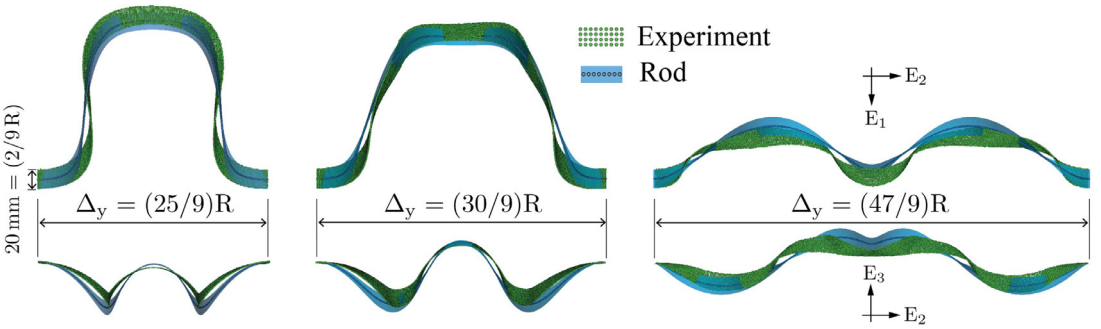

(b) Comparisons of ribbon shapes measured from experiments with deformations predicted by the Cosserat rod model. The centerline of the ribbon is highlighted using circular markers.

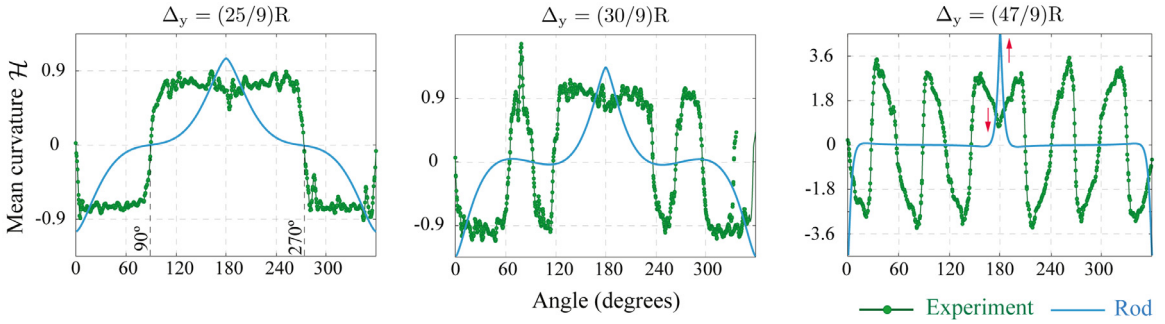

(c) Examining the mean curvature distribution along the centerline of the ribbon: the rod model predicts localization at the ends and at the midpoint of the centerline, while measured data suggests that the ribbon prefers to alternate between positive and negative curvatures of approximately equal magnitude. In the case $\Delta_y = 470\,\text{mm}$, the red arrows shown draw attention to the fact that the rod model predicts a maximum at the center while the experimental data reveals a local minimum.

Fig. 9. The unfurled annular ribbon experiment highlights a scenario in which the kinematic assumptions underlying the Cosserat rod model render it incapable of describing 3D shapes that an annular ribbon can assume.

that is commonly cited in the context of beam theories. In this sense, the aspect ratios used in the experiment are within bounds of engineering applications in which ribbon-like structures are likely to be of interest. Rather, the main shortcoming of the rod model stems from lumping details of the highly anisotropic cross section into stiffness parameters. Fig. 15b shown later suggests that the ansatz for cross section kinematics in the Cosserat rod theory results in significant errors in the strain energy when describing general deformations of ribbon-like structures.

5. Ribbons as Cosserat plates

With compelling evidence from Section 3 on the need for accurate descriptions of large displacements and rotations, and from Section 4 on the perils of imposing severe kinematic restrictions along the width, we consider modeling ribbons as 1-director Cosserat plates next. In the following, we discuss the main elements of theory in the context of homogeneous

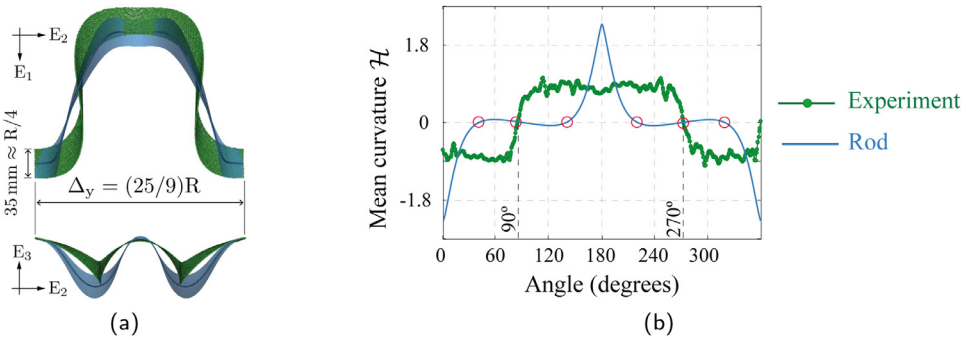

Fig. 10. Unfurling a wide ribbon amplifies the shortcomings of the rod model in predicting ribbon deformations. Both the displacement and mean curvature predictions show large deviations from the experimental data. In (b), notice that the rod model predicts six zero crossings in the mean curvature along the centerline, while the experiment reveals only two.

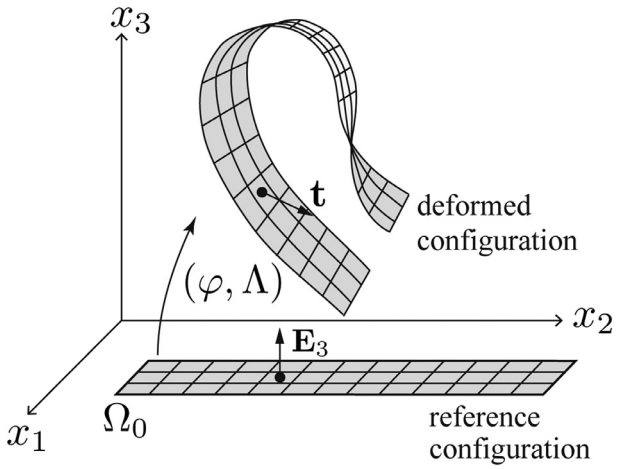

Fig. 11. Modeling a ribbon as a 1-director Cosserat plate. An admissible configuration Φ is specified by the coordinates φ of the mid surface and a field of inextensible material directors $\mathbf{t}$.

plates having a uniform thickness. Without loss of generality, we assume a Cartesian system of coordinates since this is most convenient for numerical implementation. We refer to Antman (1995) for detailed discussions of the theory, its generalization to extensible directors, and for its derivation in general curvilinear coordinate systems starting from the three dimensional problem of nonlinear elasticity with assumed kinematics.

5.1. 1-director Cosserat plates

The reference configuration of a ribbon modeled as a 1-director Cosserat plate is specified as

$$(x_1, x_2, x_3) \mapsto x_1\,\mathbf{E}_1 + x_2\,\mathbf{E}_2 + x_3\,\mathbf{E}_3, \quad \text{where } (x_1, x_2) \in \Omega_0,\ -h/2 \le x_3 \le h/2. \tag{17}$$

As depicted in Fig. 11, the set $\Omega_0 \subset \mathbb{R}^2$ is the mid surface lying in the plane spanned by the $\mathbf{E}_1 - \mathbf{E}_2$ axes. At each point on the mid surface, the ribbon is endowed with a material director that is oriented along $\mathbf{E}_3$, coinciding with the direction of the ribbon's thickness. An admissible deformation mapping has the form

$$(x_1, x_2, x_3) \mapsto \varphi(x_1, x_2) + x_3\,\mathbf{t}(x_1, x_2), \tag{18}$$

in which $(x_1, x_2) \mapsto \varphi(x_1, x_2) \in \mathbb{R}^3$ and $(x_1, x_2) \mapsto \mathbf{t}(x_1, x_2) \in \mathbb{R}^3$ describe respectively, the mid surface of the ribbon and its director field in the deformed configuration. While Eq. (18) already stipulates that directors remain straight during deformation, we will additionally insist that they remain inextensible as well by assuming that $\mathbf{t} \cdot \mathbf{t} = 1$. Consequently, an admissible configuration of the ribbon is specified by $\Phi = (\varphi, \mathbf{t}) \in \mathbb{R}^3 \times \mathbb{S}^2$, where $\mathbb{S}^2$ is the unit sphere in $\mathbb{R}^3$. By not requiring directors to remain normal to the mid surface during deformation, we permit the possibility of transverse shear. This aspect of the general theory is insignificant in our experiments involving thin ribbons, and is retained mainly for the simplifications it affords when computing finite element approximations.

Examining the statement of virtual power with kinematics given by Eq. (18) helps identify the membrane, shear and bending strain measures and their conjugate stress/couple resultants in the model. To this end, it is convenient to denote

the tangents to the mid surface $\varphi_{,1}$ and $\varphi_{,2}$ by $\mathbf{g}_1$ and $\mathbf{g}_2$, respectively, which, along with $\mathbf{g}_3 = \mathbf{t}$, defines a moving basis. We denote the corresponding dual basis by $\{\mathbf{g}^1, \mathbf{g}^2, \mathbf{g}^3\}$. Following (Simo and Fox, 1989, Sections 4, 5), strain measures are given by

$$\boldsymbol{\varepsilon} = \frac{1}{2}(\varphi_{,i}\cdot\varphi_{,j} - \delta_{ij})\,\mathbf{g}^i\otimes\mathbf{g}^j, \quad \boldsymbol{\gamma} = (\varphi_{,i}\cdot\mathbf{t})\,\mathbf{g}^i \quad \text{and} \quad \boldsymbol{\kappa} = (\varphi_{,i}\cdot\mathbf{t}_{,j})\,\mathbf{g}^i\otimes\mathbf{g}^j, \quad i,j=1,2, \tag{19}$$

with corresponding effective stress resultants denoted by $\mathbf{n} = n^{ij}\mathbf{g}_i\otimes\mathbf{g}_j$, $\mathbf{q} = q^i g_i$ and $\mathbf{m} = m^{ij}\mathbf{g}_i\otimes\mathbf{g}_j$, respectively. The membrane strain $\boldsymbol{\varepsilon}$ measures the deviation of the surface metric, given by its first fundamental form with components $g_{ij} = \varphi_{,i}\cdot\varphi_{,j}$, from the identity metric corresponding to Eq. (17) in the undeformed state. Since we expect the director field $\mathbf{t}$ to coincide with the unit normal $\mathbf{n} = (\mathbf{g}_1\times\mathbf{g}_2)/\|\mathbf{g}_1\times\mathbf{g}_2\|$ for thin ribbons, we expect transverse shear strains $\gamma_i = \varphi_i\cdot\mathbf{t} \approx \varphi_i\cdot\mathbf{n}$ to be vanishingly small. Then, neglecting transverse shear, we have $\varphi_{,i}\cdot\mathbf{t}_j \approx \varphi_{,i}\cdot\mathbf{n}_j$ so that the bending strain $\boldsymbol{\kappa}$ coincides with the second fundamental form of the mid surface.

We assume a constitutive relationship between the conjugate stress resultants and strain measures of the form

$$\mathrm{J}n^{ij} = \frac{\mathrm{E}h}{1-\nu^2}\mathbb{H}^{ijkL}\varepsilon_{kL}, \quad \mathrm{J}q^i = \mathrm{G}h\delta^{ij}\gamma_j \quad \text{and} \quad \mathrm{J}m^{ij} = \frac{\mathrm{E}h^3}{12(1-\nu^2)}\mathbb{H}^{ijkL}\kappa_{kL},$$
$$\text{where} \quad \mathbb{H}^{ijkL} = \nu\delta^{ij}\delta^{kL} + \frac{(1-\nu)}{2}(\delta^{ik}\delta^{jL} + \delta^{iL}\delta^{jk}), \quad i,j=1,2, \tag{20}$$

and $\mathrm{J} = \|\mathbf{g}_1\times\mathbf{g}_2\|$ is the Jacobian of the mid surface deformation $\Omega_0 \mapsto \Omega = \varphi(\Omega_0)$. Since we are concerned with ribbons having a flat reference configuration, strain measures in Eq. (19) are stated assuming that the reference and unstressed configurations coincide and invoking the trivial parameterization in Eq. (17) for Ω_0. Similarly, the constitutive relationship stated in Eq. (20) assumes a system of Cartesian coordinates over the reference configuration. Generalizations of Eqs. (19) and (20) to accommodate curvilinear/parameterized unstressed configurations are well known, and can be found in Simo and Fox (1989) for instance.

As expected, the membrane and shear modulii in Eq. (20) scale as h, while the bending modulii scale as h^3. Equilibrium configurations of the ribbon are extremizers of the energy functional expressed as a sum of membrane, transverse shear and bending contributions:

$$\begin{aligned}
&\Pi^{\mathrm{CS}} = \Pi^{\mathrm{CS}}_{\mathrm{m}} + \Pi^{\mathrm{CS}}_{\mathrm{s}} + \Pi^{\mathrm{CS}}_{\mathrm{b}}\\
\text{where}\quad &\Pi^{\mathrm{CS}}_{\mathrm{m}} = \frac{1}{2}\int_\Omega n^{ij}\varepsilon_{ij}\,d\Omega = \frac{\mathrm{E}h}{2(1-\nu^2)}\int_{\Omega_0}\left(\nu\,\mathrm{Tr}[\boldsymbol{\varepsilon}]^2 + (1-\nu)\,\boldsymbol{\varepsilon}:\boldsymbol{\varepsilon}\right)d\Omega_0,\\
&\Pi^{\mathrm{CS}}_{\mathrm{s}} = \frac{1}{2}\int_\Omega q^i\gamma_i\,d\Omega = \frac{\mathrm{E}h}{4(1+\nu)}\int_{\Omega_0}(\boldsymbol{\gamma}\cdot\boldsymbol{\gamma})\,d\Omega_0,\\
&\Pi^{\mathrm{CS}}_{\mathrm{b}} = \frac{1}{2}\int_\Omega m^{ij}\kappa_{ij}\,d\Omega = \frac{\mathrm{E}h^3}{24(1-\nu^2)}\int_{\Omega_0}\left(\nu\,\mathrm{Tr}[\boldsymbol{\kappa}]^2 + (1-\nu)\,\boldsymbol{\kappa}:\boldsymbol{\kappa}\right)d\Omega_0.
\end{aligned} \tag{21}$$

Relation to 2-director Cosserat rods. It is instructive to compare Eq. (18) with the kinematic assumptions invoked in the Cosserat rod model in Eq. (5). For simplicity, let us assume the case of a rectangular ribbon, so that $\Omega_0 = [0,\ell]\times[-w/2, w/2]$ in which the centerline coincides with the $\mathbf{E}_1$ axis and the direction of the width with $\mathbf{E}_2$. Identifying the coordinates S, ξ_1 and ξ_2 in Eq. (5) with x_1, x_2 and x_3 respectively in Eq. (18), we recover the kinematics of the 2-director Cosserat rod by setting $\varphi(x_1,x_2) = \varphi_0(x_1) + x_2\mathbf{t}_1(x_1)$. In this sense, the 2-director Cosserat rod model is a special case of the 1-director Cosserat plate with restricted kinematics along the width. We refer to Rubin (2013) for a unified description of Cosserat rod and plate models.

As a specific example of this relationship between the two models, we revisit the problem of the rolled up rectangular ribbon discussed in Section 4.2. Assuming the centerline to be oriented along $\mathbf{E}_1$, the width along $\mathbf{E}_2$ and the thickness along $\mathbf{E}_3$, the deformation mapping for the mid surface in Eq. (9) is recast as

$$\varphi(x_1,x_2) = \mathrm{r}\sin(\alpha x_1/\ell)\,\mathbf{E}_1 + x_2\,\mathbf{E}_2 + \mathrm{r}\,(1-\cos(\alpha x_1/\ell))\,\mathbf{E}_3. \tag{22}$$

Similarly, identifying the director field $\mathbf{t}_2(S)$ with $\mathbf{t}$ in Eq. (18), we get

$$\mathbf{t}(x_1,x_2) = -\sin(\alpha x_1/\ell)\,\mathbf{E}_1 + \cos(\alpha x_1/\ell)\,\mathbf{E}_3, \tag{23}$$

Evidently, the configuration $\Phi = (\varphi,\mathbf{t})$ represents the same deformation of the ribbon as (φ_0, Λ) in Eq. (9)– the edge $x_1 = 0$ is held clamped, the edge $x_1 = \ell$ is rotated by an angle α and the mid surface $\varphi(\Omega_0)$ represents a cylinder of radius r with axis parallel to $\mathbf{E}_2$. As required, directors in Eq. (23) remain straight and unextended from the reference irrespective of the value of α.

For the deformation defined by Eqs. (22) and (23), let us examine the strain measures in Eq. (19). Since

$$\mathbf{g}_1 = \varphi_{,1} = \cos(\alpha x_1/\ell)\,\mathbf{E}_1 + \sin(\alpha x_1/\ell)\,\mathbf{E}_3 \quad \text{and} \quad \mathbf{g}_2 = \varphi_{,2} = \mathbf{E}_2,$$

we find that $\mathbf{g}_i\cdot\mathbf{g}_j = \delta_{ij}$. Hence all components of the membrane strain $\boldsymbol{\varepsilon}$ vanish, demonstrating the fact that φ is an isometry. Since directors are orthogonal to the mid surface by virtue of Eqs. (22) and (23), we have $\mathbf{g}_i\cdot\mathbf{t} = 0$ so that transverse

shear strains vanish as well. Noting that $\mathbf{t}_{,1} = -(\cos(\alpha x_1/\ell)\,\mathbf{E}_1 + \sin(\alpha x_1/\ell)\,\mathbf{E}_3)/\mathrm{r}$ and $\mathbf{t}_{,2} = 0$, components of the bending strain follow as

$$\kappa_{11} = \mathbf{g}_1 \cdot \mathbf{t}_{,1} = -1/\mathrm{r}, \quad \kappa_{12} = \mathbf{g}_1 \cdot \mathbf{t}_{,2} = 0 = \kappa_{21} \quad \text{and} \quad \kappa_{22} = \mathbf{g}_2 \cdot \mathbf{t}_{,2} = 0. \tag{24}$$

Eq. (24) indicates, as expected, a uniform bending strain κ_{11} whose magnitude equals the curvature 1/r of the deformed cylindrical surface.

Relation to plate models. Next, if we assume that directors in Eq. (18) undergo only small rotations, say by angles ψ_2 and $-\psi_1$ about the $\mathbf{E}_1$ and $\mathbf{E}_2$ axes respectively, material lines along $\mathbf{E}_3$ deform as

$$\mathbf{E}_3 \mapsto \mathbf{t} \approx \left(\mathbf{I} + \begin{bmatrix} 0 & 0 & -\psi_1 \\ 0 & 0 & -\psi_2 \\ \psi_1 & \psi_2 & 0 \end{bmatrix}\right)\mathbf{E}_3 = -\psi_1\,\mathbf{E}_1 - \psi_2\,\mathbf{E}_2 + \mathbf{E}_3. \tag{25}$$

Denoting the mid surface displacement by $\mathbf{u}(x_1, x_2) \in \mathbb{R}^3$ so that $\varphi(x_1, x_2) = (x_1, x_2) + \mathbf{u}(x_1, x_2)$, and substituting Eq. (25) into Eq. (18), we get the displacement field in the Cosserat plate model to be of the form

$$\mathbf{U}(x_1, x_2, x_3) = (u_1(x_1, x_2) - x_3\psi_1(x_1, x_2))\,\mathbf{E}_1 + (u_2(x_1, x_2) - x_3\psi_2(x_1, x_2))\,\mathbf{E}_2 + (x_3 + u_3(x_1, x_2))\,\mathbf{E}_3, \tag{26}$$

which is precisely the kinematics assumed in the linear Reissner-Mindlin plate theory. If we additionally assume that displacements $\mathbf{u}$ remain small and that directors remain normal to the mid surface during deformation in Eq. (26), we can set $\psi_1 = u_{3,1}$ and $\psi_2 = u_{3,2}$ in Eq. (26) to get

$$\mathbf{U}(x_1, x_2, x_3) = (u_1(x_1, x_2) - x_3u_{3,1}(x_1, x_2))\,\mathbf{E}_1 + (u_2(x_1, x_2) - x_3u_{3,2}(x_1, x_2))\,\mathbf{E}_2 + (x_3 + u_3(x_1, x_2))\,\mathbf{E}_3, \tag{27}$$

which is the form of the displacement field assumed in the classical Kirchhoff-Love and von Kármán plate theories.

To help highlight the approximations invoked in the strain-displacement relationship in von Kármán model in Eq. (2), let us examine the membrane and bending strains in Eq. (19) for the particular form of the displacement field in Eq. (27). Identifying coordinates of the deformed mid surface in Eq. (27) as

$$\varphi(x_1, x_2) = (x_1 + u_1(x_1, x_2) - x_3u_{3,1}(x_1, x_2))\,\mathbf{E}_1 + (x_2 + u_2(x_1, x_2) - x_3u_{3,2}(x_1, x_2)\,\mathbf{E}_2) + u_3(x_1, x_2)\,\mathbf{E}_3,$$

we get

$$\begin{cases} \mathbf{g}_1 = \varphi_{,1} = (1 + \mathrm{u}_{1,1} - \mathrm{x}_3\mathrm{u}_{3,11})\,\mathbf{E}_1 + (\mathrm{u}_{2,1} - \mathrm{x}_3\mathrm{u}_{3,12})\,\mathbf{E}_2 + \mathrm{u}_{3,1}\,\mathbf{E}_3, \\ \mathbf{g}_2 = \varphi_{,2} = (u_{1,2} - x_3u_{3,12})\,\mathbf{E}_1 + (1 + u_{2,2} - x_3u_{3,22})\,\mathbf{E}_2 + u_{3,2}\,\mathbf{E}_3, \end{cases}$$

from where the membrane strain components given by Eq. (19) follow as

$$\begin{aligned} \varepsilon_{11} &= \frac{1}{2}\big((1 + u_{1,1} - x_3u_{3,11})^2 + (u_{2,1} - x_3u_{3,12})^2 + u_{3,1}^2 - 1\big), \\ \varepsilon_{12} &= \frac{1}{2}((1 + u_{1,1} - x_3u_{3,11})(u_{1,2} - x_3u_{3,12}) + (u_{2,1} - x_3u_{3,12})(1 + u_{2,2} - x_3u_{3,22}) + u_{3,1}u_{3,2}), \\ \varepsilon_{22} &= \frac{1}{2}\big((u_{1,2} - x_3u_{3,12})^2 + (1 + u_{2,2} - x_3u_{3,22})^2 + u_{3,2}^2 - 1\big). \end{aligned} \tag{28}$$

Neglecting quadratic terms involving in-plane displacement derivatives, namely, terms of the form $u_{1,\alpha}^2, u_{2,\alpha}^2, u_{1,\alpha}u_{2,\beta}, u_{1,\alpha}u_{3,\beta\mu}, u_{2,\alpha}u_{3,\beta\mu}$ for $\alpha, \beta, \mu = 1, 2$, and quadratic terms involving second derivatives of the out of plane displacements, namely, terms of the form $u_{3,\alpha\mu}u_{3,\beta\mu}$, Eq. (28) reduces to

$$\varepsilon_{11} \approx u_{1,1} + \frac{1}{2}u_{3,1}^2, \quad \varepsilon_{12} \approx \frac{1}{2}(u_{1,2} + u_{2,1}) + \frac{1}{2}u_{3,1}u_{3,2}, \quad \text{and} \quad \varepsilon_{22} \approx u_{2,2} + \frac{1}{2}u_{3,2}^2, \tag{29}$$

which is the form of the membrane strain in the von Kármán model, see terms independent of x_3 in Eq. (2). The non trivial aspect of the approximations leading from Eqs. (28) to (29) is the retention of quadratic terms of the form $u_{3,\alpha}u_{3,\beta}$, which is the only source of nonlinearity in the strain-displacement relationship (Ciarlet, 1980). Evaluating the components of the bending strains $\boldsymbol{\kappa}$ in Eq. (19), while employing the approximate form $\mathbf{n} \approx -u_{3,1}\,\mathbf{E}_1 - u_{3,2}\,\mathbf{E}_2 + \mathbf{E}_3$ for the normal to the mid surface warranted by the assumptions of small displacements and rotations, and neglecting quadratic terms of the form mentioned above, we get

$$\begin{aligned} \kappa_{11} &= \varphi_{,1} \cdot \mathbf{n}_{,1} = -(1 + u_{1,1} - x_3u_{3,11})u_{3,11} - (u_{2,1} - x_3u_{3,12})u_{3,12} \approx -u_{3,11}, \\ \kappa_{12} &= \varphi_{,1} \cdot \mathbf{n}_{,2} = -(1 + u_{1,1} - x_3u_{3,11})u_{3,12} - (u_{2,1} - x_3u_{3,12})u_{3,22} \approx -u_{3,12} \\ \kappa_{22} &= \varphi_{,2} \cdot \mathbf{n}_{,2} = -(u_{1,2} - x_3u_{3,12})u_{3,11} - (1 + u_{2,2} - x_3u_{3,22})u_{3,22} \approx -u_{3,22}, \end{aligned} \tag{30}$$

which is indeed the bending strain in the von Kármán and Kirchhoff-Love models, see terms depending on x_3 in Eq. (2). Linearizing the membrane strain in Eq. (28) entirely yields

$$\varepsilon_{11} \approx u_{1,1}, \quad \varepsilon_{12} \approx \frac{1}{2}(u_{1,2} + u_{2,1}) \quad \text{and} \quad \varepsilon_{22} \approx u_{2,2},$$

which is the membrane strain in the Kirchhoff-Love model.

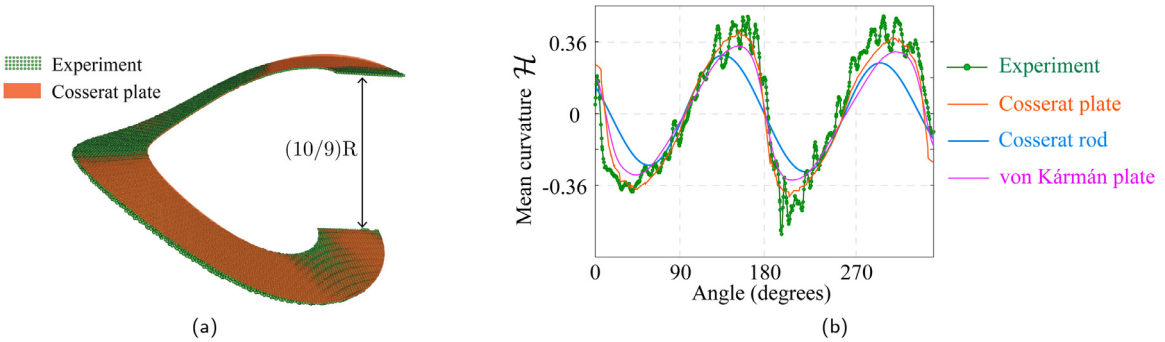

Fig. 12. Predictions of the Cosserat plate model in the transversely displaced annulus experiment. The mean curvature profile shown in (b) is computed using Eq. (34).

5.2. Experimental validation

We revisit the experiments discussed in Sections 3 and 4 to examine the performance of the Cosserat plate theory as a model for elastic ribbons. The observations in Section 5.1 show that the 1-director Cosserat plate model subsumes the two ribbon models considered previously as special cases— both the kinematics as well as the strain-displacement relationship of Cosserat plates are evident generalizations. From the outset therefore, we expect the Cosserat plate model to outperform the alternatives in comparisons with experimental measurements.

Transversely displaced annulus

Fig. 12a compares the prediction of the Cosserat plate model with the experimentally measured shape in the transversely displaced annular ribbon experiment when the separation between the edges is $\Delta_z = 100\,\text{mm}$. The model prediction in orange closely follows the measurement. This is not surprising, considering the fact that both the von Kármán and rod models predict the ribbon's deformation well in this case (see Figs. 3b and 8a).

Inspecting strain magnitudes from the simulation confirms that transverse shear strains to be negligibly small, as expected. Hence, the computed director field coincides with the unit normal $\mathbf{n}$ to the deformed mid surface. With this ansatz, we compute the mean curvature of the mid surface as

$$H(x_1, x_2) = \frac{1}{2}\frac{eG + gE - 2fF}{EG - F^2}, \tag{31}$$

where the components of the first fundamental form follow directly from the computed membrane strains as

$$\mathbf{I} = \begin{bmatrix} E & F \\ F & G \end{bmatrix} = \begin{bmatrix} \mathbf{g}_1 \cdot \mathbf{g}_1 & \mathbf{g}_1 \cdot \mathbf{g}_2 \\ . & \mathbf{g}_2 \cdot \mathbf{g}_2 \end{bmatrix} = \begin{bmatrix} 1+\varepsilon_{11} & \varepsilon_{12} \\ . & 1+\varepsilon_{22} \end{bmatrix} \Rightarrow E = 1+\varepsilon_{11}, F = \varepsilon_{12}, G = 1+\varepsilon_{22}. \tag{32}$$

Assuming $\mathbf{n} \approx \mathbf{t}$, the second fundamental form is computed using the components of the bending strain as

$$\mathbf{II} = \begin{bmatrix} e & f \\ f & g \end{bmatrix} \approx \begin{bmatrix} \mathbf{g}_1 \cdot \mathbf{t}_{,1} & \mathbf{g}_1 \cdot \mathbf{t}_{,2} \\ . & \mathbf{g}_2 \cdot \mathbf{t}_{,2} \end{bmatrix} = \begin{bmatrix} \kappa_{11} & \kappa_{12} \\ . & \kappa_{22} \end{bmatrix} \Rightarrow e = \kappa_{11}, f = \kappa_{12}, g = \kappa_{22} \tag{33}$$

Substituting Eqs. (32) and 33 in Eq. (31), we get

$$H = \frac{1}{2}\frac{\kappa_{11}(1+\varepsilon_{22}) + \kappa_{22}(1+\varepsilon_{11}) - 2\kappa_{12}\varepsilon_{12}}{(1+\varepsilon_{11})(1+\varepsilon_{22}) - \varepsilon_{12}^2}. \tag{34}$$

Fig. 12b shows the profile of the mean curvature computed along the centerline of the ribbon using Eq. (34). While all three models indicated in the figure follow the experimental profile well, the prediction of the Cosserat plate appears to be the closest match. Both in this experiment, as well as in the case of the pinched semi- annulus discussed next, simulations show membrane strains to be negligibly small. As a result, H computed using Eq. (34) is well approximated by half of the trace of the bending strain $(\kappa_{11} + \kappa_{22})/2$. We do not employ this approximation in our calculations, however.

Pinched semi annulus

Fig. 13a compares predictions of the Cosserat plate model with measured shapes for the pinched semi annular ribbon experiment. The predictions closely follow the measurements at all separation distances shown. Fig. 13b examines the displacement components at the mid point along the centerline of the ribbon, and shows that the prediction of the Cosserat plate model adheres closely to the experimental measurements over a large range of edge separations. In fact, the lower bound of 20 mm for Δ_y in the plot is the limiting separation at which the two edges of the ribbon abut each other. The prediction of the Cosserat rod model is far less accurate for the component u_1. To help visualize the displacement errors

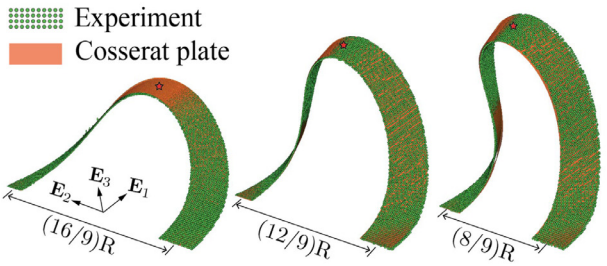

(a) Comparison of measured and predicted ribbon shapes.

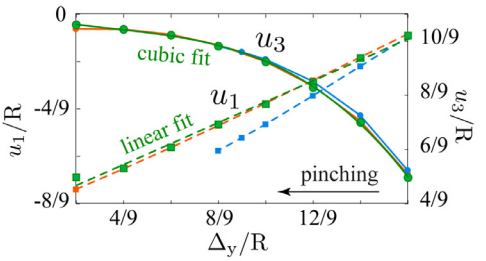

(b) Measured and predicted displacement at the mid-point along the centerline of the ribbon.

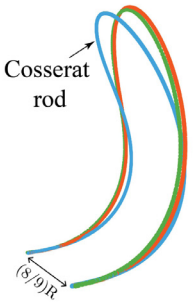

(c) Measured and predicted centerlines at $\Delta_y = 80\,\mathrm{mm}$.

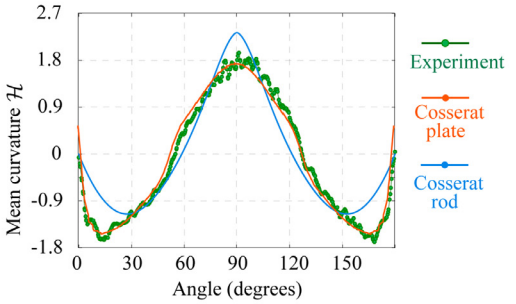

(d) Comparison of mean curvatures along the centerline.

Fig. 13. Examining predictions of the Cosserat plate model in the pinched semi annulus experiment.

seen in the plot, Fig. 13c shows the centerlines of the ribbon from the experiment and from simulations at $\Delta_y = 80\,\mathrm{mm}$. Fig. 13d compares mean curvatures along the centerline computed from simulations and from experimental measurements. The plate model outperforms the rod model here as well.

Unfurled annulus

Fig. 14 examines the predictions of the Cosserat plate model in the unfurled annulus experiment. We include predictions of the rod model previously shown in Figs. 9b and c to help compare its accuracy with the Cosserat plate model. Fig. 14a shows that the ribbon shapes computed using the plate model follow the measured shapes well.

The plots in Fig. 14b show that the mean curvature along the centerline computed by the plate model captures all details found from the experimental data, including zero crossings and extrema. The model correctly shows that the ribbon prefers to alternate between mean curvatures of opposite signs with approximately equal magnitude, and that the frequency of alternation increases with the separation Δ_y. The rod model, on the otherhand, incorrectly predicts localized curvatures at the clamps and at the center, and a nearly constant but small curvature elsewhere. Fig. 15a shows that the centerline predicted at a large separation of $\Delta_y = 470\,\mathrm{mm}$ by the rod model has the appearance of a helix, with a change in chirality at the mid point and sharp bends at the clamped ends. Both the experiment and the Cosserat plate model predict qualitatively different shapes.

6. Observations on the shape of a pinched semi annulus

With the objective of aiding a deeper analysis of the problem, we record a few observations on the shapes of ribbon centerlines in the pinched semi annulus experiment. Specifically, we identify plausible relationships between the mean radius R, the imposed displacement and the mean curvature $\mathcal{H}$ along the centerline of a pinched semi annular ribbon using simulations of the Cosserat plate model. Relying on numerical simulations helps to avoid the large number of physical measurements that would be required for the ensuing discussions, as well as to evade ambiguities stemming from noise and data fitting procedures. Furthermore, for each combination of ribbon radius and width, experimental measurements require identifying displacement regimes over which the influence of gravity is sufficiently small, cf. Plaut and Virgin (2004). Gravity effects are unambiguously eliminated in numerical simulations. Indeed, the close agreement between mean curvature profiles computed from shape measurements and from simulations over a broad range of displacements shown in Fig. 16, albeit for the specific case of a ribbon with dimensions $\mathrm{R} = 90\,\mathrm{mm}$ and $w = 20\,\mathrm{mm}$, warrants considering model simulations as convenient *virtual experiments*.

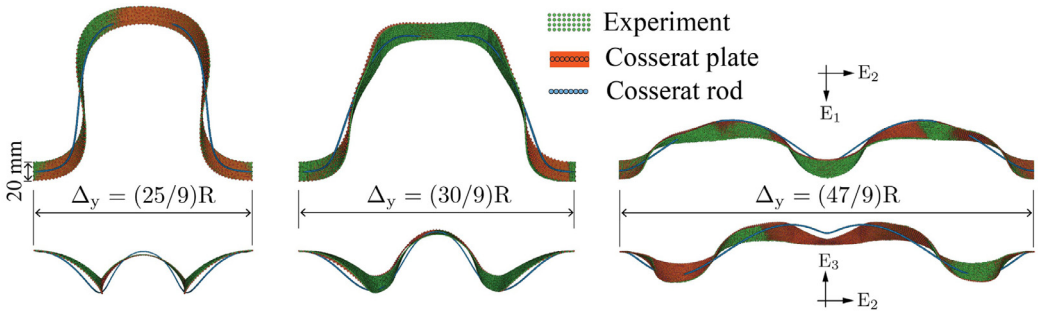

(a) Comparison of predicted and measured ribbon shapes for three different separation distances. Only the centerline of the ribbon is shown for the rod model.

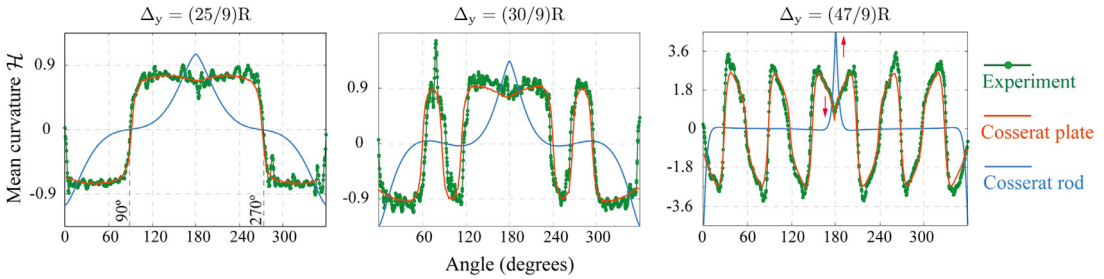

(b) Mean curvature profiles along the centerline of the ribbon.

Fig. 14. Examining the predictive accuracy of the Cosserat plate model in the unfurled annulus experiment.

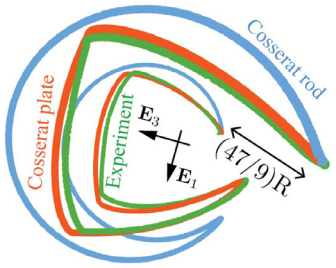

(a) Predicted and measured centerlines at $\Delta_y = 470$ mm.

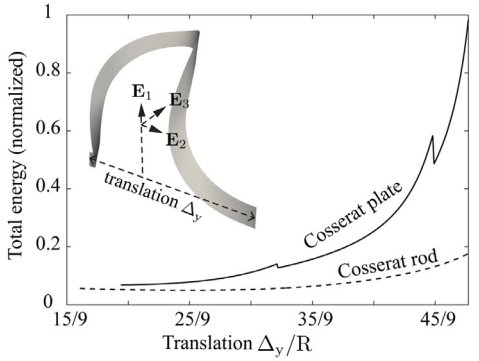

(b) Energies of solutions predicted by the Cosserat rod and plate models.

Fig. 15. Evaluating accuracies of predicted ribbon centerlines in the unfurled annulus experiment. The image in (a) reveals qualitative errors in the shape predicted by the Cosserat rod model. Plot (b) shows that the rod model predicts a lower energy than the plate model despite identifying an inaccurate solution. This suggests that the kinematic assumptions invoked in the rod model ignores important energetic contributions. Jumps in the energy observed in the plate model are related to transitions between solution branches discussed in Section 7.

In the following, we non dimensionalize the imposed displacement as $\delta = (2\mathrm{R} - \Delta_y)/\mathrm{R}$, where the control parameter Δ_y denotes the separation between the ends of the ribbon. In the unloaded state therefore, $\Delta_y = 2\mathrm{R}$ and $\delta = 0$. The maximum displacement is limited to $\delta = (2 - w/\mathrm{R})$, when the two displaced ends of the ribbon contact each other at the center.

(i) For semi annular ribbons having width $w = 20$ mm, Fig. 17 plots the non dimensionalized mean curvature $\mathcal{H}_{\mathrm{mid}}$ at the mid point of the centerline as a function of the non dimensionalized displacement δ. We find that over a reasonably large range of mean radii, the relationship between δ and $\mathcal{H}_{\mathrm{mid}}$ is approximately independent of R, leading us to conclude that $\mathcal{H}_{\mathrm{mid}} = \mathcal{H}_{\mathrm{mid}}(\delta)$, i.e., that $\mathcal{H}_{\mathrm{mid}}$ depends on R only through δ. The specific values of the mean radii chosen in the plot, ranging from 70 to 120 mm, are not limiting values but simply represent ones for which simulations were performed.

(ii) The nature of the relationship $\delta \mapsto \mathcal{H}_{\mathrm{mid}}(\delta)$ in Fig. 17 is noticeably different for small and large values of δ, i.e., close to the bifurcation from the planar state, and far away from it. An inspection reveals that for δ less than about 0.3,

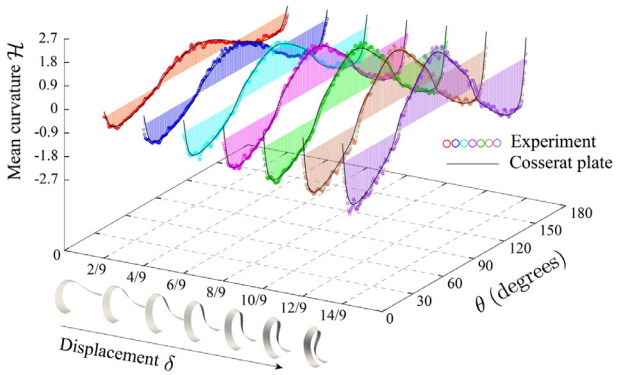

Fig. 16. Comparison of non dimensionalized mean curvature profiles computed from shape measurements, and from Cosserat plate simulations for the pinched semi annulus experiment ($R = 90\,mm, w = 20\,mm$) over a broad range of displacements $\delta = (2R - \Delta_y)/R$.

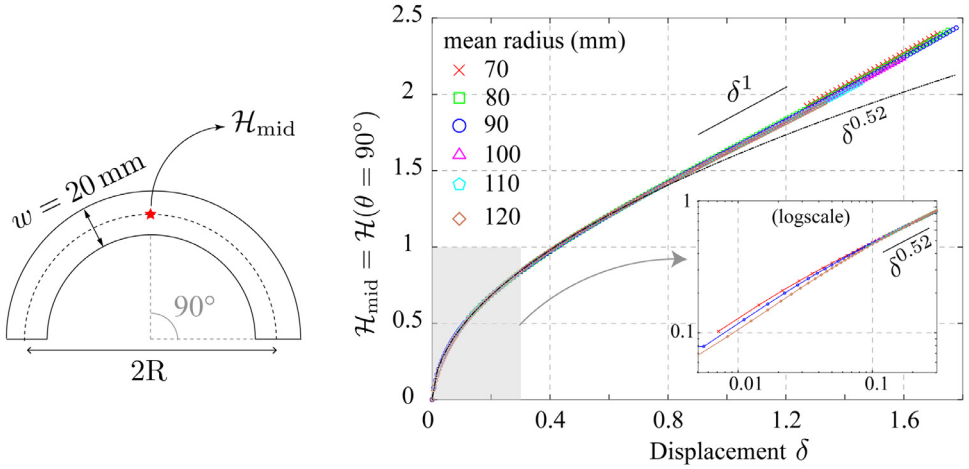

Fig. 17. For ribbons of varying mean radii but fixed width, the plot shows the dependence of the mean curvature at the mid point of the centerline ($\mathcal{H}_{mid}$) on the imposed displacement (δ).

$\mathcal{H}_{mid}(\delta)$ varies approximately as $\sqrt{\delta}$. The inset in the plot identifies the exponent of δ to 0.52 based on an exponential fit over points having $0.1 \le \delta \le 0.3$. For δ larger than about 0.5, $\delta \mapsto \mathcal{H}_{mid}(\delta)$ is approximately linear. Coincidentally, the transition from nonlinear to linear dependence of $\mathcal{H}_{mid}$ on δ occurs in the vicinity of $\mathcal{H}_{mid} = 1$, i.e., where the mean curvature falls below 1/R.

(iii) Next, we examine whether the nature of the relationship $\delta \mapsto \mathcal{H}_{mid}(\delta)$ observed in Fig. 17 extends to mean curvature profiles along the entire centerline, i.e., to $0 \le \theta \le 180°$. To this end, Fig. 18a shows profiles of $\mathcal{H}$ as a function of θ for a representative set of displacements $\delta = 0.1, 0.2, 0.3$ and 0.4 computed for the set of ribbons considered in Fig. 17. Consistent with our previous observation in (i), we find that for each δ, the profile of $\mathcal{H}$ is largely independent of R. This suggests that $\mathcal{H} = \mathcal{H}(\theta, \delta)$, i.e., that $\mathcal{H}$ depends on R only through δ. In light of the scaling $\mathcal{H}_{mid} \sim \delta^{0.52}$ observed in Fig. 17 for small δ, Fig. 18b plots the scaled mean curvature $\mathcal{H}/\delta^{0.52}$, which, to a good degree of approximation, appears to be independent of δ. Hence, for sufficiently small δ, the mean curvature along the centerline is well approximated by a variable-separable functional form $\mathcal{H}(\theta, \delta) \approx f(\theta)\,\delta^{0.52}$.

(iv) Fig. 19a shows profiles of $\mathcal{H}$ along the centerline for larger δ ranging from 0.6 to 1.4, which, again, appear to be independent of R. Hence, we assume that $\mathcal{H} = \mathcal{H}(\theta, \delta)$ in this regime as well. Fig. 17 then suggests postulating a linear dependence for $\mathcal{H}(\theta, \delta)$ on δ. Towards verifying this possibility, we compute

$$\mathrm{F}(\theta, \delta) = \frac{\partial \mathcal{H}}{\partial \delta}(\theta, \delta) \approx \frac{\mathcal{H}(\theta, \delta + 1/\mathrm{R}) - \mathcal{H}(\theta, \delta)}{(1/\mathrm{R})} \tag{35a}$$

$$\text{and} \quad \mathrm{G}(\theta, \delta) = \mathcal{H}(\theta, \delta) - \mathrm{F}(\theta, \delta). \tag{35b}$$

The calculation in Eq. (35a) is a finite difference approximation of $\partial\mathcal{H}/\partial\delta$ computed using finite element simulations performed with 1 mm displacement increments. Fig. 19b shows the profiles of F and G computed according to Eq. (35) for a large range of displacements in the regime $\delta \ge 0.75$, and for mean radii ranging from 70 to 120 mm.

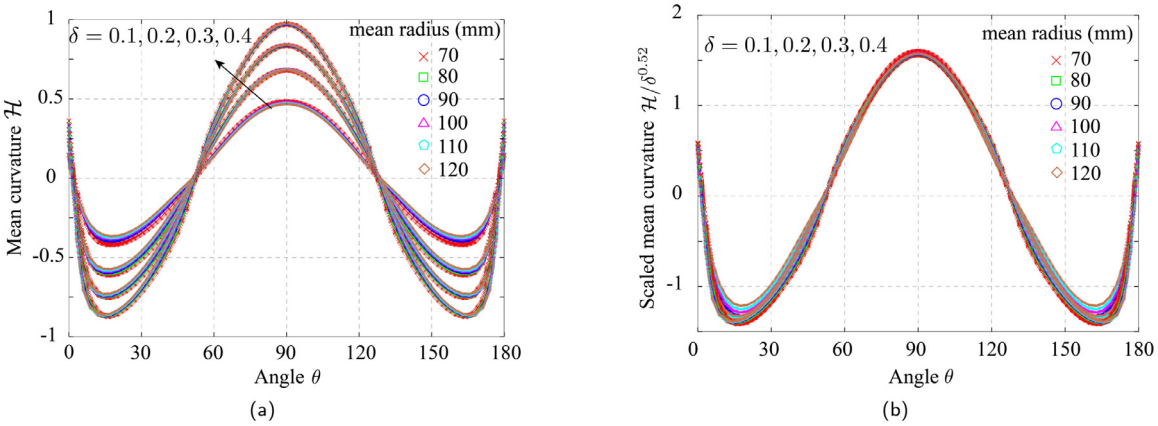

Fig. 18. Examining the dependence of $\mathcal{H}$ on δ for sufficiently small values δ. Plot (a) shows that $\mathcal{H}$ depends on R only through δ. Then, profiles of the scaled mean curvature plotted in (b) suggests the approximate functional form $\mathcal{H}(\theta,\delta) \approx f(\theta)\delta^{0.52}$ for the mean curvature along the centerline.

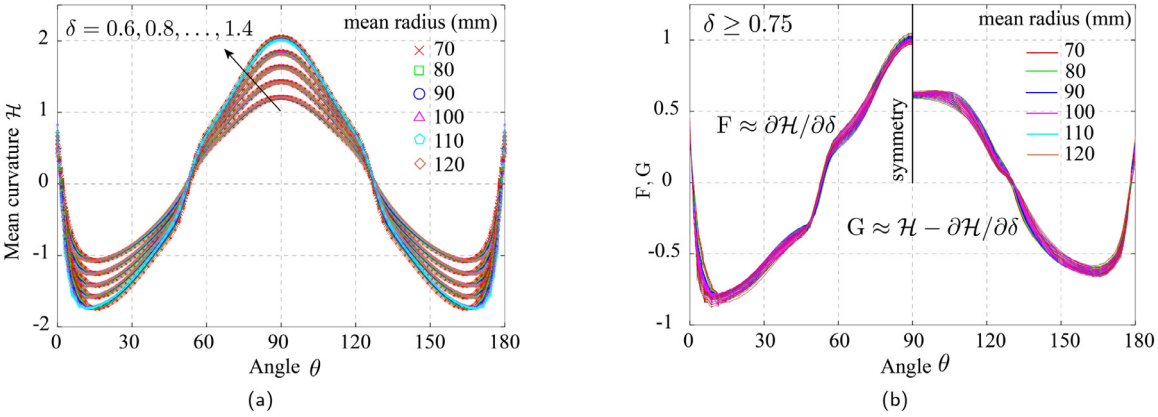

Fig. 19. Plot (a) shows profiles of $\mathcal{H}$ along the centerline for representative values of displacements in the regime $\delta \geq 0.6$. The profiles remain unchanged with radius, leading to the conclusion that $\mathcal{H}$ depends on R only through δ. Then, the near independence of $\mathrm{F} = \partial\mathcal{H}/\partial\delta$ and $\mathrm{G} = \mathcal{H} - \mathrm{F}$ on δ seen in (b) suggests the functional form $\mathcal{H}(\theta,\delta) \approx \mathrm{F}(\theta)\delta + \mathrm{G}(\theta)$, for sufficiently large δ.

Noting the symmetry of $\mathcal{H}$, and consequently of F and G about $\theta = 90^\circ$, Fig. 19b shows profiles of F, G over complementary halves of the centerline. To a good degree of approximation, both F and G are independent of δ, thus supporting the ansatz $\mathcal{H}(\theta,\delta) \approx \mathrm{F}(\theta)\delta + \mathrm{G}(\theta)$ in the regime where δ is sufficiently large.

(v) The functional forms for $\mathcal{H}$ identified in (iii) and (iv) for small and large δ respectively, are consistent with the observations in Figs. 18a and 19a that the locations of zero crossings in the mean curvature profiles remain unchanged with δ. Similarly, both relationships ensure monotonic growth in mean curvature magnitudes with the imposed displacement.

(vi) It is worth noting that the qualitative difference in the relationship $\delta \mapsto \mathcal{H}_{\mathrm{mid}}(\delta)$ for small and large δ observed in Fig. 17, also manifests in the shapes of the profiles seen in Figs. 18a and 19 a.

(vii) Conspicuously missing in our discussions thus far, are considerations on the influence of the width of the ribbon. We expect w, and in particular the aspect ratio w/R, to be a significant parameter in determining ribbon shapes during deformation. Notice that by fixing w (at 20 mm) and changing R, the aspect ratio w/R is not held constant in the data presented in Figs. 17–19. As we discuss next, ignoring the influence of w/R in postulating the relationships above is not an oversight, but an approximation. Fig. 20 a examines the dependence of $\mathcal{H}_{\mathrm{mid}}$ on δ for ribbons having identical mean radius but different widths. For definiteness, we choose R = 90 mm and let the width range from 2.5 to 40 mm. While unambiguously confirming the influence of w/R on the deformation, the plot also shows that $\mathcal{H}_{\mathrm{mid}}$ is increasingly insensitive to w/R at sufficiently large values of the parameter, notably beyond the ratio $w/\mathrm{R} = 15/90 = 1/6$. Fig. 20b confirms that this insensitivity of $\mathcal{H}$ to w/R is not restricted to the mid point of the centerline, but extends to the profile of $\mathcal{H}$ along the entire centerline. The choice of the mean radius R = 90 mm in Fig. 20 is not especially significant— we have verified these conclusions for ribbons having mean radii ranging from 70 to 120 mm.

In summary, simulations of the pinched semi annulus experiment using the Cosserat plate model helps identify approximate relationships between the displacement and the mean curvature distribution along centerlines of ribbons with

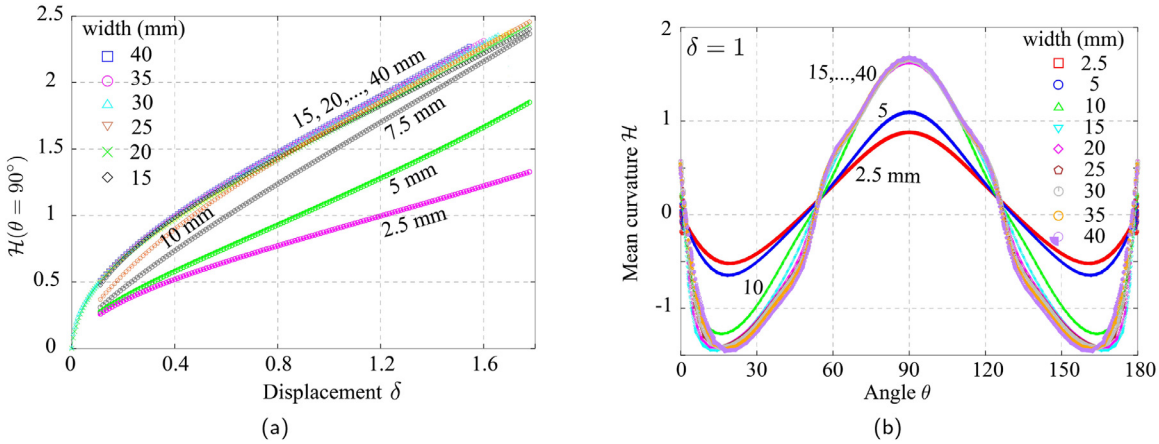

Fig. 20. Examining the influence of the aspect ratio w/R on the mean curvature along the centerline by fixing the mean radius at 90 mm and varying the width from 2.5 to 40 mm. The plots show that $\mathcal{H}$ is approximately insensitive to w/R at sufficiently large values of the parameter..

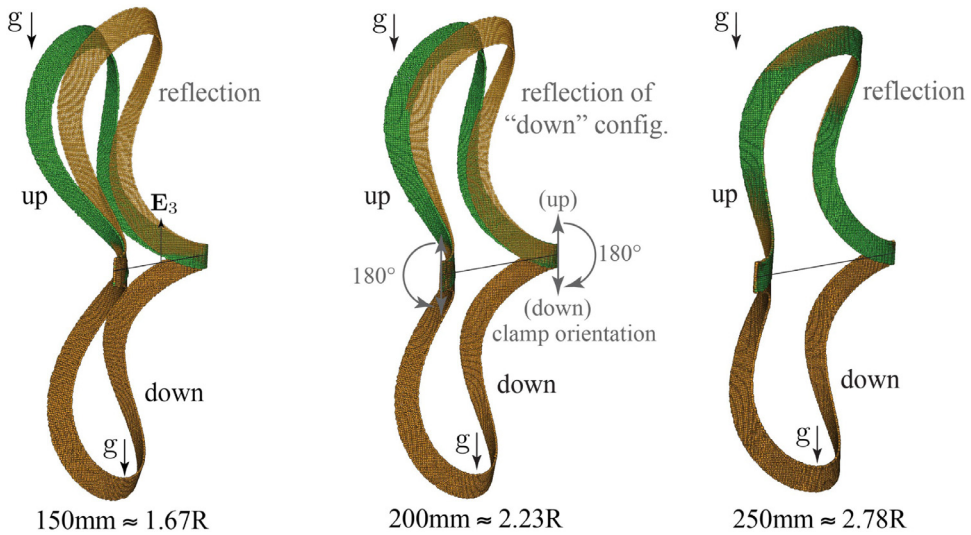

Fig. 21. Illustration of the procedure to identify deformations in which the effect of self weight is small in the unfurled annulus experiment. Rotating the clamps holding the ribbon edges by 180° as shown, helps compare a configuration in which the gravitational force acts towards the line joining the centers of the clamps, with another in which the force acts away from it. These configurations are labelled as "up" and "down," respectively. We deem the effect of gravity to be small if the ribbon has nearly identical shapes in the two configurations. We follow an identical procedure for the pinched semi annulus experiment as well.

sufficiently large aspect ratios w/R. Although the parametric studies shown here are not a substitute for a rigorous analysis, we expect the observations pointed out to serve as useful hints in modeling the problem.

7. Observations from unfurling an annular ribbon

We devote this section to discussing a few observations from the unfurled annulus experiment and its simulation using the Cosserat plate model. A short video illustrating these findings is provided as supplementary material.

(i) We mentioned in Section 2 that for the purpose of comparing experimental measurements with simulations that do not include the effect of self weight, it is necessary to identify displacement regimes over which the influence of gravity is measurably small. In the context of the unfurled annulus experiment, we expect to find such a regime for two reasons. First, the ribbon (geometrically) stiffens with increasing separation between the clamps, causing the deformation induced by self weight to become progressively smaller. Second, the out-of-plane component of the displacement decreases with increasing Δ_y. Consequently, the twisting moment of the gravitational force about the $\mathbf{E}_2$ axis reduces with increasing Δ_y. Fig. 21 illustrates the procedure we adopt to identify ribbon configurations that are insensitive to gravity effects. We rely on the fact that if the influence of gravity is negligible, then the deformation of the ribbon should be symmetric about the (horizontal) plane spanned by the $\mathbf{E}_1 - \mathbf{E}_2$ axes. Hence, we measure

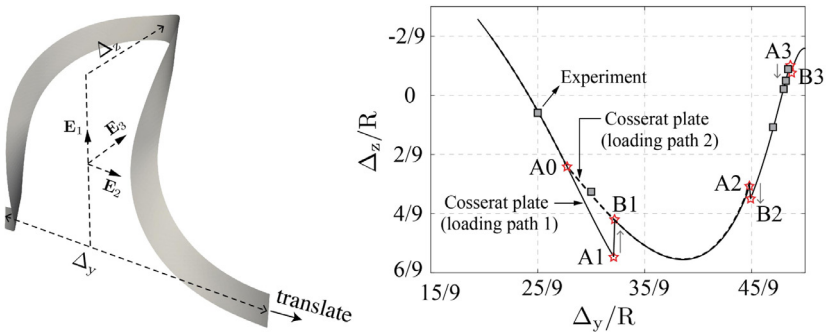

(a) Jumps in the out-of-plane displacement at the midpoint along the centerline of the ribbon found from simulations are accompanied by a transition in the number of zero crossings in the mean curvature.

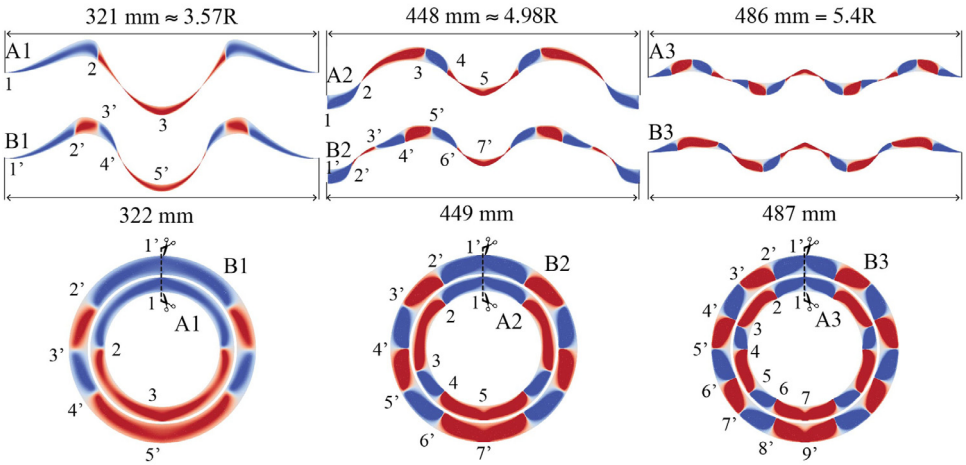

(b) Contours of mean curvature over the deformed and reference configurations at transition states along loading path 1 indicated in (a). Blue and red colors correspond to negative and positive values, respectively. Corresponding landmarks in the reference and deformed configurations are provided to aid in visualization.

Fig. 22. Number of zero crossings in the mean curvature increases abruptly with loading in the unfurled ribbon experiment. These transitions often manifest as displacement jumps during simulations.

two sets of deformations in which the orientations of the clamped ribbon edges differ by 180°. These configurations are labelled as "up" and "down" in the figure and depicted in green and brown colors, respectively. Notice that the gravitational force acts towards the line joining the centers of the clamps in the former, and away from it in the latter. By (digitally) reflecting measured ribbon shapes about the horizontal plane, we compare the deformations in the two configurations. At $\Delta_y = 150$ and 200 mm, the shapes measured in the "up" and "down" configurations are noticeably different, clearly demonstrating that the effect of self-weight is significant at these displacements. At the larger distance $\Delta_y = 250$ mm where the two configurations practically overlap, we deem the effect of gravity to be small.

(ii) In Fig. 14b, notice that the number of zero crossings in the mean curvature changes with loading. At $\Delta_y =$ 250 mm, 300 mm and 470 mm, the experimental data shows 2, 6 and 10 zero crossings, respectively. The transition between ribbon configurations having different number of such "inflection" points often happens abruptly in our Cosserat plate simulations. To illustrate this point, Fig. 22a shows the evolution of the out-of-plane component of the displacement at the midpoint of the centerline of the ribbon. In the simulation labeled as loading path 1, the displacement jumps from state A1 to B1 at $\Delta_y = 321$ mm. Similar jumps occur from A2 to B2, and A3 to B3 at distances 448 mm and 486 mm, respectively. Contours of the mean curvature shown in Fig. 22b confirm that the transitions seen in Fig. 22a correspond to changes in the number of zero crossings in the mean curvature. For ease of visualization, we show contours over both the reference and deformed configurations. Blue contours correspond to negative values and red ones to positive values of mean curvature. In Fig. 22b, we see that the mean curvature in state A1 has two zero crossings. A small increase in Δ_y causes the ribbon to jump to state B1 having six zero crossings, which

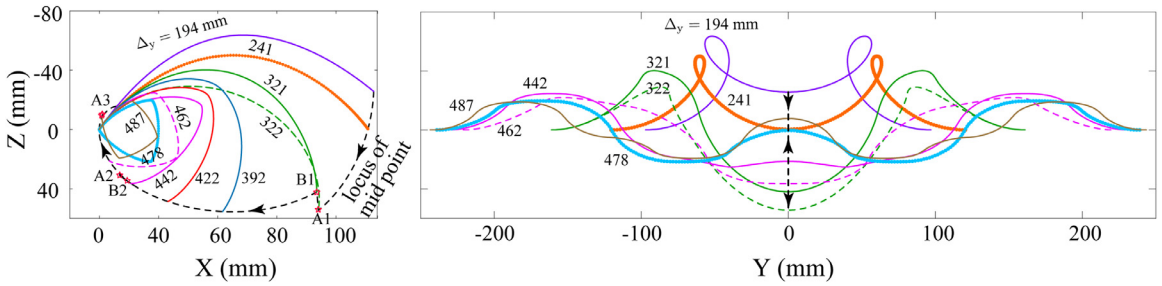

Fig. 23. Projections of centerline shapes predicted by the Cosserat plate model on the $\mathbf{E}_1 - \mathbf{E}_3$ and $\mathbf{E}_2 - \mathbf{E}_3$ planes. Apparent kinks in the profile in the former correlate well with transitions in the number of zero crossings in the mean curvature of the ribbon. The plots also reveal extensive twist in the ribbon to accommodate the imposed displacement.

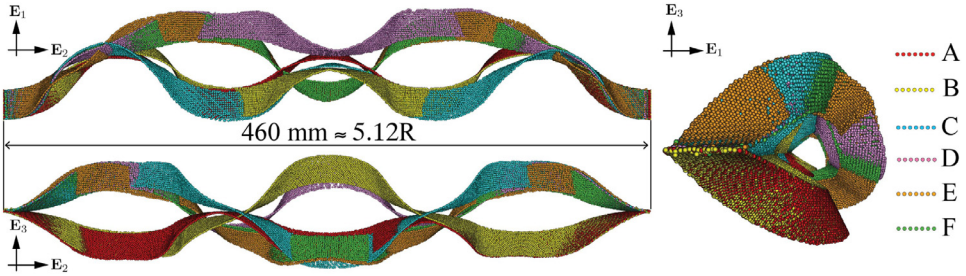

Fig. 24. Experimental demonstration of multiple stable equilibria in the unfurled annulus experiment.

persists until the ribbon reaches state A2 at $\Delta_y = 448$ mm. The ribbon then transitions to state B2 having 10 zero crossings. In the same manner, at $\Delta_y = 486$ mm, the ribbon transitions from state A3 having 10 zero crossings to state B3 having 14 zero crossings. Each of these three transitions is accompanied by a decrease in the total strain energy of the ribbon, see Fig. 15b. In particular, the strain energy at state B1 is smaller than at A1, at state B2 is smaller than at A2, and so on.

(iii) Fig. 22a also shows an alternative loading path in dashed lines, labeled as path 2. The simulations shown in Fig. 14 in fact correspond to loading path 2. The transition from two to six zero crossings in path 2 occurs at the point A0 ($\Delta_y \approx 277$ mm) where paths 1 and 2 diverge. Unlike loading path 1, the transition at A0 in path 2 occurs without a noticeable jump in the displacement. Inspecting the number of zero crossings in the mean curvature on either side of A0 suggests that paths 1 and 2 are solution branches that bifurcate at A0. Without special techniques to detect bifurcations or instabilities in our simulations/experiments, it is unfortunately not possible to examine the real nature of transitions in the mean curvature, i.e., whether they occur smoothly or through an instability.

(iv) Fig. 23 shows projections of the ribbon's centerline on the $\mathbf{E}_1 - \mathbf{E}_3$ and $\mathbf{E}_2 - \mathbf{E}_3$ planes computed using the Cosserat plate model. Appearance of apparent kinks in the projection on the $\mathbf{E}_1 - \mathbf{E}_3$ plane correlate well with transitions in the number of zero crossings in the mean curvature— the first kink develops after the transition from two to six zero crossings ($\Delta_y > 322$ mm), the second after the transition from six to ten zero crossings ($\Delta_y > 449$ mm), and so on.

(v) The spiral-like trajectory of the mid point of the centerline in the $\mathbf{E}_1 - \mathbf{E}_3$ plane and the progressive narrowing of the profile along the $\mathbf{E}_1$ and $\mathbf{E}_3$ axes observed in Fig. 23 show that the ribbon accommodates increasing amount of the imposed stretch Δ_y by twisting about the $\mathbf{E}_2$ axis. The extent of twist is exemplified in the figure by the observation that the out-of-plane displacement (along $\mathbf{E}_3$) of the mid point changes sign twice over the range of Δ_y considered, namely, at $\Delta_y \approx 241$ mm and 478 mm. In fact, the mid point completes a full revolution about the $\mathbf{E}_2$ axis as Δ_y is increased from 241 to 478 mm.

(vi) The appearance of two, six, ten and fourteen zero crossings in the mean curvature can be rationalized as follows. Let us assume that transitions in the mean curvature are accompanied by reasonably small perturbations in the deformation itself. In particular, let us assume that the sign of the mean curvature at the clamps and at the center of the ribbon remain unchanged after each transition. Fig. 22 suggests that this is indeed the case— the mean curvature remains negative (blue) at the clamps and positive (red) at the center before and after each transition. In fact, these signs remain unchanged throughout the deformation. Then, symmetry of the deformation about the $\mathbf{E}_1 - \mathbf{E}_3$ plane requires that the mean curvature possess an odd number of zero transitions, say of the form $2k+1$ for $k = 0, 1, 2, \ldots$, on either side of the symmetry plane. Hence, the total number of zero transitions is of the form $2(2k+1)$ for $k = 0, 1, 2, \ldots$. Then, the number of transitions observed in Figs. 14b and 22, namely, two, six, ten and fourteen, correspond to setting $k = 0, 1, 2$ and 3, respectively.

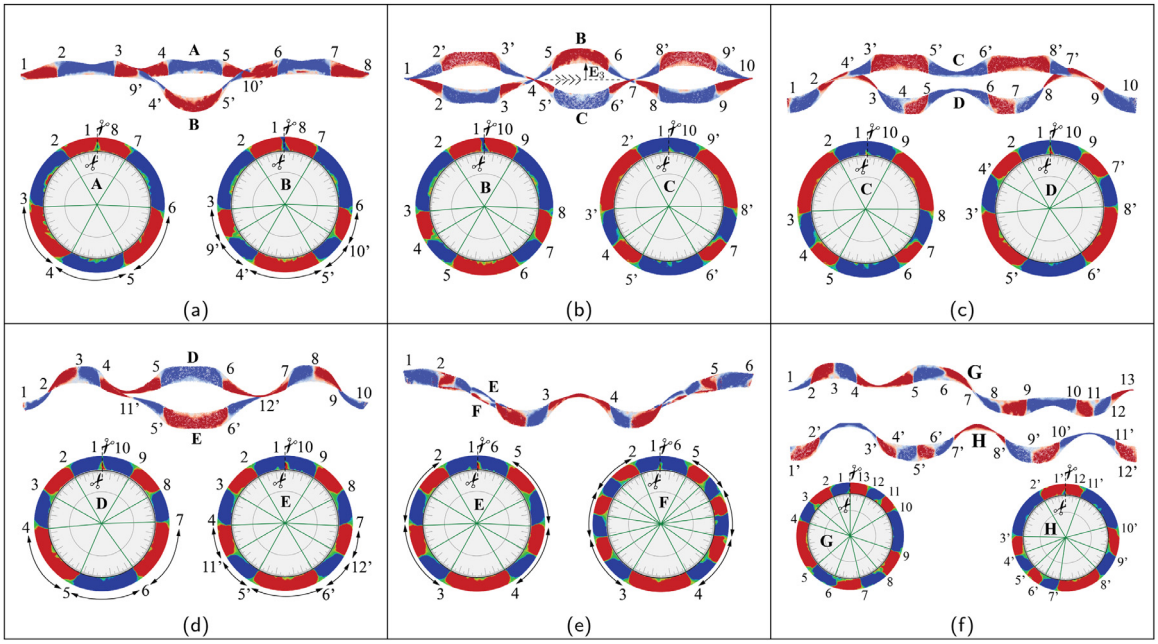

Fig. 25. Pairwise comparisons of mean curvature distributions in the six measured stable configurations of the ribbon shown in Fig. 24. These contours suggest that mean curvatures may help to encode different solution branches and reveal how to transition from one branch to another, see item (viii) in the text.

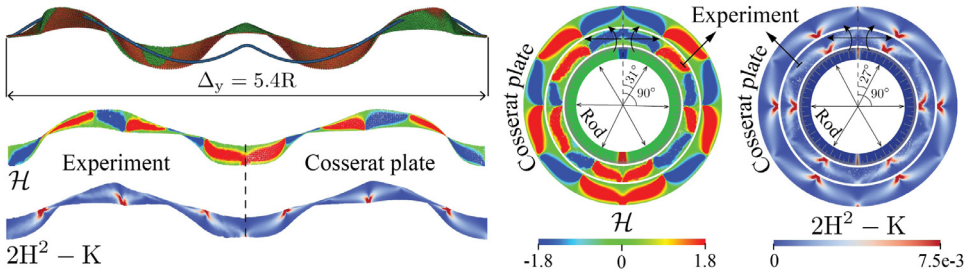

Fig. 26. At large separation between the edges, the ribbon accommodates a state of high tension by focusing energy at vertices along the inner circumference. Large values of $W = 2H^2 - K$ at these vertices reveal non trivial Gaussian curvatures there, and in turn, local extension of the material.

(vii) While Fig. 22a hints at the possibility of multiple equilibrium solutions, Fig. 24 provides compelling experimental evidence. For ease of visualization, Fig. 24 shows six among many more distinct configurations measured experimentally. The configurations shown are labeled as states A through F and are depicted in different colors. The specific value of the edge separation $\Delta_y = 460$ mm used for the demonstration is not particularly significant— we find multiple equilibria at smaller as well as at larger distances. We realize the different states shown by manually adjusting the ribbon without altering the boundary conditions, and verify the stability of each state by subjecting the ribbon to small perturbations. Presumably, each of these states correspond to a different stable solution branch. The multiplicity of solutions observed serves as a reminder of the importance of geometric nonlinearity in ribbon mechanics.

(viii) To compare features of the different configurations seen in Fig. 24, and in turn, of solution branches they belong to, we examine their mean curvature distributions in Fig. 25. For ease of visualization, we show contours over both reference and deformed configurations for each state and label corresponding landmark points. In the following, we examine the six states A through F in a pairwise manner and discuss how transformations between them are achieved.

(a) Plot Fig. 25a compares state A having six zero crossings in the mean curvature, with state B having eight. The transition from A to B is achieved by altering the region of the ribbon demarcated by the zero crossings at points 3 and 6 in state A. The central lobe of the ribbon is inverted to flip the sign of the curvature there, and two new zero crossings at $9'$ and $10'$ are introduced on either side of the $\mathbf{E}_1 - \mathbf{E}_3$ symmetry plane. States A and B agree in shape between the clamps and the landmarks 3 and 6 respectively, but differ elsewhere.

(b) By virtue of the boundary conditions imposed in the experiment, solutions enjoy reflection symmetry about the $\mathbf{E}_1 - \mathbf{E}_2$ plane. An example of this symmetry is provided in plot (b), which shows that states B and C are simply mirror images of each other about the $\mathbf{E}_1 - \mathbf{E}_2$ plane. A consequence of this reflection symmetry is that curvatures

in the two states are equal in magnitude but opposite in sign. Hence, colors of curvature contours in B and C are complementary to each other.

(c) An alternative mode of modifying mean curvatures without altering the number of zero crossings is shown in plot (c). Therein, the transformation from state C to D is achieved by shifting zero crossings 4 and 7 in C to 4′ and 7′ in D.

(d) The transformation from state D to E in plot (d) mimics that shown in (a). We invert the curvature at the center of the ribbon between points 4 and 7 in state D, and introduce new new zero crossings 11′ and 12′. State E with ten zero crossings in fact belongs to the solution branch B2-A3 in Fig. 22a.

(e) Plot (e) shows the transformation from state E to F is achieved in a manner similar to that in (a) and (d). This time, however, we introduce two new zero crossings on either side of the $\mathbf{E}_1 - \mathbf{E}_2$ symmetry plane, so that the sign of the mean curvature at the center remains unchanged. The number of zero crossings hence jumps from ten in E to fourteen in F. Recall that we observe a similar transition in Fig. 22a, albeit at a larger separation $\Delta_y = 486\,\text{mm}$. It is likely therefore, that state F belongs to the solution branch containing B3 in Fig. 22a.

(f) While states A through F all enjoy reflection symmetry about the $\mathbf{E}_1 - \mathbf{E}_3$ plane, plot (f) shows configurations G and H violating this symmetry. In state G, one of the zero crossings in the mean curvature occurs approximately at the center of the ribbon at the landmark point 7, and curvatures at the two clamps have opposite signs. The ribbon has different number of zero crossings on either side of the $\mathbf{E}_1 - \mathbf{E}_3$ plane in state H, namely, six on the left side (2′ through 7′) and four on the right side (8′ through 11′).

In summary, Figs. 23 and 24 show representative configurations sampling what appears to be a complex landscape of multiple stable solution branches. The discussion above suggests that the signature of mean curvature distributions over the reference configuration, i.e., the number and angular extents of positive and negative values, can serve as a convenient way of *encoding* different solution branches. These signatures, in a rough sense, capture the microstructure of the deformation, while also providing useful information about the perturbations necessary to transition from one branch to another.

(ix) The last observation we note concerns energy focusing at large edge separations. Although we have not measured the forces required, hand held trials suggest that the tension in the ribbon increases steeply as Δ_y becomes comparable to the perimeter of the inner circumference ($2\pi R_i \approx 502.7\,\text{mm}$). At these large tensions, extensibility of the ribbon becomes important, and is likely to influence its deformation. As is often observed in slender structures, we expect energetic considerations to dictate the ribbon to adopt a configuration with localized extension when subject to a large tension.

Fig. 26 shows one such instance, with the end separation set to $\Delta_y = 484\,\text{mm}$. Reiterating our previous observations, we find here too that the prediction of the Cosserat plate model closely follows the measured shape while the centerline of the rod solution shows large deviations. The ribbon configuration shown has ten zero crossings in the mean curvature and belongs to the solution branch B2-A3 in Fig. 22a. More pertinent to our point on energy focusing, the Cosserat plate simulation for this large Δ_y reveals that the membrane component of the strain energy is comparable to the bending component. To examine the significance of extensibility in the deformation, we show contours of $W = 2H^2 - K$ in the figure, where K is the Gaussian curvature. We pick W, which is simply half of the sum of squared principal curvatures, in favor of alternate energy densities because it is computable both from predicted and measured ribbon shapes, besides being independent of material parameters. Both the experiment and the simulated solution show sharp localization of W at vertices along the inner circumference of the ribbon where positive and negative contours of the mean curvature meet. The deformation observed in the experiment is fully reversible and these vertices are not the result of any localized damage. Instead, steep gradients in the mean curvature at these vertices induce non trivial Gaussian curvatures, which indirectly conveys local extension of the material.

8. Summary and concluding remarks

Summary. Table 1 succinctly summarizes our findings based on comparing model predictions with measured shapes of ribbons and curvatures computed from them. The inadequacy of linear plate theories is not surprising, considering the expected geometric nonlinearities in ribbon deformations. Fig. 4b amply illustrates this point— the measured out of plane displacement at the midpoint of the ribbon in the pinched semi annulus experiment varies nonlinearly (approxi-

Table 1
A summary of our investigation of models for elastic ribbons. The ✗/√symbols indicate inaccurate/accurate predictions when compared with experimental measurements.

Experiments → ↓ Models	Transversely displaced annulus	Pinched semi annulus	Unfurled annulus
Linear plates	✗		
von Kármán plates	√	✗	
Cosserat rods	√	√	✗
Cosserat plates	√	√	√

mately cubically) with progressive pinching. The same experiment also highlights pitfalls in adopting the von Kármán plate model. While large deviations between predicted and measured shapes become conspicuous with increasing loading (i.e., Δ_y) in Fig. 5a, a lack of inner consistency in the model arising from finite rotations of material directors during deformation is evident even at relatively small displacements. For instance, at $\Delta_y = 20\,\text{mm}$, representing a displacement of the ends of the ribbon by one eighth of the inner diameter, Fig. 5c shows that transverse displacement derivatives $u_{3,1}$ and $u_{3,2}$ attain peak magnitudes of approximately 0.39 and 0.54 respectively, which contradict the assumptions underlying the strain-displacement relationship in the model. Remedies for these shortcomings of the model are possible. As suggested in Ben Amar and Pomeau (1997); Chopin et al. (2015), linearizations inherent to the model can be performed about curvilinear configurations different from the planar unstressed state. This, however, requires a priori knowledge about the deformation.

Unlike the von Kármán theory, the Cosserat rod model permits large displacements of the centerline and large rotations of cross sections. These features ensure good predictions in the transversely displaced annulus and pinched semi annulus experiments. The unfurled annulus experiment, however, exposes the consequences of assuming rigid kinematics for ribbon cross sections. Although predictions show deviations comparable to the width of the ribbon, examining mean curvature distributions truly reveals the repercussions of lumping details of ribbon cross sections into stiffness parameters. Observations such as the ones in Fig. 8 remain true for ribbons that are much narrower than the ones we have used in the experiments, suggesting that the aspect ratios ℓ/w and w/h of our ribbon samples are not unreasonable. Fig. 15b in particular suggests that rod models ignore important energetic contributions stemming from deformability of cross sections, leading to predictions of non physical localization of strains/curvatures along the centerline. Indeed, the unfurled annular ribbon furnishes an example in which the rod model, despite predicting a lower energy than the Cosserat plate, is the less accurate one.

By permitting large surface displacements and director rotations, and by explicitly considering deformability along the width of a ribbon, the Cosserat plate theory is an evident generalization of the models mentioned above. Its favorable comparisons with ribbon shapes and curvatures realized in experiments is a testament to its geometrically exact nature (Fox et al., 1993; Simo and Fox, 1989). We refer to Simo et al. (1990); Sze et al. (2004) for examples demonstrating its performance in an "obstacle course" of benchmark problems for plate and shell structures.

Remarks. We conclude the article with a few remarks.

(i) It is hardly surprising that a fully geometrically nonlinear plate model that permits unrestricted displacements and rotations outperforms a nonlinear rod or a weakly nonlinear plate theory. Indeed, referring back to Fig. 1, it is fairly obvious that the prediction of the 1-director Cosserat plate theory is expected to be the most accurate. The less general theories are useful nevertheless, as many detailed studies in the literature have shown. Table 1 also suggests the same.

(ii) Discrepancies between predictions of von Kármán plate or 2-director Cosserat (effectively Kirchhoff) rod theories and experimental measurements highlighted in Table 1, is, again, foreseeable. Nevertheless, their widespread use in modeling elastic ribbons appears to be at odds with the qualitative and quantitative inconsistencies observed in their predictions for simplistic ribbon deformations.

(iii) Comparisons between model predictions and experimental measurements shown here highlight the importance of kinematic assumptions when modeling geometrically nonlinear deformations of ribbon-like structures. In particular, we find that it is imperative for ribbon models to permit large displacements of the centerline, large rotations of material directors, and to account for deformability of cross sections. While none of these considerations are startling per se, they do not all usually manifest in conventional engineering applications employing beam and plate structures, and consequently, in routinely used structural models.

(iv) Despite what Table 1 may appear to suggest, we do not question the validities of the von Kármán plate and Cosserat rod models. Insightful discussions to this end can be found in Audoly and Pomeau (2010, Parts I, II). Instead, our findings show that the kinematic assumptions underlying them are easily violated in simple experiments with ribbons.

(v) Similarly, it is *not* our conclusion here that ribbons should be modeled as plates. Rather, our study identifies important requirements for dedicated one-dimensional ribbon models. Of course, the utility of such reduced order models will depend on additional factors that require deeper considerations— for instance, bounds on load magnitudes or on aspect ratios of ribbons. Furthermore, we have shown here that predictions of the 1-director Cosserat plate model can serve as a benchmark against which to compare those of models proposed in the literature (Dias and Audoly, 2015; Hinz and Fried, 2015; Starostin and van der Heijden, 2007; Todres, 2015). We refer to (Moore and Healey, 2019; Yu and Hanna, 2019) for discussions of the challenges (and singularities) encountered in simulating these models. Nevertheless, we expect more comprehensive numerical investigations of ribbon models to appear in the literature. Ribbon models derived by dimensional reduction from von Kármán plate theories in Freddi et al. (2018) will benefit from such comparisons as well, especially in light of our observations here.

(vi) An important feature of the Cosserat plate model is that it does not impose inextensibility of the ribbon surface as a constraint. Inextensibility is a reasonable assumption when predicting bending dominated deformations of thin structures, since energetic considerations eliminate the possibility of stretching or shear. It highlights the overwhelming influence of geometry on deformations of slender structures. Nevertheless, it is an idealization. At sufficiently large loads, ribbons develop defects and regions of irreversible damage by yielding or fracture. We showed an instance of localized extension in an experiment using annular ribbons in Fig. 26. In these scenarios, restricting deformations to remain isometric can even result in a divergent energy density (Witten, 2007). Deviations from strict inextensibility

are easy to find in commonly used models as well. For example, as highlighted in Friesecke et al. (2006), inextensibility is usually only enforced in a linearized sense in von Kármán plate theories. The constraint may not even manifest in ribbon models derived by dimensional reduction from plate theories, despite being explicitly imposed in the latter (Freddi et al., 2020). In models that permit combined states of bending and stretching, such as the Cosserat plate theory, a large membrane stiffness functions as a penalty parameter that entices the ribbon to remain developable in bending dominated deformations. Simultaneously, such models allow exploring configurations where contributions from stretching can be significant.

(vii) Table 1 fully justifies our claim that annular ribbons exhibit a tunable degree of nonlinearity in response to simple boundary conditions. By virtue of being predictable by the von Kármán model, we declare that the transversely displaced annulus experiment as showing weak nonlinearity. In the same vein, the unfurled annulus shows a high degree of nonlinearity by virtue of not being reproducible by either the von Kármán (not shown) or the Cosserat rod models. We also draw attention to the magnitudes of curvatures realized in these experiments, which appear to correlate well with the degree of nonlinearity.

(viii) As discussed in Section 7, annular ribbons exhibit a wide range of features including solution multiplicity, symmetry breaking bifurcations and energy localization. The mean radius additionally endows them with a nonzero geodesic curvature. These observations suggest that annular ribbons are interesting mechanical systems in their own right, and their study will augment the existing literature on problems of Möbius strips and ribbons subjected to combined states of tension and twist (Chopin et al., 2015; Green, 1936).

(ix) An important feature of the comparisons between experiments and model predictions we showed here is that they are reproducible. The independence from material parameters, simplicity of the experimental setup and the absence of ad hoc parameters render our comparisons amenable to independent verification.

To facilitate reproducing the simulation results shown for the pinched semi annulus experiment using open source or freely available softwares, we provide three well-documented scripts as supplementary material. The python script provided reproduces predictions of the von Kármán plate model using the open source FEniCS library (Alnæs et al., 2015; Hale et al., 2018). Two Abaqus input files are provided to reproduce simulations of the Cosserat rod and plate models using a free student edition of the software. We urge some caution in comparing our results for the Cosserat models, which are computed using our group's research code to faithfully reproduce the theory outlined in Sections 4 and 5, with Abaqus simulations that employ special modifications of strain measures.

We also note that the experiments shown in the article can be reproduced with minimal infrastructure— in principle, annular ribbons with edges taped to a ruler will suffice. A video demonstration of the unfurled annulus experiment included as supplementary material amply demonstrates this point. Furthermore, shapes of deformed ribbons can be accurately measured using computer vision techniques, whose implementations can be found in open source libraries (Bradski, 2000).

A few directions for future inquiry are apparent at this point. Notice that it is possible for a model to predict the correct shape for a ribbon but not the right deformation mapping. Indeed, composing a deformation map with any shape preserving transformation alters the displacement and strain fields, but not the shape of the ribbon or any of its intrinsic properties. It is therefore necessary to augment shape comparisons shown here with marker-based displacement measurements. Next, coupling numerical approximation algorithms with bifurcation/continuation codes will help inspect solution branches and their stability (Doedel et al., 2007). Such studies will likely reveal the significance of zero crossings in the mean curvature observed in the unfurled annulus experiment in Section 7. It is also prudent to examine the predictive accuracy of the Cosserat plate model in problems that have been previously explored in the literature. In particular, we note the problem of a rectangular ribbon subjected to tension and twist for which detailed experimental observations and analysis is available (Chopin and Kudrolli, 2013; 2016; Kudrolli and Chopin, 2018). The problem of constructing Möbius strips by bending and twisting rectangular ribbons (Fosdick and Fried, 2016) has also be extensively studied, although experimental measurements appear to be sparse.

Appendix A. Approximate deformation mappings and ribbon centerlines from experimental point cloud measurements

We have extensively used shapes of ribbon centerlines and mean curvature distributions along these centerlines computed from experimental measurements to examine accuracies of ribbon models. Noting that ribbon centerlines are not directly identifiable from point cloud measurements, we discuss an algorithm for this purpose. In fact, we outline an algorithm addressing a more general problem— one of explicitly constructing an injective mapping between the reference and deformed configurations of a ribbon, given only a point cloud sampling of the deformed ribbon's shape measured experimentally.

Specifically, we seek a mapping $\psi : \mathcal{B}_0 \to \mathcal{B}$ from the reference configuration $\mathcal{B}_0$ of a ribbon to its deformed configuration $\mathcal{B}$. The main idea consists in transforming this problem into one of parameterizing a triangulation $\mathcal{T}$ of $\mathcal{B}$ over $\mathcal{B}_0$. Such a reformulation enables us to adopt algorithms available in the literature on computational geometry for mesh parameterization to determine ψ. The challenge, however, lies in guaranteeing injectivity of ψ, which is an uncompromisable constraint

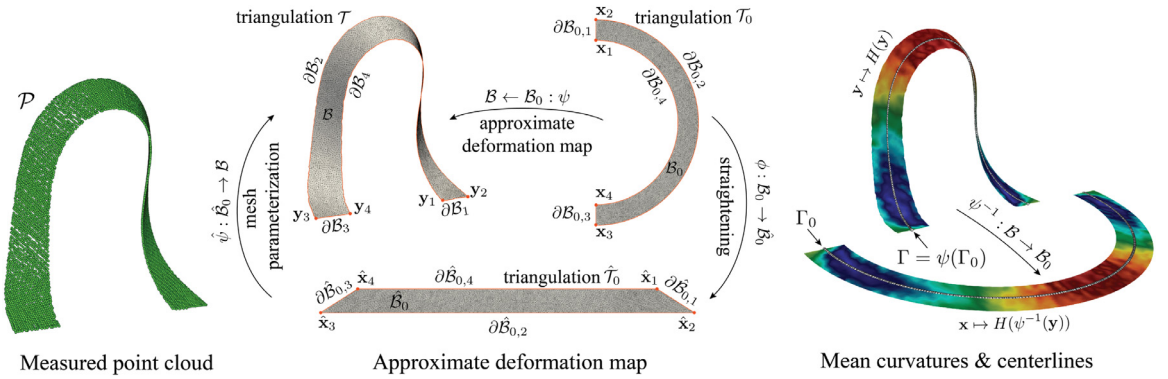

Fig. 27. An illustrative example showing the construction of an injective map $\psi : \mathcal{B}_0 \to \mathcal{B}$ from the reference to the deformed configuration of a ribbon while using only a point cloud sampling $\mathcal{P}$ of $\mathcal{B}$ measured experimentally. The image on the far right shows that ψ helps to visualize mean curvatures over the reference configuration and to identify the centerline of the ribbon in a measured point cloud.

for our purposes. In the following, we use the example of a semi annular ribbon depicted in Fig. 27 as an illustrative aid to discuss the steps in the algorithm.

(i) Starting with a measured point cloud $\mathcal{P}$ sampling the surface of a deformed ribbon, we first compute a triangulation $\mathcal{T}$ of $\mathcal{P}$ using the advancing front surface reconstruction algorithm of (Cohen-Steiner and Da, 2004). The set triangulated by $\mathcal{T}$ defines the deformed configuration $\mathcal{B}$.

(ii) Next, we introduce a trapezoidal intermediate configuration $\hat{\mathcal{B}}_0$. The lengths of the sides $\hat{\mathbf{x}}_1 - \hat{\mathbf{x}}_4$ and $\hat{\mathbf{x}}_2 - \hat{\mathbf{x}}_3$ of the trapezoid equal the inner and outer perimeters of the ribbon, namely $\pi \mathrm{R}_i$ and $\pi \mathrm{R}_0$ respectively, while its height is set to equal the ribbon width $w = \mathrm{R}_0 - \mathrm{R}_i$. In the following, we compute $\hat{\psi} : \hat{\mathcal{B}}_0 \to \mathcal{B}$ using a mesh parameterization algorithm. Then, letting $\phi : \mathcal{B}_0 \to \hat{\mathcal{B}}_0$ denote a simple "straightening" of the semi annulus $\mathcal{B}_0$ into the trapezoid $\hat{\mathcal{B}}_0$, we shall set $\psi = \hat{\psi} \circ \phi : \mathcal{B}_0 \to \mathcal{B}$. We construct $\hat{\psi} : \hat{\mathcal{B}}_0 \to \mathcal{B}$ itself in two steps— by prescribing its correspondence between the boundaries $\partial\hat{\mathcal{B}}_0$ and $\partial\mathcal{B}$, and then by extending $\hat{\psi}$ to the interior as a map that parameterizes the mesh $\mathcal{T}$ covering $\mathcal{B}$ over $\hat{\mathcal{B}}_0$.

(iii) For the purpose of defining $\hat{\psi}$ over $\partial\hat{\mathcal{B}}_0$, we partition the boundaries $\partial\hat{\mathcal{B}}_0$ and $\partial\mathcal{B}$ into four corresponding components as demarcated by their four corners. Referring to Fig. 27, we denote the corners along $\partial\hat{\mathcal{B}}_0$ by $\hat{\mathbf{x}}_1, \ldots, \hat{\mathbf{x}}_4$ and the four boundary components they determine by $\partial\hat{\mathcal{B}}_{0,i}$ for $i = 1$ to 4. The analogous corners and components of $\partial\mathcal{B}$ are labeled $\mathbf{y}_1, \ldots, \mathbf{y}_4$ and $\partial\mathcal{B}_i$ for $i = 1$ to 4, respectively.
Next, we prescribe the mapping between corresponding boundary components through their arc length parameters. Specifically, consider the pair of corresponding boundary components $\partial\hat{\mathcal{B}}_{0,i}$ and $\partial\mathcal{B}_i$. Let these curves have lengths $\hat{L}_i$ and ℓ_i, and denote their arc length parameterizations by $S \mapsto \hat{\boldsymbol{\lambda}}_i(S)$ and $s \mapsto \boldsymbol{\lambda}_i(s)$, respectively. We explicitly prescribe the correspondence between $\partial\hat{\mathcal{B}}_{0,i}$ and $\partial\mathcal{B}_i$ as $\hat{\psi}(\hat{\boldsymbol{\lambda}}_i(S)) = \boldsymbol{\lambda}_i(\ell_i S/\hat{L}_i)$ for $0 \le S \le \hat{L}_i$ and for $i = 1$ to 4.

(iv) We extend $\hat{\psi}$ to the interior of $\mathcal{B}_0$ as a mapping that parameterizes the triangulation $\mathcal{T}$ of $\mathcal{B}$ over $\hat{\mathcal{B}}_0$. For this, we adopt the algorithm of Floater (2003) using mean value coordinates and its implementation provided in CGAL (Alliez et al., 2019). In particular, the algorithm determines a triangulation $\hat{\mathcal{T}}_0$ over $\hat{\mathcal{B}}_0$ having identical connectivity as $\mathcal{T}$. It defines $\hat{\psi}$ as a homeomorphism from $\hat{\mathcal{T}}_0$ to $\mathcal{T}$ that is affine over each triangle in $\hat{\mathcal{T}}_0$ and is specified by its values at the vertices of $\hat{\mathcal{T}}_0$.

(v) Finally, letting $\phi : \mathcal{B}_0 \to \hat{\mathcal{B}}_0$ denote the canonical map that straightens out the semi annulus $\mathcal{B}_0$ to the trapezoid $\hat{\mathcal{B}}_0$, we set $\psi \triangleq \hat{\psi} \circ \phi$. The main reason to introduce the intermediate configuration $\hat{\mathcal{B}}_0$ is to ensure injectivity of ψ. By virtue of Tutte's theorem on sufficient conditions for perfect graph matchings (Tutte, 1963), it is guaranteed that the mesh parameterization $\hat{\psi} : \hat{\mathcal{B}}_0 \to \mathcal{B}$ is injective if $\hat{\mathcal{B}}_0$ is convex. It is precisely for this reason that we parameterize the mesh $\mathcal{T}$ over a trapezoidal domain $\hat{\mathcal{B}}_0$ rather than over the non convex domain $\mathcal{B}_0$. Then, injectivity of $\hat{\psi}$ and ϕ guarantee that $\psi = \hat{\psi} \circ \phi$ is injective as well, just as required.

Our final remark on the construction of ψ concerns its interpretation as an approximation of the actual deformation mapping $\varphi : \mathcal{B}_0 \to \mathcal{B}$. This interpretation is supported (only) qualitatively by the observations that $\mathcal{B} = \psi(\mathcal{B}_0)$, $\partial\mathcal{B}_i = \psi(\partial\mathcal{B}_{i,0})$ and $\mathbf{y}_i = \psi(\mathbf{x}_i)$ for each $i = 1$ to 4, just as is the case for φ. In fact, since the domain and range of φ and ψ are identical and both maps are injective, it follows that there exists an automorphism $\chi : \mathcal{B}_0 \to \mathcal{B}_0$ such that $\psi = \varphi \circ \chi$, showing that φ and ψ coincide up to a reparameterization of the reference configuration. This observation reveals that although ψ defines the correct shape for the deformed configuration, in general, it determines an inaccurate metric. Since we expect bending dominated deformations in our experiments to result in negligible membrane strains, we deliberately construct ψ such that the metric it defines for $\mathcal{B}$ remains close to the identity. In particular, the arc length-based parameterization of boundary components by $\hat{\psi}$, and its extension to $\hat{\mathcal{B}}_0$ as a mesh parameterization that can be understood as a discrete approximation of a conformal mapping from $\hat{\mathcal{B}}_0$ to $\mathcal{B}$, are choices that help to ensure that ψ results only in small metric

changes, and in turn, represents a useful approximation of φ for our purposes. In all our examples, we have verified this feature of our construction for ψ by inspecting the triangulation $\mathcal{T}_0$ over $\mathcal{B}_0$ defined as the pre-image $\psi^{-1}(\mathcal{T})$ of $\mathcal{T}$. That is, $\mathcal{T}_0$ has identical connectivity as $\mathcal{T}$, while its vertices are located at the pre-images of corresponding vertices in $\mathcal{T}$. Inspecting triangle quality metrics reveals that triangles in $\mathcal{T}_0$ are only mildly distorted from their respective counterparts in $\mathcal{T}$.

With an approximate deformation mapping ψ at hand, it is straightforward to pull back fields defined over the deformed configuration to the reference. The inverse map $\psi^{-1} = \phi^{-1} \circ \hat{\psi}^{-1}$ is also explicitly computable owing to the fact that the inverses of ϕ and $\hat{\psi}$ are both easily determined. Then, we map mean curvatures $\mathbf{y} \in \mathcal{B} \mapsto H(\mathbf{y})$ computed over the deformed configuration as discussed in Section 2, back to the reference as $\mathbf{x} \in \mathcal{B}_0 \mapsto H(\psi^{-1}(\mathbf{y}))$. Finally, we determine centerlines of ribbons in the deformed configuration simply as the images of centerlines in the reference under ψ.

Appendix B. Remarks on finite element simulations

Computing finite element approximations of the geometrically nonlinear models considered in the article is a challenging task. Since the literature on the topic is extensive, in the following, we briefly highlight the main ideas underlying our simulations of the von Kármán, Cosserat rod and Cosserat plate models. The ensuing discussions are not intended to serve as a comprehensive review, but as a reminder of some of the interesting issues that arise when simulating geometrically nonlinear models. For each model, we point to references in the literature for detailed descriptions.

B1. The von Kármán plate model

Simulating the von Kármán plate model using a conforming finite element method requires constructing spaces of continuously differentiable (C^1) functions to approximate the transverse displacement. This is more generally the case for plate models that invoke the Kirchhoff assumption. It is indeed possible to construct C^1 basis functions using specially designed elements such as the Argyris triangle (Ciarlet, 1978), using spline functions (Kiendl et al., 2009), using special techniques such as subdivision surfaces (Cirak et al., 2000), or by using mesh-independent interpolation methods (Millán et al., 2011). Mixed finite element methods help bypass the C^1 requirement by independently approximating displacements and their derivatives Boffi et al. (2013, Chapter 10). We resort to a simpler strategy here, that consists in enforcing the Kirchhoff condition weakly as a constraint, rather than by directly incorporating it in the set of admissible solutions. In essence, such an approach amounts to introducing a transversely shearable version of the model discussed in Section 3.1, while penalizing the appearance of transverse shear strains in the computed approximations. Since the ribbons used in our examples are thin, we expect transverse shear strains to be vanishingly small. Transverse shear is hence a numerical artifice, which we verify to be negligibly small a posteriori.

Specifically, we replace the 3-field problem for extremizing Π^{vK} to compute displacement components (u_1, u_2, u_3) by a 5-field formulation that additionally introduces (infinitesimal) rotations $\boldsymbol{\psi} = (\psi_1, \psi_2) : \Omega_0 \to \mathbb{R}^2$ of material fibers along the thickness of the ribbon. Satisfying the Kirchhoff assumption requires imposing the constraint $\boldsymbol{\psi} = \nabla u_3$. To this end, we replace the energy functional Π^{vk} by

$$\begin{aligned} &\Pi' = \Pi^{\text{vk}}_{\text{m}} + \Pi'_{\text{s}} + \Pi'_{\text{b}}, \qquad (36)\\ \text{where}\quad &\Pi'_{\text{b}} = \frac{1}{2}\int_{\Omega_0} \frac{h^3}{12}\left(\text{G}(\psi_{1,2}+\psi_{2,1})^2 + \frac{\text{E}}{(1-\nu^2)}(\psi_{1,1}^2 + \psi_{2,2}^2 + 2\nu\psi_{1,1}\psi_{2,2})\right) d\mathbf{x},\\ &\Pi'_{\text{s}} = \frac{\text{K}}{2}\int_{\Omega_0} \left((u_{3,1}-\psi_1)^2 + (u_{3,2}-\psi_2)^2\right) d\mathbf{x}, \end{aligned}$$

$\text{G} = \text{E}/((2(1+\nu))$ is the shear modulus and K is a sufficiently large penalty parameter. Unlike Eqs. (3), Eq. (36) does not involve any second derivatives of transverse displacements. The term Π'_{s} represents the energetic contribution arising from transverse shear, which in our context, is interpreted as the penalty for deviations from the Kirchhoff constraint. In the case when $\boldsymbol{\psi}$ coincides with ∇u_3, implying satisfaction of the Kirchhoff condition, notice that $\Pi'_{\text{s}} = 0$, the bending term Π'_{b} coincides with $\Pi^{\text{vk}}_{\text{b}}$, and the total energy Π' equals Π^{vk}. The penalty parameter K implicitly sets the tolerance on permitted magnitudes of transverse shear strains. In our calculations, we set $\text{K} = \text{G}h$, so that Π' reduces to the strain energy functional of a *shearable* von Kármán plate. While useful in its own right for modeling deformations of moderately thick plates, we effectively employ it here for ease of finite element implementation by circumventing the Kirchhoff condition when computing numerical simulations. We adopt the implementation of the model in Eq. (36) provided by the authors of Hale et al. (2018) within the framework of the FEniCS open source library (Alnæs et al., 2015). The implementation employs partial selective reduced integration to avoid numerical locking, conforming piecewise quadratic triangle elements for displacement components, linear triangle elements enriched with cubic bubble functions to approximate rotation fields, and nonlinear solvers implemented in the PETSc library (Balay and et al, 2019) for resolving the set of nonlinear equations resulting from discretization. In all our examples, we verify convergence of finite element solutions using mesh refinement as well as by elevating the degrees of polynomial shape functions used.

B2. The 2-director Cosserat rod model

Recall from Section 4.1 that the configuration of a ribbon modeled as a Cosserat rod is specified as $\Phi = (\varphi_0(S), \Lambda(S)) \in \mathbb{R}^3 \times \mathrm{SO}(3))$, where φ_0 determines the location of the centerline and Λ orients the moving frame positioned at each point along the centerline. One of the principal challenges in computing such configurations stems from the fact that rotations $S \mapsto \Lambda(S)$ do not belong to a linear space, but to the nonlinear manifold SO(3). The pointwise constraint $\Lambda^{\mathrm{T}}\Lambda = \mathbf{I}$ highlights the non triviality of constructing finite element spaces for numerical approximation. These issues have been well recognized in the literature, and are usually addressed by (locally) parameterizing rotations, using Euler angles for instance (Stuelpnagel, 1964). The choice of coordinates is critical both in ensuring satisfaction of the constraint as well as in deriving the equilibrium equations. Here, we adopt the approach of (Simo and Vu-Quoc, 1986) using local exponential coordinates.

To deduce the weak form satisfied by an extremizer of Eq. (7), introduce the 1-parameter family of perturbed configurations $\Phi_\varepsilon = (\varphi_{0\varepsilon}, \Lambda_\varepsilon)$

$$\varphi_{0\varepsilon}(S) = \varphi_0(S) + \varepsilon\boldsymbol{\eta}_0(S) \quad \text{and} \quad \Lambda_\varepsilon(S) = \exp(\varepsilon\hat{\boldsymbol{\vartheta}}(S))\Lambda(S), \tag{37}$$

where $\varepsilon > 0$ is the perturbation parameter, $\boldsymbol{\eta}_0 \in \mathbb{R}^3$ is an admissible variation of the centerline coordinates φ_0, the hat operator $\boldsymbol{\vartheta} \mapsto \hat{\boldsymbol{\vartheta}}$ denotes the isomorphism from $\mathbb{R}^3$ to so(3), and $\boldsymbol{\vartheta} \in \mathbb{R}^3$ determines the skew-symmetric tensor field $\hat{\boldsymbol{\vartheta}} \in \mathrm{so}(3)$ representing an admissible variation of the frame rotation Λ. The exponential map $\exp\colon \mathrm{so}(3) \to \mathrm{SO}(3)$ in Eq. (37) transforms infinitesimal rotations in the Lie algebra so(3) to finite rotations in the group SO(3). The perturbed rotation Λ_ε can therefore be interpreted as the result of superimposing an infinitesimal rotation $\hat{\boldsymbol{\vartheta}}$ on Λ. Most significantly, Eq. (37) provides a canonical construction for admissible configurations Φ_ϵ in the vicinity of Φ, while permitting admissible variations $\boldsymbol{\eta}_0$ and $\boldsymbol{\vartheta}$ to belong to *linear* spaces.

Armed with Eq. (37), we compute the first variation of the energy functional in Eq. (7) as (Simo and Vu-Quoc, 1986, Section 4):

$$G(\Phi, (\boldsymbol{\eta}_0, \boldsymbol{\vartheta})) \triangleq \lim_{\varepsilon\to 0} \frac{d}{d\varepsilon}\Pi^{\mathrm{CR}}[\Phi_\varepsilon] = \int_{S=0}^{\ell} \left\{ \mathbf{N}\cdot\Lambda^{\mathrm{T}}\left(\frac{d\boldsymbol{\eta}_0}{dS} - \boldsymbol{\vartheta}\times\frac{d\varphi_0}{dS}\right) + \mathbf{M}\cdot\Lambda^{\mathrm{T}}\frac{d\boldsymbol{\vartheta}}{dS}\right\} dS, \tag{38a}$$

$$\text{where} \quad \mathbf{N} = \mathrm{diag}[\mathrm{GA}, \mathrm{GA}, \mathrm{EA}]\,\boldsymbol{\Gamma} \quad \text{and} \quad \mathbf{M} = \mathrm{diag}[\mathrm{EI}_1, \mathrm{EI}_2, \mathrm{GJ}]\,\mathbf{K} \tag{38b}$$

are the resultant force and couple, respectively. The statement of virtual work in Eq. (38a) is the point of departure for computing finite element approximations of Φ. While G is expectedly linear in the variations $(\boldsymbol{\eta}_0, \boldsymbol{\vartheta})$, it depends nonlinearly on the configuration (φ_0, Λ). An added source of nonlinearity stems from Λ belonging to the nonlinear manifold SO(3). Eq. (38b) serves as a reminder that nonlinearity in Eq. (38a) is purely geometric.

We compute finite element approximations of Φ satisfying Eq. (38a) by computing configurational increments, rather than by parameterizing the nonlinear manifold of admissible solutions (Simo and Vu-Quoc, 1986). To this end, we linearize G for an admissible increment $\Delta\Phi = (\Delta\varphi_0, \Delta\theta) \in \mathbb{R}^3 \times \mathbb{R}^3$ as

$$L[G(\Phi, (\boldsymbol{\eta}_0, \boldsymbol{\vartheta}))] = G(\Phi, (\boldsymbol{\eta}_0, \boldsymbol{\vartheta})) + \underbrace{\lim_{\varepsilon\to 0} \frac{d}{d\varepsilon} G((\varphi_0 + \varepsilon\Delta\varphi_0, \exp(\varepsilon\widehat{\Delta\boldsymbol{\theta}})\Lambda), (\boldsymbol{\eta}_0, \boldsymbol{\vartheta}))}_{DG(\Phi,(\boldsymbol{\eta},\boldsymbol{\vartheta}))\cdot\Delta\Phi}, \tag{39}$$

in which the notation $DG(\Phi, (\boldsymbol{\eta}, \boldsymbol{\vartheta})) \cdot \Delta\Phi$ is chosen to convey the linear dependence of the directional derivative on the configuration increment $\Delta\Phi$. For the purpose of finite element approximation, we interpret $(\boldsymbol{\eta}_0, \boldsymbol{\vartheta})$ to denote test functions and $(\Delta\varphi_0, \Delta\theta)$ to denote the solution increment of interest. Observe that these test functions and increments belong to linear spaces for which finite element subspaces can be constructed in the usual way. At a given configuration Φ, $G(\Phi, (\boldsymbol{\eta}_0, \boldsymbol{\vartheta}))$ represents the finite element residual while $DG(\Phi, (\boldsymbol{\eta}_0, \boldsymbol{\vartheta})) \cdot \Delta\Phi$ determines the stiffness matrix, see Simo and Vu-Quoc (1986) for detailed expressions. In our calculations, we use function spaces spanned by piecewise cubic polynomials defined over a uniform subdivision of the interval $[0, \ell]$ for both test functions and solution increments. Using cubic polynomial elements helps circumvent issues of numerical locking, which is conventionally handled in low order elements using reduced integration techniques. In this way, Eq. (39) yields a system of linear equations for the increment $\Delta\Phi$. Then, a configurational update mirroring Eq. (37) advances the configuration to the next iterate:

$$\varphi_0 \leftarrow \varphi_0 + \Delta\varphi_0 \quad \text{and} \quad \Lambda \leftarrow \exp(\widehat{\Delta\theta})\Lambda. \tag{40}$$

In summary, the numerical algorithm to compute an equilibrium configuration for a prescribed set of Dirichlet boundary conditions at the sections $S = 0$ and $S = \ell$ consists of the following steps: start with an initial guess $\Phi^0 = (\varphi_0^0, \Lambda^0)$ for the configuration, assemble the residual vector and stiffness matrix, solve the linear system of equations in Eq. (39) to determine the increment $\Delta\Phi^0$, and update the configuration to $\Phi_1 = (\varphi_0^1, \Lambda^1) = (\varphi_0^0 + \Delta\varphi^0, \exp(\widehat{\Delta\theta^0})\Lambda^0)$. We repeat this process iteratively to compute the sequence of configurations $\Phi^2, \Phi^3, \ldots$ and terminate the algorithm at the k^{th} iteration when the magnitude of the configurational increment $\Delta\Phi^k$ is deemed to be sufficiently small, and set Φ^k to be the finite element approximation of the required equilibrium solution.

B3. The 1-director Cosserat plate model

The configuration of a 1-director Cosserat plate is defined by the pairing $\Phi = (\varphi, \mathbf{t})$, where φ determines the location of the mid surface and $\mathbf{t}$ defines the orientations of inextensible directors. Then, a key step in deducing the weak form satisfied by extremizers of the energy functional in Eq. (21) lies in constructing admissible perturbations of Φ. Since $\mathbf{t} \in \mathbb{S}^2$, its variations belong to the tangent space

$$\mathrm{T}_{\mathbf{t}}\mathbb{S}^2 = \{\delta\mathbf{t} \in \mathbb{R}^3 \,:\, \delta\mathbf{t}\cdot\mathbf{t} = 0\}. \tag{41}$$

Despite the linear nature of the orthogonality constraint, constructing $\mathrm{T}_{\mathbf{t}}\mathbb{S}^2$ following Eq. (41) is problematic in practice because the constraint is configuration-dependent. It is in fact usually necessary to explicitly parameterize $\mathbb{S}^2$ to define admissible director variations. This, however, begets numerical issues concerning singularities in 2-parameter charts (e.g., Euler angles) and pointwise constraints in 3-parameter charts.

To aid in constructing director variations in a singularity-free manner, following (Simo and Fox, 1989), introduce the unique drill-free rotation $\Lambda \in \mathrm{SO}(3)$ that maps $\mathbf{E}_3$ to $\mathbf{t}$:

$$\Lambda = (\mathbf{t}\cdot\mathbf{E}_3)\mathbf{I} + \widehat{(\mathbf{E}_3 \times \mathbf{t})} + \frac{(\mathbf{E}\times\mathbf{t})\otimes(\mathbf{E}\times\mathbf{t})}{1+\mathbf{t}\cdot\mathbf{E}_3}. \tag{42}$$

Eq. (42) establishes an injective correspondence between $\mathbb{S}^2$ and a subset of SO(3) consisting of rotations whose axis is orthogonal to $\mathbf{E}_3$. This identification is convenient because it facilitates an alternate construction for the tangent space in Eq. (41) as

$$\mathrm{T}_{\mathbf{t}}\mathbb{S}^2 = \{\Lambda\,\delta\mathbf{T} \,:\, \delta\mathbf{T} \in \mathbb{R}^3,\ \delta\mathbf{T}\cdot\mathbf{E}_3 = 0\}. \tag{43}$$

That $\delta\mathbf{t} = \Lambda\delta\mathbf{T}$ is an admissible variation follows easily from $\mathbf{t}\cdot\Lambda\,\delta\mathbf{T} = \Lambda\,\mathbf{E}_3\cdot\Lambda\,\delta\mathbf{T} = \mathbf{E}_3\cdot\delta\mathbf{T} = 0$. In effect, introducing Λ transforms the configuration-dependent constraint $\delta\mathbf{t}\cdot\mathbf{t} = 0$ into a simple coordinate restriction $\delta\mathbf{T}\cdot\mathbf{E}_3 = 0$. Given $(\delta\varphi, \delta\mathbf{T}) \in \mathbb{R}^3\times\mathbb{R}^3$ such that $\delta\mathbf{T}\cdot\mathbf{E}_3 = 0$, we can now construct a 1-parameter family of perturbations $\Phi_\varepsilon = (\varphi_\epsilon, \mathbf{t}_\epsilon)$ of Φ as

$$\varphi_\epsilon = \varphi + \epsilon\delta\varphi \quad \text{and} \quad \mathbf{t}_\epsilon = \exp_{\mathbf{t}}(\epsilon\delta\mathbf{t}) = \cos\|\epsilon\delta\mathbf{t}\|\mathbf{t} + \frac{\sin\|\epsilon\delta\mathbf{t}\|}{\|\epsilon\delta\mathbf{t}\|}\epsilon\delta\mathbf{t}, \tag{44}$$

where $\delta\mathbf{t} = \Lambda\,\delta\mathbf{T}$ and $\exp_{\mathbf{t}} : \mathrm{T}_{\mathbf{t}}\mathbb{S}^2 \to \mathbb{S}^2$ is the exponential map of the unit sphere. Corresponding variations $\delta\boldsymbol{\varepsilon}$, $\delta\boldsymbol{\gamma}$ and $\delta\boldsymbol{\kappa}$ of the strain measures are straightforward to compute using their definitions in Eq. (19). Then, for an admissible variation $\delta\Phi = (\delta\varphi, \delta\mathbf{t})$, the first variation of the energy functional follows from Eq. (21) as

$$G(\Phi, (\delta\varphi, \delta\mathbf{t})) \triangleq \lim_{\epsilon\to 0}\frac{d}{d\epsilon}\Pi^{\mathrm{CS}}[\Phi_\epsilon] = \int_{\Omega_0}\left(n^{\alpha\beta}\delta\varepsilon_{\alpha\beta} + q^{\alpha}\delta\gamma_\alpha + m^{\alpha\beta}\delta\kappa_{\alpha\beta}\right)\mathrm{J}d\Omega_0. \tag{45}$$

As was the case in Section B.2, for the purpose of finite element calculations, it is convenient to identify an equilibrium configuration Φ satisfying $G(\Phi, \delta\Phi) = 0$ for every $\delta\Phi$ admissible, in an incremental manner rather than by parameterizing the configuration manifold $\mathbb{R}^3\times\mathbb{S}^2$. To this end, we linearize Eq. (45) about Φ by an admissible increment $\Delta\Phi = (\Delta\varphi, \Delta\mathbf{t} = \Lambda\Delta\mathbf{T})$ satisfying $\Delta\mathbf{T}\cdot\mathbf{E}_3 = 0$ to get

$$LG(\Phi, (\delta\varphi, \delta\mathbf{t})) = G(\Phi, (\delta\varphi, \delta\mathbf{t})) + DG(\Phi, (\delta\varphi, \delta\mathbf{t})\cdot(\Delta\varphi, \Delta\mathbf{t})), \tag{46}$$

where the directional derivative is computed using Eq. (45) as

$$\begin{aligned} DG(\Phi, (\delta\varphi, \delta\mathbf{t}))\cdot(\Delta\varphi, \Delta\mathbf{t}) = &\int_{\Omega_0}\left(\Delta\left(\mathrm{J}n^{\alpha\beta}\right)\delta\varepsilon_{\alpha\beta} + \Delta(\mathrm{J}q^{\alpha})\delta\gamma_\alpha + \left(\mathrm{J}\Delta m^{\alpha\beta}\right)\delta\kappa_{\alpha\beta}\right)d\Omega_0 \\ &+ \int_{\Omega_0}\left(n^{\alpha\beta}\Delta\delta\varepsilon_{\alpha\beta} + q^{\alpha}\Delta\delta\gamma_\alpha + m^{\alpha\beta}\Delta\delta\kappa_{\alpha\beta}\right)\mathrm{J}d\Omega_0. \end{aligned} \tag{47}$$

Computing the variations/increments of stress resultants and strains appearing in Eq. (47) is straightforward in principle, see (Simo et al., 1990, Section 5). Once $\Delta\Phi$ is determined, we update the configuration as

$$\varphi \leftarrow \varphi + \Delta\varphi \quad \text{and} \quad \mathbf{t} \leftarrow \exp_{\mathbf{t}}(\Lambda\Delta\mathbf{T}). \tag{48}$$

The linearized weak form in Eq. (46) and the update procedure in Eq. (48) are the basis of our algorithm to approximate an equilibrium solution Φ satisfying $G(\Phi, \delta\Phi) = 0$. The finite element discretization of Eq. (46) consists in restricting test functions $\delta\Phi = (\delta\varphi, \delta\mathbf{t} = \Lambda\delta\mathbf{T})$ and configuration increments $\Delta\Phi = (\Delta\varphi, \Delta\mathbf{t} = \Lambda\Delta\mathbf{T})$ to finite dimensional spaces. We adopt finite element function spaces spanned by piecewise cubic polynomials defined over a triangular discretization of Ω_0 for both test functions and increments, while restricting the components $\delta\mathbf{T}\cdot\mathbf{E}_3$ and $\Delta\mathbf{T}\cdot\mathbf{E}_3$ to be zero so that the corresponding variation $\delta\mathbf{t}$ and increment $\Delta\mathbf{t}$ are admissible. Choosing high order shape functions helps circumvent issues related to numerical locking. At a given configuration Φ, restricting $\delta\Phi$ and $\Delta\Phi$ to the finite element space transforms Eq. (46) into a system of linear equations for the increment $\Delta\Phi$. The first integral in Eq. (47) constitutes to the "material" part of the stiffness matrix, while the second term is commonly referred to as the "geometric" part. This terminology is motivated by the fact that the geometric part stems from the nonlinear strain-displacement relationship in Eq. (19). In particular, the geometric part vanishes in plate models employing a linear strain-displacement relationship.

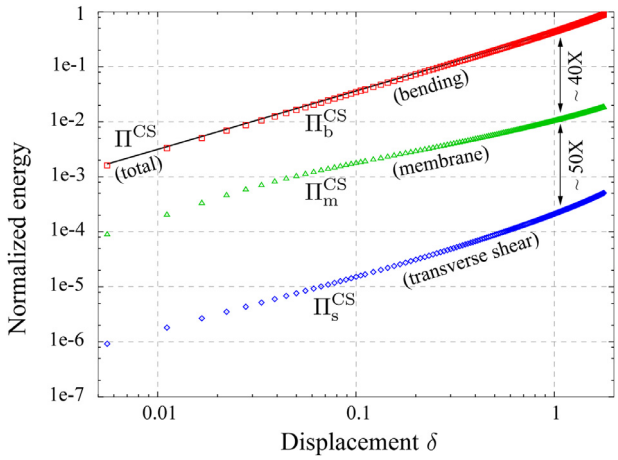

Fig. 28. Contributions from membrane, transverse shear and bending components to the total energy in simulations of the pinched semi annulus experiment using the Cosserat plate model.

For a given set of Dirichlet boundary conditions and an initial guess $\Phi^0 = (\varphi^0, \mathbf{t}^0)$ for the equilibrium configuration, we follow an iterative solution procedure consisting in (i) assembling the residual $G(\Phi^0, \delta\Phi)$ and the stiffness matrix defined by $DG(\Phi^0, \delta\Phi) \cdot \Delta\Phi$, (ii) resolving the linear system in Eq. (46) to compute the increments $\Delta\varphi^0$ and $\Delta\mathbf{T}^0$, and (iii) incrementing the configuration to the next iterate $\Phi^1 = (\varphi_0 + \Delta\varphi^0, \exp_{\mathbf{t}^0}(\Lambda^0 \Delta\mathbf{T}^0))$. We repeat this procedure until configurational increments are deemed to be sufficiently small.

The connections between the Cosserat rod and plate models, which was only briefly alluded to in Section 5.1, are also evident in the algorithms for computing their finite element approximations. The configuration spaces in both models are nonlinear manifolds, namely $\mathbb{R}^3 \times \mathrm{SO}(3)$ in the rod model and $\mathbb{R}^3 \times \mathbb{S}^2$ in the plate model. Conventional approaches either parameterize the configuration manifold explicitly, or incorporate pointwise constraints while choosing a convenient but improper system of coordinates. Our approach is based on the insightful observation in Simo (1985); Simo et al. (1990) that configurational increments belonging to the tangent bundle of the configuration manifold are amenable to straightforward finite element approximation. The computed increments in the tangent spaces are then mapped back to the configuration manifold using explicit and singularity-free definitions of the exponential maps for SO(3) and $\mathbb{S}^2$ in the rod and plate models, respectively.

B4. Simulation of bending dominated deformations

Due to the small thicknesses of our ribbon samples, we expect the deformations observed in our experiments to be bending-dominated. Nevertheless, the rod and plate models discussed above permit extensibility and transverse shear. Besides being more general purpose, these models are more convenient to simulate than ones that explicitly incorporate inextensibility/unshearability constraints.

In the context of bending dominated deformations, membrane and shear modulii in the models discussed above serve as penalty parameters that weakly impose inextensibility and unshearability constraints. To illustrate this point, Fig. 28 shows contributions from membrane, shear and bending deformations to the total energy in a simulation of the pinched semi annulus experiment using the Cosserat plate model. These contributions are labelled as $\Pi_{\mathrm{m}}^{\mathrm{CS}}$, $\Pi_{\mathrm{s}}^{\mathrm{CS}}$ and $\Pi_{\mathrm{b}}^{\mathrm{CS}}$ in Eq. (21). The plot confirms that $\Pi_{\mathrm{b}}^{\mathrm{CS}}$ is at least an order of magnitude larger than $\Pi_{\mathrm{m}}^{\mathrm{CS}}$ and $\Pi_{\mathrm{s}}^{\mathrm{CS}}$. In this sense, the model indeed predicts that the mid surface remains approximately isometric to the undeformed state, as well as approximate satisfaction of the Kirchhoff condition. A similar observation holds for simulations using the Cosserat rod model, which implies that our conclusions concerning it in Table 1 extend to the Kirchhoff rod model as well.

Declaration of Competing Interest

The authors do not report any conflict of interest.

Supplementary material

Supplementary material associated with this article can be found, in the online version, at doi:10.1016/j.jmps.2020.104070.

CRediT authorship contribution statement

Arun Kumar: Methodology, Software, Investigation, Writing - review & editing. **Poornakanta Handral:** Validation, Resources, Investigation. **C S Darshan Bhandari:** Validation, Resources. **Anindya Karmakar:** Methodology. **Ramsharan Rangarajan:** Conceptualization, Methodology, Software, Investigation, Writing - original draft, Funding acquisition.

References

Agostiniani, V., DeSimone, A., Koumatos, K., 2017. Shape programming for narrow ribbons of nematic elastomers. J. Elast. 127 (1), 1–24.
Alliez, P., Giraudot, S., Jamin, C., Lafarge, F., Mérigot, Q., Meyron, J., Saboret, L., Salman, N., Wu, S., 2019. Point set processing. CGAL User and Reference Manual, 5.0 ed. CGAL Editorial Board.
Alnæs, M., Blechta, J., Hake, J., Johansson, A., Kehlet, B., Logg, A., Richardson, C., Ring, J., Rognes, M., Wells, G., 2015. The FEniCS project version 1.5. Arch. Numer. Softw. 3 (100). doi:10.11588/ans.2015.100.20553.
Antman, S., 1974. Kirchhoff's problem for nonlinearly elastic rods. Q. J. Mech. Appl. Math. 32 (3), 221–240.
Antman, S., 1995. Nonlinear plasticity. In: Nonlinear Problems of Elasticity. Springer, pp. 603–628.
Armon, S., Aharoni, H., Moshe, M., Sharon, E., 2014. Shape selection in chiral ribbons: from seed pods to supramolecular assemblies. Soft Matter 10 (16), 2733–2740.
Audoly, B., Pomeau, Y., 2010. Elasticity and Geometry: From Hair Curls to the Non-linear Response of Shells. Oxford University Press.
Audoly, B., Seffen, K., 2015. Buckling of naturally curved elastic strips: the ribbon model makes a difference. J. Elast. 1 (119), 293–320.
Balay, S., et al, 2019. PETSc Web page. https://www.mcs.anl.gov/petsc.
Başar, Y., Ding, Y., 1992. Finite-rotation shell elements for the analysis of finite-rotation shell problems. Int. J. Numer. Meth. Eng. 34 (1), 165–169.
Ben Amar, M., Pomeau, Y., 1997. Crumpled paper. Proc. R. Soc. A 453 (1959), 729–755.
Besl, P.J., McKay, N.D., 1992. A method for registration of 3-D shapes. IEEE Trans. Pattern Anal. Mach. Intell. 14 (2), 239–256. doi:10.1109/34.121791.
Boffi, D., Brezzi, F., Fortin, M., 2013. Mixed Finite Element Methods and Applications, 44. Springer.
Bradski, G., 2000. The OpenCV library. Dr. Dobb's J. Softw. Tools 25, 120–125.
do Carmo, M., 2016. Differential Geometry of Curves and Surfaces. Dover Books on Mathematics. Dover Publications.
Cazals, F., Pouget, M., 2005. Estimating differential quantities using polynomial fitting of osculating jets. Comput. Aided Geom. Des. 22 (2), 121–146.
Chopin, J., Démery, V., Davidovitch, B., 2015. Roadmap to the morphological instabilities of a stretched twisted ribbon. J. Elast. 119 (1–2), 137–189.
Chopin, J., Kudrolli, A., 2013. Helicoids, wrinkles, and loops in twisted ribbons. Phys. Rev. Lett. 111 (17), 174302.
Chopin, J., Kudrolli, A., 2016. Disclinations, e-cones, and their interactions in extensible sheets. Soft Matter 12 (19), 4457–4462.
Ciarlet, P., 1978. The Finite Element Method for Elliptic Problems. Elsevier Science. ISSN
Ciarlet, P., 1980. A justification of the von Kármán equations. Arch. Ration. Mech. Anal. 73 (4), 349–389.
Ciarlet, P., 1997. Mathematical Elasticity: Volume II: Theory of Plates, 27. Elsevier.
Cirak, F., Ortiz, M., Schröder, P., 2000. Subdivision surfaces: a new paradigm for thin-shell finite-element analysis. Int. J. Numer. Meth. Eng. 47 (12), 2039–2072.
Cohen-Steiner, D., Da, F., 2004. A greedy delaunay-based surface reconstruction algorithm. Vis. Comput. 20 (1), 4–16.
Dias, M., Audoly, B., 2014. A non-linear rod model for folded elastic strips. J. Mech. Phys. Solids 62, 57–80.
Dias, M., Audoly, B., 2015. "Wunderlich, meet Kirchhoff": a general and unified description of elastic ribbons and thin rods. J. Elast. 119 (1–2), 49–66.
Dias, M., McCarron, M., Rayneau-Kirkhope, D., Hanakata, P., Campbell, D., Park, H., Holmes, D., 2017. Kirigami actuators. Soft Matter 13 (48), 9087–9092.
Dill, E., 1992. Kirchhoff's theory of rods. Arch. Hist. Exact Sci. 44 (1), 1–23.
Doedel, E., Fairgrieve, T., Sandstede, B., Champneys, A., Kuznetsov, A., Wang, X., 2007. AUTO-07P: continuation and bifurcation software for ordinary differential equations. Technical Report.
Fan, Z., Hwang, K., Rogers, J., Huang, Y., Zhang, Y., 2018. A double perturbation method of postbuckling analysis in 2D curved beams for assembly of 3D ribbon-shaped structures. J. Mech. Phys. Solids 111, 215–238.
Fischer, F., Rammerstorfer, F., Friedl, N., 2003. Residual stress-induced center wave buckling of rolled strip metal. J. Appl. Mech. 70 (1), 84–90.
Floater, M., 2003. Mean value coordinates. Comput. Aided Geom. Des. 20 (1), 19–27.
Fosdick, R., Fried, E., 2016. The Mechanics of Ribbons and Möbius Bands. Springer.
Fox, D., Raoult, A., Simo, J., 1993. A justification of nonlinear properly invariant plate theories. Arch. Ration. Mech. Anal. 124 (2), 157–199.
Freddi, L., Hornung, P., Mora, G., Paroni, R.. Generalised Sadowsky theories for ribbons from three-dimensional nonlinear elasticity.
Freddi, L., Hornung, P., Mora, M., Paroni, R., 2018. One-dimensional von Kármán models for elastic ribbons. Meccanica 53 (3), 659–670.
Friesecke, G., James, R., Müller, S., 2006. A hierarchy of plate models derived from nonlinear elasticity by gamma-convergence. Arch. Ration. Mech. Anal. 180 (2), 183–236.
Frisch-Fay, R., 1962. Flexible bars. Butterworths scientific publications. Butterworths.
Goriely, A., Nizette, M., Tabor, M., 2001. On the dynamics of elastic strips. J. Nonlinear Sci. 11 (1), 3–45.
Green, A., 1936. The equilibrium and elastic stability of a thin twisted strip. Proc. R. Soc. A 154 (882), 430–455.
Hale, J., Brunetti, M., Bordas, S., Maurini, C., 2018. Simple and extensible plate and shell finite element models through automatic code generation tools. Comput. Struct. 209, 163–181.
Harnach, R., Rothert, H., 1976. On the theory of inextensional bending of shell structures. Int. J. Solids Struct. 12 (5), 359–376.
Hinz, D., Fried, E., 2015. Translation and interpretation of Michael Sadowsky's paper "theory of elastically bendable inextensible bands with applications to the Möbius band". J. Elast. 119 (1–2), 7–17.
Sanders Jr., J.L., 1963. Nonlinear theories for thin shells. Q. Appl. Math. 21 (1), 21–36.
Jiang, H., Khang, D., Fei, H., Kim, H., Huang, Y., Xiao, J., Rogers, J., 2008. Finite width effect of thin-films buckling on compliant substrate: experimental and theoretical studies. J. Mech. Phys. Solids 56 (8), 2585–2598.
Kiendl, J., Bletzinger, K., Linhard, J., Wüchner, R., 2009. Isogeometric shell analysis with Kirchhoff-Love elements. Comput. Methods Appl. Mech. Eng. 198 (49–52), 3902–3914.
Kirby, N., Fried, E., 2015. Gamma-limit of a model for the elastic energy of an inextensible ribbon. J. Elast. 119 (1–2), 35–47.
Kit, O., Tallinen, T., Mahadevan, L., Timonen, J., Koskinen, P., 2012. Twisting graphene nanoribbons into carbon nanotubes. Phys. Rev. B 85 (8), 085428.
Koiter, W., 1966. On the nonlinear theory of thin elastic shells. Proc. Koninkl. Ned. Akad. van Wetenschappen Ser. B 69, 1–54.
Kudrolli, A., Chopin, J., 2018. Tension-dependent transverse buckles and wrinkles in twisted elastic sheets. Proc. R. Soc. A 474 (2214), 20180062.
Liang, H., Mahadevan, L., 2009. The shape of a long leaf. Proc. Natl. Acad. Sci. USA 106 (52), 22049–22054.
Liang, H., Mahadevan, L., 2011. Growth, geometry, and mechanics of a blooming lily. Proc. Natl. Acad. Sci. USA 108 (14), 5516–5521.
Luo, G., Fu, H., Cheng, X., Bai, K., Shi, L., He, X., Rogers, J., Huang, Y., Zhang, Y., 2019. Mechanics of bistable cross-shaped structures through loading-path controlled 3D assembly. J. Mech. Phys. Solids 129, 261–277.
Mahadevan, L., Keller, J., 1993. The shape of a Möbius band. Proc. R. Soc. A 440 (1908), 149–162.
Mansfield, E., 1955. The inextensional theory for thin flat plates. Q. J. Mech. Appl. Math. 8 (3), 338–352.
Marder, M., Sharon, E., Smith, S., Roman, B., 2003. Theory of edges of leaves. Europhys. Lett. 62 (4), 498.
Millán, D., Rosolen, A., Arroyo, M., 2011. Thin shell analysis from scattered points with maximum-entropy approximants. Int. J. Numer. Meth. Eng. 85 (6), 723–751.

Moakher, M., Maddocks, J., 2005. A double-strand elastic rod theory. Arch. Ration. Mech. Anal. 177 (1), 53–91.
Moore, A., Healey, T., 2019. Computation of elastic equilibria of complete Möbius bands and their stability. Math. Mech. Solids 24 (4), 939–967.
Morigaki, Y., Wada, H., Tanaka, Y., 2016. Stretching an elastic loop: crease, helicoid, and pop out. Phys. Rev. Lett. 117 (19), 198003.
Nechaev, S., Voituriez, R., 2001. On the plant Leaf's boundary, jupe à Godets' and conformal embeddings. J. Phys. A 34 (49), 11069.
O'Reilly, O., 2017. Modeling nonlinear problems in the mechanics of strings and rods: the role of the balance laws. Interaction of Mechanics and Mathematics. Springer International Publishing.
Plaut, R., Virgin, L., 2004. Three-dimensional postbuckling and vibration of vertical half-loop under self-weight. Int. J. Solids Struct. 41 (18–19), 4975–4988.
Rafsanjani, A., Bertoldi, K., 2017. Buckling-induced kirigami. Phys. Rev. Lett. 118 (8), 084301.
Reis, P., 2015. A perspective on the revival of structural (in) stability with novel opportunities for function: from Buckliphobia to Buckliphilia. J. Appl. Mech. 82 (11), 111001.
Rubin, M., 2013. Cosserat theories: shells, rods and points. Solid Mechanics and Its Applications. Springer Netherlands.
Sano, T., Wada, H., 2019. Twist-induced snapping in a bent elastic rod and ribbon. Phys. Rev. Lett. 122 (11), 114301.
Seereeram, V., Seffen, K., 2014. Confirming inextensional theory. Int. J. Solids Struct. 51 (19–20), 3439–3448.
Shames, I., Dym, C., 1995. Energy and Finite Element Methods in Structural Mechanics. New Age International Publishers Limited.
Sharon, E., Efrati, E., 2010. The mechanics of non-euclidean plates. Soft Matter 6 (22), 5693–5704.
Sharon, E., Roman, B., Marder, M., Shin, G., Swinney, H., 2002. Mechanics: buckling cascades in free sheets. Nature 419 (6907), 579.
Shim, J., Perdigou, C., Chen, E., Bertoldi, K., Reis, P., 2012. Buckling-induced encapsulation of structured elastic shells under pressure. Proc. Natl. Acad. Sci. USA 109 (16), 5978–5983.
Simo, J., 1985. A finite strain beam formulation. the three-dimensional dynamic problem. Part I. Comput. Methods Appl. Mech. Eng. 49 (1), 55–70.
Simo, J., Fox, D., 1989. On a stress resultant geometrically exact shell model. Part I: formulation and optimal parametrization. Comput. Methods Appl. Mech. Eng. 72 (3), 267–304.
Simo, J., Fox, D., Rifai, M., 1990. On a stress resultant geometrically exact shell model. Part III: computational aspects of the nonlinear theory. Comput. Methods Appl. Mech. Eng. 79 (1), 21–70.
Simo, J., Vu-Quoc, L., 1986. A three-dimensional finite-strain rod model. Part II: computational aspects. Comput. Methods Appl. Mech. Eng. 58 (1), 79–116.
Starostin, E., van der Heijden, G., 2007. The shape of a Möbius strip. Nat. Mater. 6 (8), 563.
Starostin, E., van der Heijden, G., 2015. Equilibrium shapes with stress localisation for inextensible elastic Möbius and other strips. J. Elast. 119 (1–2), 67–112.
Steigmann, D., 2013. Koiter's shell theory from the perspective of three-dimensional nonlinear elasticity. J. Elast. 111 (1), 91–107.
Stuelpnagel, J., 1964. On the parametrization of the three-dimensional rotation group. SIAM Rev. 6 (4), 422–430.
Sun, Y., Choi, W., Jiang, H., Huang, Y., Rogers, J., 2006. Controlled buckling of semiconductor nanoribbons for stretchable electronics. Nat. Nanotechnol. 1 (3), 201.
Sze, K., Liu, X., Lo, S., 2004. Popular benchmark problems for geometric nonlinear analysis of shells. Finite Elem. Anal. Des. 40 (11), 1551–1569.
Tarasovs, S., Andersons, J., 2008. Buckling of a coating strip of finite width bonded to elastic half-space. Int. J. Solids Struct. 45 (2), 593–600.
Taylor, M., Davidovitch, B., Qiu, Z., Bertoldi, K., 2015. A comparative analysis of numerical approaches to the mechanics of elastic sheets. J. Mech. Phys. Solids 79, 92–107.
Todres, R., 2015. Translation of W. Wunderlich's "on a developable Möbius band". J. Elast. 119 (1–2), 23–34.
Tutte, W., 1963. How to draw a graph. Proc. Lond. Math. Soc. 3 (1), 743–767.
Vella, D., Bico, J., Boudaoud, A., Roman, B., Reis, P., 2009. The macroscopic delamination of thin films from elastic substrates. Proc. Natl. Acad. Sci. USA 106 (27), 10901–10906.
Witten, T., 2007. Stress focusing in elastic sheets. Rev. Mod. Phys. 79 (2), 643.
Yu, T., Hanna, J., 2019. Bifurcations of buckled, clamped anisotropic rods and thin bands under lateral end translations. J. Mech. Phys. Solids 122, 657–685.